

Chapter 1

Introduction

1.1 Background

Since carbon nanotubes (CNTs) were first discovered by Dr. Iijima^[Iijima 91-56], many research groups all over the world are attracted to investigate and study its growth mechanisms, structures, morphologies, and corresponding applications. The experimental results show that CNTs are fullerene-related structure and just like the shape of the elongated fullerene. Depends on the number of graphite layers, they are generally classified single-walled carbon nanotubes (SWNT) and multi-walled carbon nanotubes (MWNT).

Single-wall carbon nanotubes have shown the highest Young's modulus and highest axial thermal conductivity, very high aspect ratios ($> 10^3$), extremely high surface area, small radius of curvature, extraordinary mechanical strength and chemical stability, therefore, SWNTs are being developed for many applications like field emission display (FED)^[Sander-1998-49], biology technology^[Dai-1996-147], fuel cell^[Liu-1999-1127], nanotube-polymer solar cell^[Landi-2005-167], single electron transistor^[Bachtold-2001-1317], etc. Furthermore, in the applications of nano-device integrated with Si chip, structural manipulation is important and the deposition temperature must be low in particularly to ensure compatibility with the IC processes. Accordingly, the fabrication of SWNTs with the desired morphology at low temperatures has attracted significant interest among academic researchers and technology users.

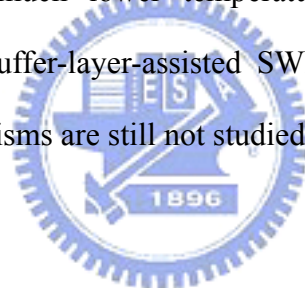
Single-walled carbon nanotubes (SWNTs) can be fabricated by using arc-discharge^[Saito-1995-33] and laser ablation^{[Guo-1995-49] [Thess-1996-483]}, which are high

temperature processes (above 1500 K). Recently, catalytically assisted CVD methods, which are relatively low temperature processes for synthesizing SWNTs, have been widely studied. However, most of the as-grown SWNTs fabricated by CVD have randomly entangled morphologies^{[Kong-1998-567][Delzeit-2001-368][Seidel-2004-1888]}, which cannot be practically applied. Vertical aligned of MWNTs has been synthesized in previous report^{[Modi-2003-171] [Fan-1999-512] [Wei-2002-495]}. As for SWNTs, only those aligned parallel to substrate has been achieved by the application of a strong electric or magnetic field^{[Zhang-2001-3155] [Joselevich-2002-1137] [Fischer-2003-2157]}. Although Murakami and Zhang et al.^{[Murakami-04-298] [Zhang-06-198]} recently adopted bimetallic Co-Mo catalyst to successfully synthesize vertically SWNT films on quartz substrate. However, the maximum thickness of as-grown SWNTs films is only 5 μm and its growth temperature is still high (~ 800 °C). Besides, purity is a key issue for application of SWNTs, current commercial SWNTs fabricated by arc-discharge or catalytic-CVD is around 50~70 %^{[http-CNI] [http-Helix]}. A lot of impurities, such as amorphous carbon and catalyst metals, are included in the produced soot besides SWNTs. Although, many SWNT purification methods have been reported up to now^{[Rinzler-1998-29] [Feng-2003-645] [Haruyunyan-2002-867] [Suzuki-2007-1167]}, these methods are not suitable for CNTs-integrated Si-based nano-device.

The treatment of the catalyst represents another technological challenge in SWNTs growth. Physical vapor deposition (PVD) is the most popular approach for depositing catalytic materials because it highly compatible with the IC process. The catalyst films are typically treated with H-plasma to become well-distributed nano-particles, and CNTs are subsequently grown from these pre-treated catalytic nanoparticles. However, the agglomeration of nano-particles is unavoidable during the heating process, which does not particularly favor the fabrication of SWNTs. The ultra-thin catalytic film was deposited to make smaller nano-particles but the

as-grown SWNTs were few and retained random structures^{[Delzeit-2001-368] [Seidel-2004-1888]}. Restated, forming and preventing the agglomeration of small catalytic nano-particles is key to solving these problems.

Buffer layer was employed to solve the particles agglomeration in recently research report. Arcos et al.^[de los Acros-2004-187] presented the alumina buffer layer deposited under catalyst layer can effectively promote the synthesis of SWNTs at 840 °C. Delzeit et al.^[Delzeit-2001-368] also obtained a similar result by incorporating alumina buffer layer and multilayered metal catalysts at ~900 °C. Afterwards, Seidel et al.^[Seidel-2004-1888] and Zhong et al.^[Zhong-05-1558] have further reduced the synthesizing temperature of SWNTs to ~ 600 °C. These findings indeed provide a potential process for fabricating SWNTs at much lower temperature, however, the quality and morphologies of as-grown buffer-layer-assisted SWNTs could not be manipulated well and their growth mechanisms are still not studied thoroughly.



1.2 Motivation

Catalytic-CVD method collaborating buffer layer had been considered as a high potential process to approach the fabrication of SWNTs in previous research. However, fabrication of SWNTs with the desired morphology at low temperatures is still a challenge and their growth mechanism is a debated issue. On the other hand, synthesis and effective control of the nanostructures of single-walled carbon nanotubes (SWNTs) are the current bottlenecks of CNTs researches in which process temperature further determines the feasibility of SWNTs integrated with Si-based devices.

In this work, the processes to fabricate catalyst and buffer layer-assisted SWNTs on Si wafer were developed by both microwave plasma-enhanced chemical vapor

deposition (MPCVD) and electron cyclotron resonance chemical vapor deposition (ECR-CVD) with different buffer and catalyst materials, using CH_4 and H_2 as source gases. The buffer and catalyst materials include ZnS-SiO_2 , Si_3N_4 , TiN , Al_2O_3 , AlN , and AlON of 5 ~ 15 nm in thickness, and Co, Fe, and novel CoCrPtO_x precursor films of 1 ~10 nm in thickness, respectively. The effects of catalysts, buffer layer materials, synthetic method and process conditions on the characteristics of the as-grown SWNTs are investigated and their growth mechanisms are proposed.



Chapter 2

Literature review

2.1 Structures and properties of SWNTs

CNTs are one dimension nanostructure of carbon bonded mainly by sp^2 bond and crooked by sp^3 bonds with hollow and cylindrical construction. It was proposed that a graphene sheet of (0001) plane could be rolled to become various forms of CNTs structures shown in Fig. 2.1^[Dresselhaus-1996-p756]. The single-walled CNTs (SWNTs) and multi-walled CNTs (MWNTs) are defined whether the number of the rolled graphene layers is one or more. SWNTs were first time synthesized using arc-discharge method by Dr. Iijima^[Iijima-1991-56] and D.Bethune^[Bethune-1993-605] in 1993. The smallest sized SWNTs (~ 0.4 nm) existed stabile in the world were fabricated by Wang et al. using zeolite (AlPO4-5) with diameter of 0.73 nm as template^[Wang-2000-51].

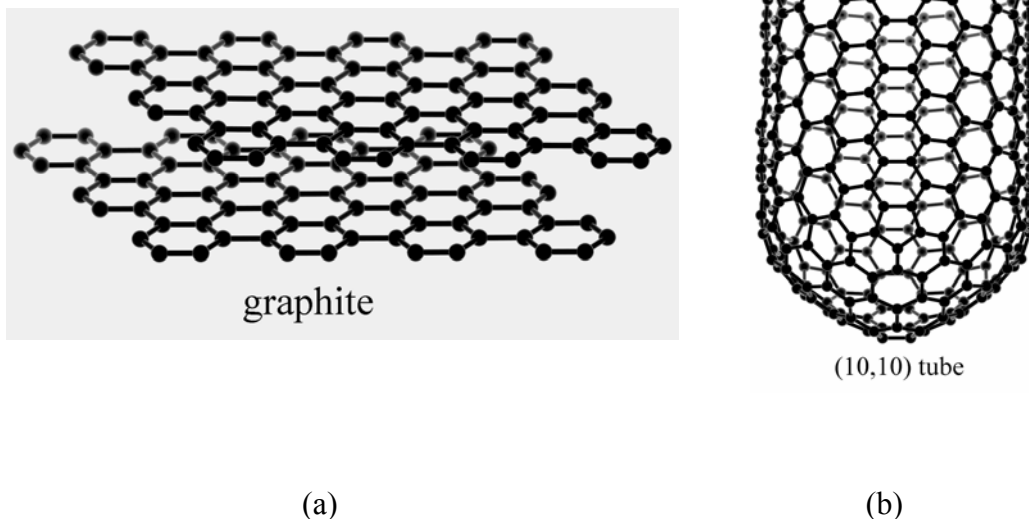


Fig. 2-1 (a) Graphite sheet, and (b) formed CNT rolled by the graphite sheet^[Dresselhaus-1996-p756].

In mathematics, scientists proposed a vector to define CNTs^[Saito-92-2204].

$$C_h = na_1 + ma_2 \equiv (n, m) \quad (2-1)$$

The C_h called chiral vector, and the angle between C_h and a_1 is chiral angle θ , while a_1 and a_2 denoted the unit vectors of graphene sheet. As shown in Fig. 2.2, the structures of CNTs in zigzag, armchair or chiral form are classified by the θ angle or range, i.e. 0° , 30° or $0^\circ < \theta < 30^\circ$, respectively. The chiral vector is expressed as a pair of integers (n, m) for mapping planar graphene sheet. The zigzag, armchair and chiral CNTs are corresponding to the chiral vectors of $(n, 0)$, (n, n) and (n, m) , respectively.

(a) Electrical properties :

In 1992, Hamada and Saito ^[Hamada-1992-1579] ^[Saito-1992-2204] proposed that the chirality of CNTs determines the tube is a conductor or a semiconductor. In 1998, Wildoer and Odom ^[Wildoer-1998-59] ^[Odom-1998-62] further proved this assumption by STM, in which they indicated that the two parameters, helicity and diameter, can be adopted to identify the metallic and semi-conducting properties of CNTs, such as the differences in the band gap and the Fermi energy shift. Among them, the armchair CNTs have two integers n and m equal to each other, thus have bands that cross the Fermi level and therefore are truly metallic. The chiral and zigzag nanotubes had two possibilities: (a) If $n-m = 3k$, where k is a integer except zero, then it was metallic with an energy gap of about 1.7 - 2.0 eV; (b) If $n-m \neq 3k$, then it was semiconducting with an energy gap of about 0.5 - 0.6 eV [Fig. 2.3]. These show the nanotubes electrical properties are very sensitive to the wrapping angle and the tube diameter. Ballistic transport in the CNT channel was assumed.

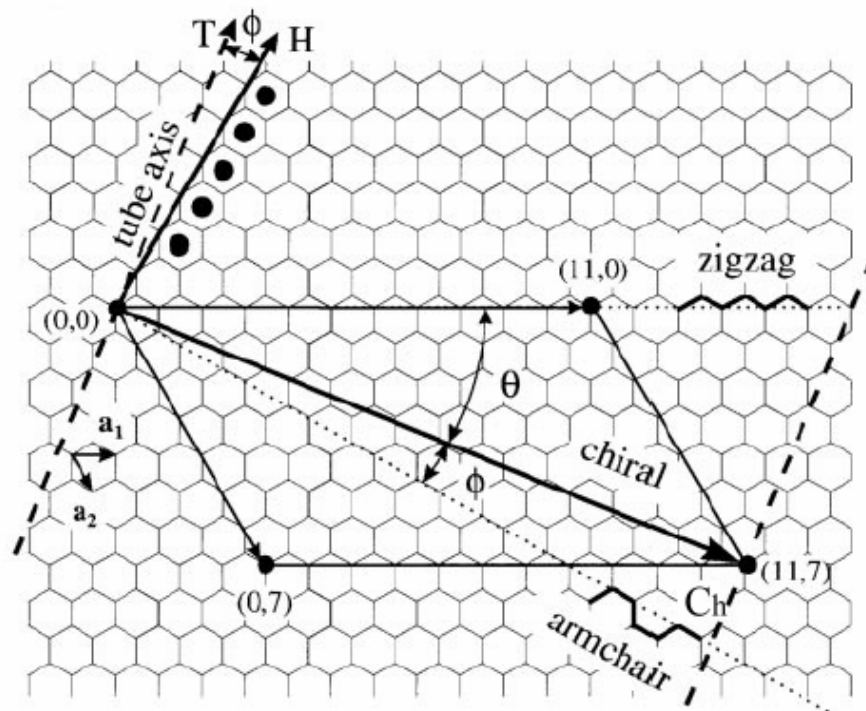


Fig. 2-2 The construction of CNT from a single graphite sheet^[Saito-1992-2204]

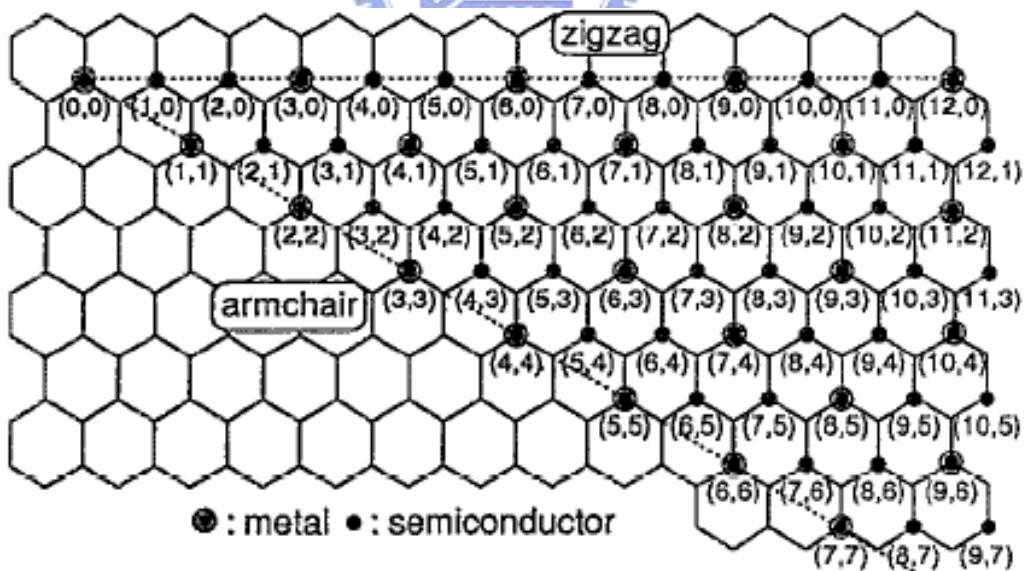


Fig. 2-3 The relation between properties and structure of CNTs^[Saito-1992-2204]

(b) Thermal conductivity and mechanical strength:

Che et al. ^[Che-2000-65] reported that thermal conductivity of 10-nm-long CNTs was great than 2800 W/mK, which is almost equal to diamond. Moreover, Berber et al. ^[Berber-2000-4613] predicted the thermal conductivity of (10,10) SWNT is about 6600 W/mK at room temperature. This amazing findings promise that SWNTs is a potential candidate materials for thermal management applications such as heat sink.

With respect to mechanical properties of SWNTs, Treacy ^[Treacy-1996-678] et al. obtained a Young's modules of ~1.8 Tpa calculating from the vibration of tip of tubes under different temperatures by TEM. Thus, SWNTs can be used for potential applications in reinforcement of the composites.

2.2 Synthesis methods of SWNTs

Arc-discharge, laser ablation and chemical vapor deposition (CVD) are the most popular methods ^{[Lee-2001-245] [Zhou-1994-1593]} to synthesize SWNTs where carbon sources can be in gas or solid phases. Manipulating the following process parameters often controls the morphology and properties of SWNTs: substrate temperature, precursor gases and gas ratio, catalyst, pretreatment conditions, applied bias, etc. However, the proposed methods still suffer the following problems of low yielding, low uniformity in structure and property and low quality.

(a) Arc-discharge method ^[Saito-1995-979]

Arc-discharge method is the earliest method to synthesize SWNTs where Fig. 2.4 shows the schematic diagram of the arc-discharge system ^[Saito-1995-979]. Bethune ^[Bethune-1993-605] used graphitic rods containing small amount of Co catalyst and pure graphitic rods as anode and cathode, respectively. Arcing was occurred between two

electrodes when DC voltage (20 to 40 V) is applied under He or Ar atmosphere of 10-500 Torr. Then, as-deposited carbon nanostructures were deposited in the cathode where the production includes amorphous carbon, fullerenes, carbon cluster, carbon nanotubes and varieties of other carbon structures. SWNTs were obtained from these as-deposited carbon nanostructures after purification treatment. The low yielding and low purification of as-deposited SWNTs is the problem to be solved.

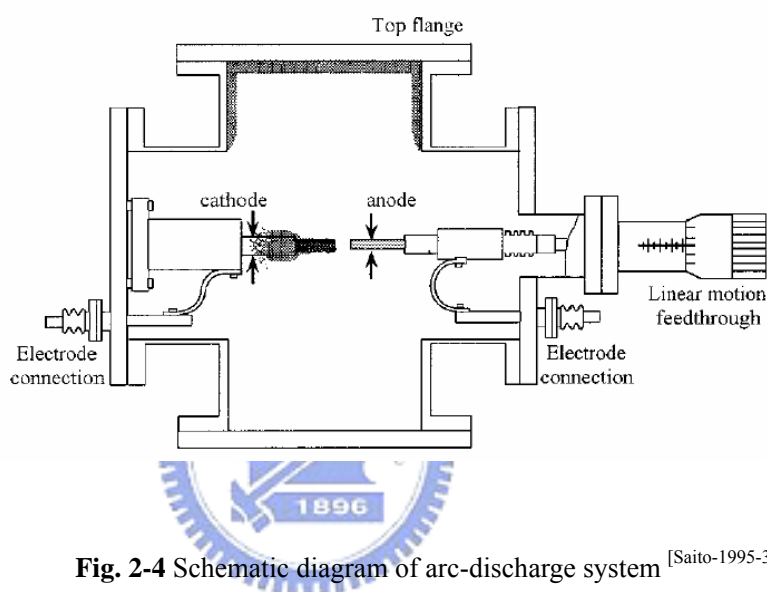


Fig. 2-4 Schematic diagram of arc-discharge system [Saito-1995-33]

(b) Laser vaporization^[Guo-1995-49]

Direct laser vaporization produced SWNTs in the condensed vapor in a heated flow tube using transition-metal/graphite composite rods was first reported by Guo's group in 1995^[Guo-1995-49]. The schematic diagram of the laser-vaporization system is shown in Fig. 2.5. There is an incident laser beam for vaporizing graphite target under helium or argon gas atmosphere at pressure of 500 Torr and then the productions are swept out by the flowing gas and to be deposited on the water cooled collector. A much higher yield is found compared to those produced by arc-discharge method. Thess et al.^[Thess-96-483] further optimized the laser-oven method to synthesize SWNTs in yield of more than 70% by using Co-Ni/graphite composite target.

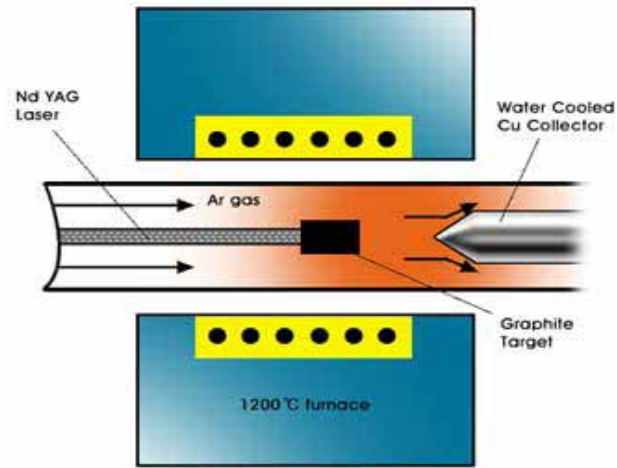
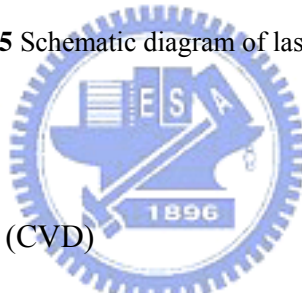


Fig. 2-5 Schematic diagram of laser ablation system ^[Guo-1995-49]



(c) Chemical vapor deposition (CVD)

The CVD method is the most popular method to synthesize CNTs, which takes the advantage of low temperature, high yield and well structural manipulation. It is essential for CVD process to introduce the energy to decompose precursor gases (such as CH₄, C₂H₂, C₂H₄, C₆H₆, CO, etc.) and deposit the reaction product on the substrate surface. The introduced energy may include thermal, microwave, RF, or others; thus, the different process names were defined depending on the source of the applied energy. Various CVD processes to synthesize CNTs have been proposed by many researchers, including microwave plasma enhanced CVD (MPE-CVD)^[Tsai 1999-3462], electron cyclotron resonance CVD (ECR-CVD)^[Lin 2002-922], inductively coupled plasma CVD (ICP-CVD)^[Delzeit 2002-6027], RF plasma enhanced CVD (RF-PE-CVD)^[Kato 2004-2], DC plasma enhanced CVD (DC-PE-CVD)^[Hofmann 2004-1171], thermal CVD^{[Lee}

2000-3397], hot filament CVD (HF-CVD)^[Yang 2004-433], point arc CVD^[Zhong-05-1558], HiPco^[Nikolaev-99-91] etc. Figure 2.6 shows a schematic diagram of typical thermal CVD system of synthesizing carbon nanotubes. Among them, SWNTs were still not successfully fabricated by ECRCVD method and the presently smallest size of synthesized CNTs is ~ 6 nm with 5 layers^[Minea-05-1101].

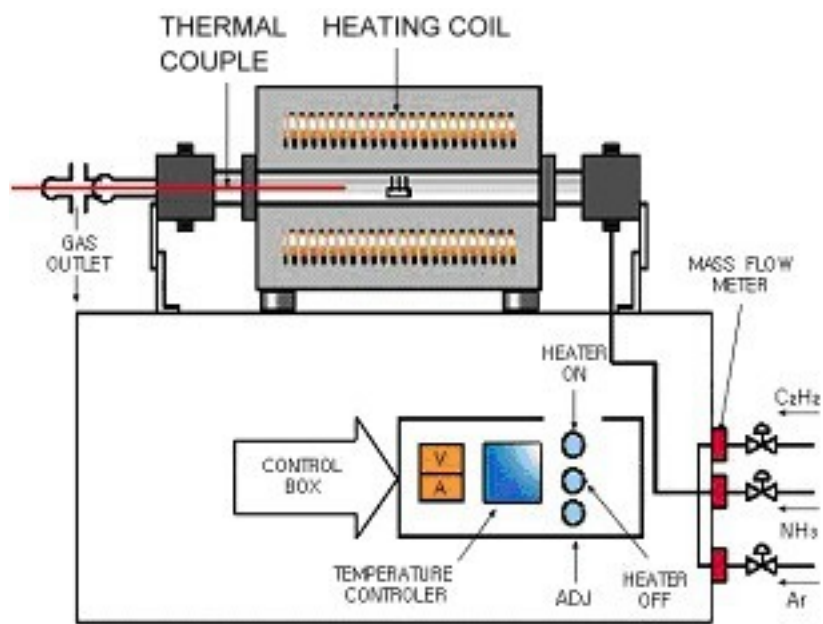


Fig. 2-6 Schematic drawings of thermal CVD system^[Lee-2001-245]

2.3 Structures and process parameters of as-grown SWNTs by catalytic-CVD

Pure transition metals (such as Fe, Co, Ni) were widely employed to fabricate SWNTs by using catalytic CVD. However, the most as-grown SWNTs demonstrate entangled morphology and poor quality^[Seidel-04-1888]. Therefore, alloy catalyst was developed to improve the quality and manipulation of as-deposited SWNTs. Yoon et al.^[Yoon-02-318], first time, used co-sputtered Co-Mo thin film to fabricate SWNTs but still obtained random morphology. Afterward, Murakami^[Murakami-04-298] used mono-dispersed Co-Mo catalyst thin film by dip-coating to successfully vertically aligned SWNT films. Zhang et al.^[Zhang-06-198] further revealed that vertically aligned SWNT films could be synthesized varying the density of Co-Mo catalyst particles.

The other approach is employment of buffer layer materials. T. de los Arcos et al.^[T. de los Arcos-04-187] demonstrated that buffer layer (Al, Al₂O₃, TiN, TiO₂) can strongly influence the growth of CNTs, in which only Al₂O₃ can be helpful to SWNTs formation. Delzeit^[Delzeit-01-368] had revealed that under layer of Al could enhance the SWNTs growth but afterward T. de los Arcos et al.^[T. de los Arcos-03-419] used XPS to prove that this effect is resulted from oxidation of Al film not by pure Al layer. Therefore, Al₂O₃ was considered as the most effective buffer layer to enhance SWNTs growth and attracted much interest in past few years. Some groups develop the process to fabricate SWNTs using alloy catalyst adopting Al₂O₃ buffer layer^{[Zhang-2003-731][Lacerda-2004-269]}. Except above concept, Zhong et al.^[Zhong-05-1558] used novel point-arc CVD to successfully fabricate dense and vertically aligned SWNT films employing sandwich-like structure of Al₂O₃/Fe/Al₂O₃. Catalyst and buffer layer materials for SWNTs growth that revealed in previous study are summarized in Table 2.1.

Table 2.1 General characteristics and synthetic method of as-deposited SWNTs using various catalyst, buffer layer materials in previous study

Catalyst	Buffer layer	Gas	Temperature (°C)	Morphology	I _G /I _D ratio	Method	Ref.
Co-Mo	—	Ar/ H ₂ , CO, ethanol	750~800	Vertically aligned film	10~15	Thermal CVD	[Murakami-2004-298] [Maruyama-2005-320] [Zhang-2006-198]
Fe	Al ₂ O ₃	CH ₄ /H ₂	600	Vertically aligned film	~12.5	Point-arc CVD	[Zhong-2005-1558]
Fe	Al /Al ₂ O ₃	C ₂ H ₄ /H ₂ O	750	Vertically aligned film of 2.5 mm	5~10	Thermal CVD	[Hata-2004-1361][Futaba -2005-056104]
Fe	—	CO	800~1200	Ropes	—	HiPco	[Nikolaev-1999-91]
Mo	—	Ar/CO	1200	Spaghetti-like	—	Thermal CVD	[Dai-1996-471]
Ni,Co	Al	CH ₄ /C ₂ H ₂ / H ₂	600~900	Spaghetti-like	—	Thermal CVD	[Seidel-2004-1888]
Fe/Mo	Al, Ir	Ar/ CH ₄	900	Spaghetti-like	~10	Thermal CVD	[Delzeit-2001-368]
Metal salts (Mo,Al,Fe)	Al	CH ₄	900	Network-like	—	Thermal CVD	[Cassell-2003-817]
Fe	Al ₂ O ₃	C ₂ H ₂	840	Very few in MWNT films	~1.5	Thermal CVD	[de los Acros-2004-187]

2.4 The proposed growth mechanisms of SWNTs

Two typical growth modes of catalyst-assisted CNTs have been proposed: tip-growth mode, in which the catalyst particle is detached from the substrate and remains at the tip of the growing tube, and base-growth mode, in which the catalyst remains on the substrate. Actually, many detailed and precise growth mechanisms about the catalytic CVD methods for SWNTs growth have been proposed and described as follows:

(a) Ball-and-stick catalyst scooting model

This model was proposed by Birkett et al.^[Birkett-1997-111] to explain the phenomenon that catalyst was not found at tip of SWNT. Birkett et al. proposed that transition metals show a high propensity for decoration fullerene surfaces. A carbon fragments bind to the metal clad fullerene and they may self-assemble as a surrounding circular hexagonal chicken-wire-like fence. Once formed as a belt, the network could propagate as a cylinder, so called open edge growth. This model predicts the SWNT diameter will be $d(C_{60}) + 2*d(\text{Interplanar distance})$, i.e. $0.7 \text{ nm} + 2(0.34) \text{ nm} = 1.38 \text{ nm}$, which is in excellent agreement with observation. Another similar model was scooter mechanism^[Thess-1996-483] which considered that a few metal atoms chemisorbed and scooted around the open edge of the sheet and kept tube open and grow. When metal atoms aggregated and lost its kinetic energy for scooting, SWNT growth will stop. Figure 2.7 shows the schematic diagram of ball-and-stick scooting model.

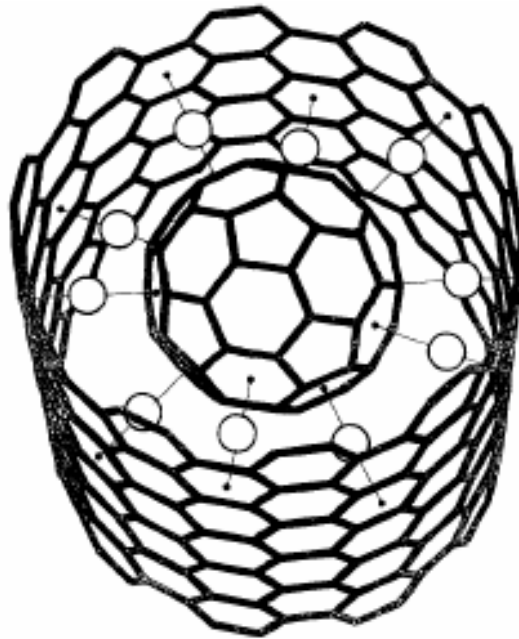


Fig. 2-7 Schematic diagram of ball-and-stick scooting model ^[Birkett-1997-111]

(b) Root growth mechanism

Saito et al. ^[saito-1994-L526] proposed this model to explain the growth mechanism of radiate sea-urchin-like SWNTs ^[saito-1994-L526] synthesized by arc-discharge, in which numerous SWNTs grow from a single catalyst particle and their diameter is much smaller than catalyst (Fig. 2.8). Saito et al. proposed that carbon-metal alloy particles were formed by vaporization during arc discharge process, and this carbon-metal alloy possesses much carbon solubility than in a solid state. Thus, these liquid alloy particles begin to segregate excess carbon on their surfaces with the decrease of temperature of the cathode. There are two possible conditions will be observed: One condition is that the cooling rate of particles proceeded at a moderate rate and the supersaturation of carbon in metal particles was not high, the carbon will be gradually segregated on the surface to form graphitic layers. The other condition is the cooling rate was rapid and dissolved carbon species in a particle was very high, supersaturation of carbon would cause numerous nucleation site of graphite on the particle surface. A large number of tiny graphitic flakes are formed and then close their open ends in order to saturate dangling bonds at their periphery. Among this random assembly of graphitic flakes, seeds of SWNTs may be formed (Fig. 2.9).

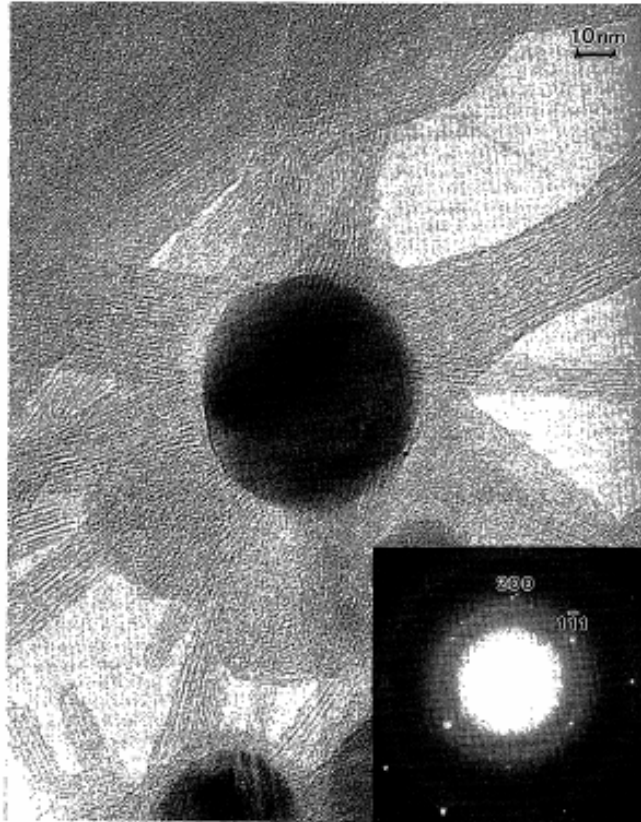


Fig. 2-8 TEM image of radiate sea-urchin-like SWNTs [saito-1994-L526]

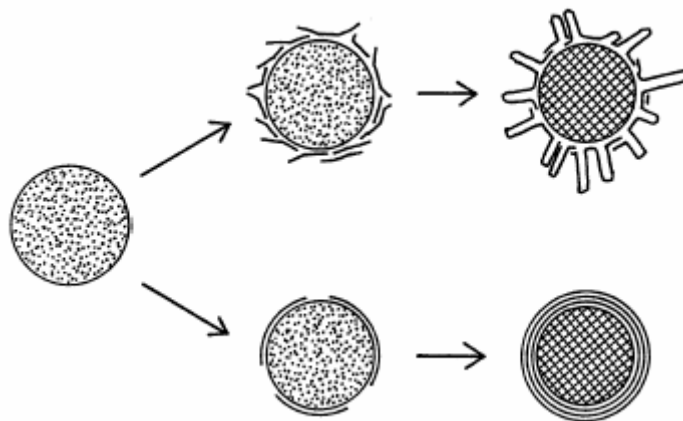


Fig. 2-9 Schematic diagram of root growth mechanism-1 [saito-1994-L526]

Zhou et al.^[zhou-1994-1593] also observed bundles of SWNTs protruding radially from Y_2C particles coated with graphitic multi-layers. The graphitic cages separating Y_2C particle and SWNT bundles fall into the narrow range of 10-20 layers (Fig. 2-10). He suggests a two-step growth model: The radial SWNTs growth pattern is first initiated by catalytic action between the Y_2C , droplet and the carbon in the gas phase. Second, and upon cooling, the graphitic cage starts by segregating excess carbon from the Y_2C , bulk, arresting further growth of SWNTs.

The growth mechanism of SWNTs investigated by Saito and Zhou are produced by arc-discharge. Furthermore, Gavillet et al.^[Gavillet-2001-275504] suggested a common growth mechanism based on a vapor-liquid-solid model for SWNTs synthesized from different techniques and quantum-molecular-dynamics simulations support a root growth mechanism where carbon atoms are incorporated into the tube base by a diffusion-segregation process. The first step is the formation of a liquid nanoparticle of metal supersaturated with carbon [Fig. 2.11(a)]. Then, there is a competition between the formation of a graphitic sheet [Fig. 2.11(b)] and the nucleation of single-wall nanotubes [Fig. 2.11(c)]. In order to obtain long nanotubes [Fig. 2.11(d)], the root-growth process should continue for a sufficiently long time, until local temperatures are too low, leading to the solidification of the nanoparticles. Figures 2.11(e) and 2.11(f) show that nucleation did occur but growth did not take place so that carbon has partly condensed into amorphous carbon flakes or into a few graphitic layers.

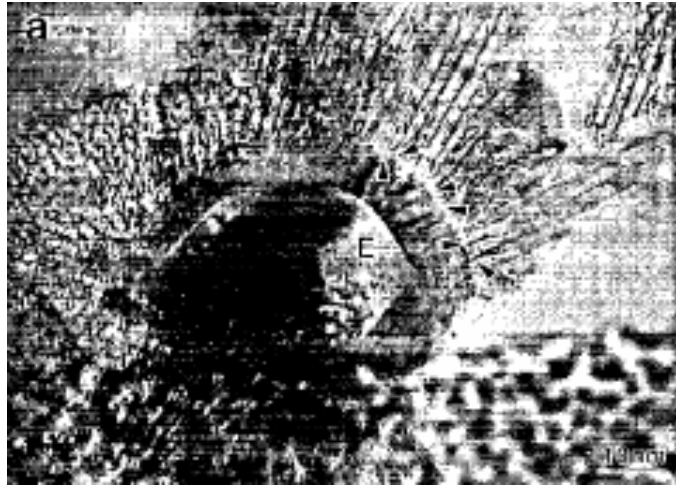


Fig. 2-10 TEM image of the interface between the multilayered cage and the single-walled tubes [zhou-1994-1593]

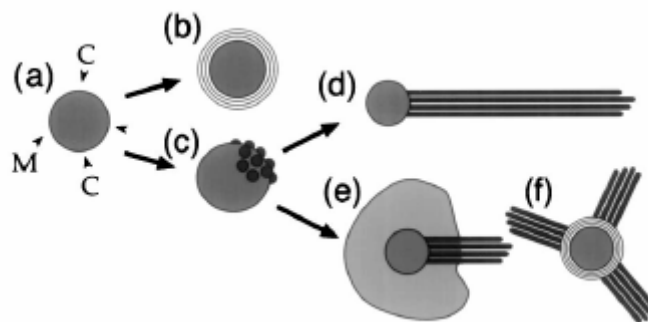


Fig. 2-11 Schematic diagram of root growth mechanism -2 [Gavillet-2001-275504]

(c) Yarmulke mechanism

Dai et al.^[Dai-1996-471] proposed this model to explain growth mechanism of SWNTs synthesized on molybdenum nanoparticles by the disproportionate of CO at 1200°C and concluded that catalyst size determines the tube diameter. They supposed tubes were close end and carbon atoms were chemisorbed on the catalyst to form yarmulke firstly. And then carbon source decomposed and diffused into catalyst, to make SWNTs grew longer. In the case of catalyst particles with sizes of ~1 nm, SWNTs of ~1 nm diameter were produced. When the catalyst particles with sizes in the range of 5~20 nm, MWNTs were formed. If the size is larger than 50 nm, graphite-covered metal particles were predominantly formed (Fig. 2.12).

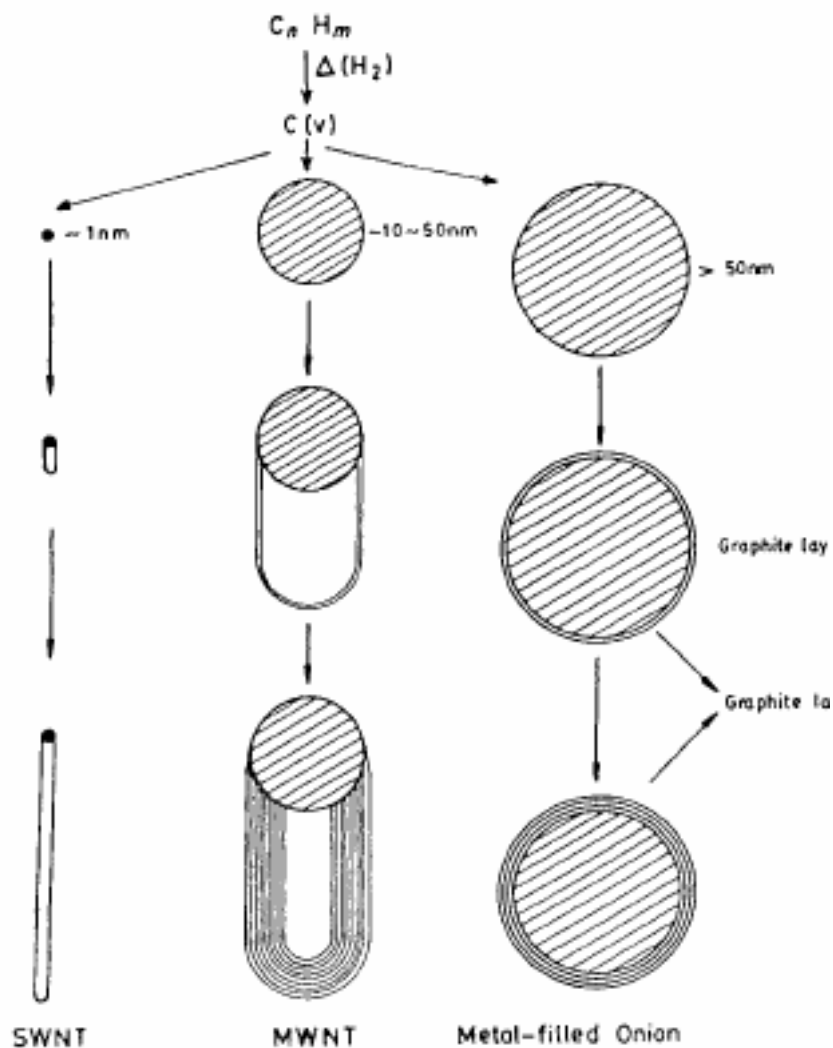


Fig. 2-12 Schematic diagram of yarmulke mechanism^[Dai-1996-471]

(d) Solid–liquid–solid growth mechanism

Gorbunov et al.^[Gorbunov-2002-113] proposed that a molten catalyst nanoparticle penetrates an amorphous carbon aggregate dissolving it and precipitating carbon atom [Fig. 2.13(a)]. These atoms arrange in a graphene sheet [Fig. 2.13(b)], whose orientation parallel to the supersaturated metal-carbon melt is not energetically favorable. Any local defect of this graphene sheet will result in its buckling [Fig. 2.13(c)] and formation of a SWNT nucleus [Fig. 2.13(d)]. Further precipitating carbons incorporate in edges of growing nanotube [Fig. 2.13(e)], which are anchored to the catalyst nanoparticle by overlapping its unsaturated sp^2 orbitals with the metal orbitals of the catalyst nanoparticles.

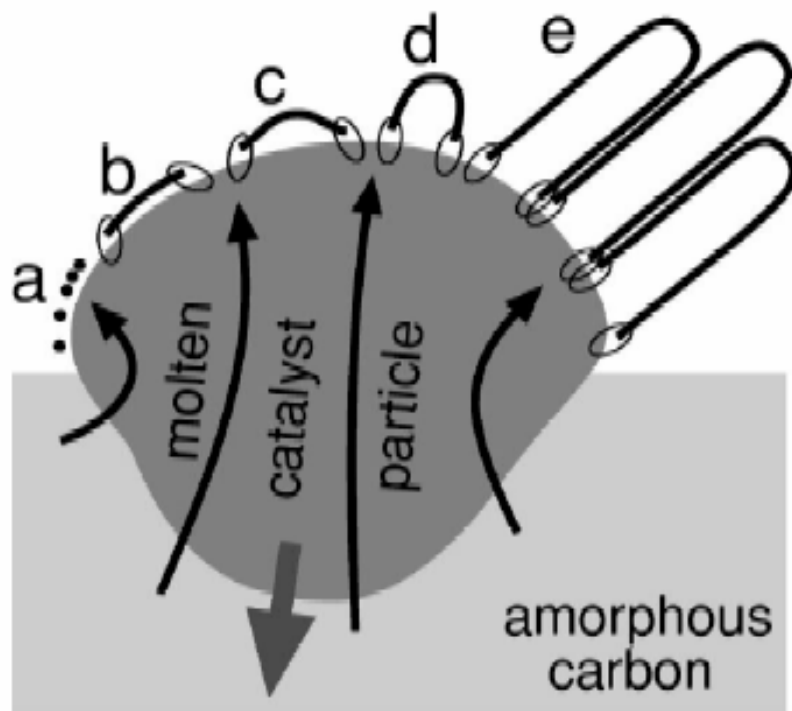


Fig. 2-13 Schematic diagram of Solid–liquid–solid growth mechanism^[Gorbunov-2002-113]

2.5 Analytical methods of SWNTs

HRTEM is the most direct method to analyze the structure of small sized CNT, such as layer number and diameter (Fig. 2.14). However, SWNT samples preparation with well dispersion is difficult and structure of SWNTs is easily destroyed under a high energy electron beam. Thus, Raman spectroscopy analysis, which takes advantage of large area, precise and easily operation, was widely investigated and developed to characterize the presence, diameter and graphitized-degree of SWNTs.

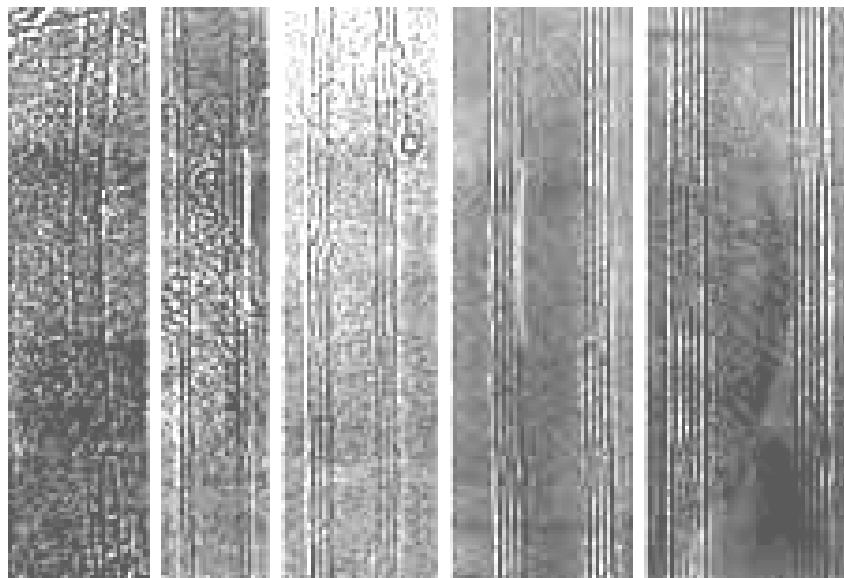


Fig. 2-14 (a) SWNT, (b) double-walled CNT, (c) three-walled CNT, (d) four-walled CNT, and (e) five-walled CNT [成惠民-2004-p. 30]

Rao et al. [Rao-1997-187], first time, used Raman scattering from vibration mode of CNTs to characterize the tube diameter. He proposed that SWNT has 15 or 16 Raman-active modes, but some of their Raman scattering are difficult to detect. Thus, only 7 Raman-active modes can be observed in measurement, as shown in Fig. 2.15.

Raravikar et al. [Raravikar-2002-235424] further investigated the relationship between Raman spectrum and as-produced SWNTs (synthesized by HiPCO method). Figures 2.16(a) and 2.16(b) show a typical Raman spectrum of SWNT sample taken at room temperature. The two prominent peaks with a peak position of 182 and 264 cm^{-1} in Fig. 2.16(a) are the two RBM

(radial breath mode, A_{1g}) peaks. The two peaks from Fig. 2.16(b) at peak positions ~ 1590 and $\sim 1350 \text{ cm}^{-1}$ belong to the G-band (tangential stretching mode, E_{2g}) and D-band (from amorphous carbon, A_{1g}), respectively.

The RBM is a unique feature in the Raman spectrum of SWNTs and involves a collective vibration movement of the carbon atoms towards and away from the central axis of a SWNT. The RBM oscillations are associated with a periodicity imposed on a graphene sheet by wrapping it into a finite-size (small diameter) tube. Consequently, the associated RBM Wavelength and frequency are directly related to the perimeter of the nanotube. Base on this relationship, as the diameter of the nanotube increases, the RBM frequency shifts to lower wave numbers. For larger and, particularly, MWNTs, the RBM frequency becomes very small and, at the same time, the intensity of the radial breathing mode decreases and ultimately becomes undetectable by Raman spectroscopy measurements. Hence, Dresselhaus et al.

[Dresselhaus-2002-2043] proposed that the frequency of the RBM are :

$$\omega = \bar{a}(\text{cm}^{-1} \text{ nm})/d(\text{nm}) \quad (2-7)$$

where \bar{a} for the Si /SiO substrate is experimentally found to be $248 \text{ cm}^{-1} \text{ nm}$ for isolated SWNTs, ω is the peak position, d is the SWNT diameter and RBM is independent of chiral angle.

As a DWNT can be considered as two coaxial SWNTs, it causes Raman spectroscopic features similar to those of SWNTs: the radial breathing mode (RBM), a D band and a G band. Moreover, in the RBM and G band of the DWNTs, two components associated to vibration of inner and outer layers of DWNTs can be found [Li-2005-623]. Thus, the RBM peaks demonstrate the possible presence of SWNT and DWNT. However, Costa et al. [Costa-2004-2527] indicated that RBM peaks cannot be found in the DWNTs with larger diameter. In this study, we identify carefully the presence of SWNTs by TEM/HRTEM following Raman spectrum to avoid the misjudgement.

Furthermore, Tuinstra et al. [Tuinstra-1970-1126] proposed that the Raman spectra of single crystals of graphite shows only one mode at 1575 cm^{-1} and as the increase of defects and

disorder, D-band will show. Therefore, the I_G/I_D ratio can be used to determine the graphitized degree of SWNTs.

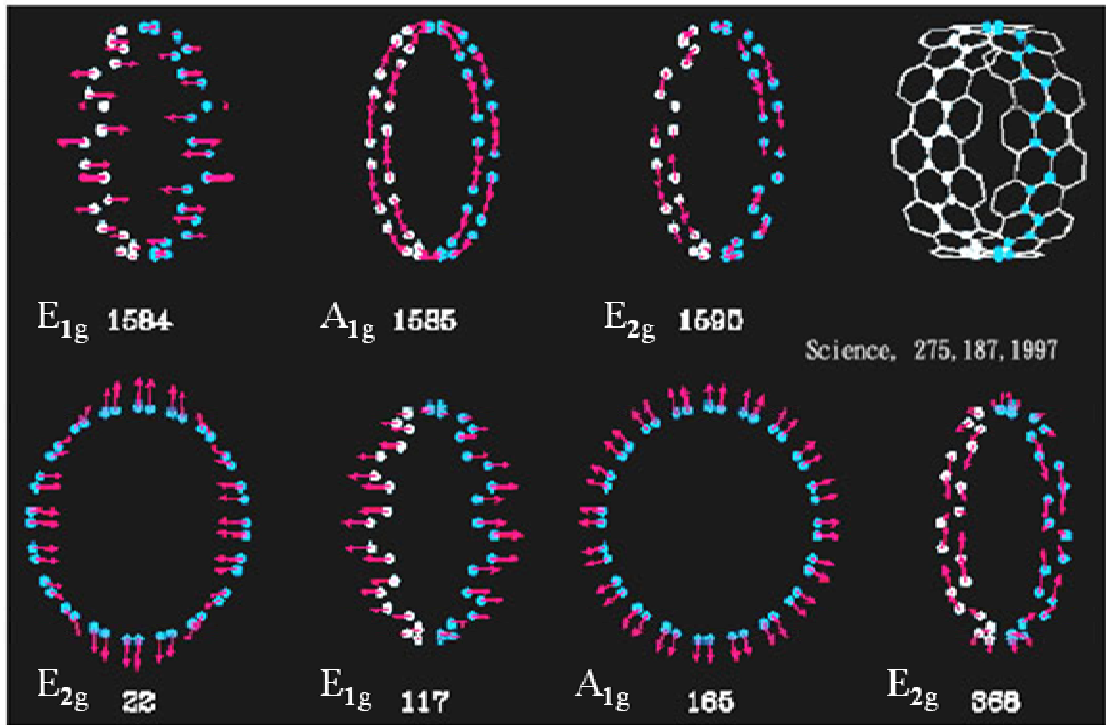
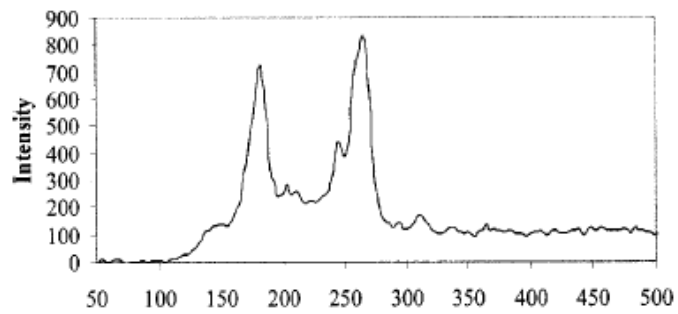
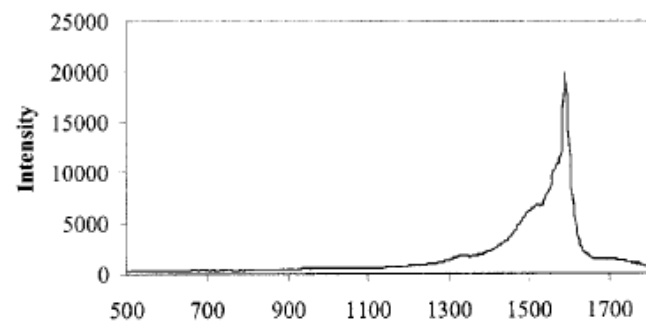


Fig. 2-15 Raman-active normal mode eigenvectors and frequencies for a (10,10) nanotube ^[Rao-1997-187]



(a)



(b)

Fig. 2-16 Raman spectra of SWNTs ^[Raravikar-2002-235424]

2.6 Applications of SWNTs

Many researchers and engineers have been devoted to combine the CNTs with living. There are a lot of possible applications of CNTs products such as FED, field effect transistor (FET), hydrogen storage, etc. Until now, lots of prototypes of these applications have been published. Thus, it is believed that more and more commercial products will be published soon in the future.

(a) Electron field emission elements:

The electron field emission elements, as implied by the name, utilized the field emission properties of CNTs. Among all of them, the closest to our life is FED. It is a next generation display after plasma display panel (PDP) and liquid crystal display (LCD) technologies. The theorem of formation of image is to use CNTs as cathode, then applies the potential between cathode and anode. Electrons emits from cathode to anode with phosphors which generate illumination. Ultra thin, wider view angle, superior brightness and low operation power are main advantages of FED. Samsung corporation had been public the 4.5" FED prototype in 1999 [Fig. 2.17] ^[Choi-1999-3129]. And the electron source like SEM filament or X-ray tube ^[Yue-2002-355] can also employ the CNTs as electron emitters, which possess longer life, small energy spreading and power-saving significantly. Another field emission application related to general public is cathode-ray tube (CRT) lighting elements. The original has been published in 1998 by Ise Electronics corporation, Japan. ^[Saito-1998-L346] The fabricated CRTs are of a triode type, consisting of a cathode (nanotubes field emitter arrays), a grid and an anode (phosphor screen) [Figs. 2.18(a) and 2.18(b)]. The maxima brightness with anode at $200 \mu A$ is 64000 cd/cm^2 . Stable electron emission, adequate luminance and long life (over 10000 hours) are demonstrated. It can be applied to a giant outdoor display or ultra-high quality color CRT displays.

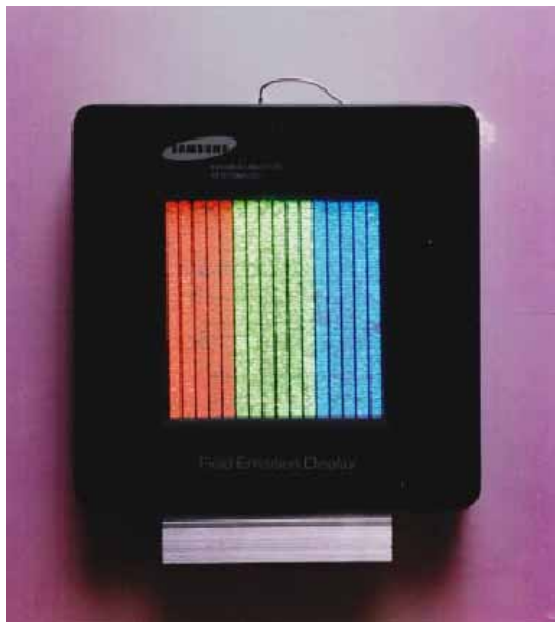


Fig. 2-17 FED display at color mode with red, green, and blue phosphor column. [Choi-1999-3129]

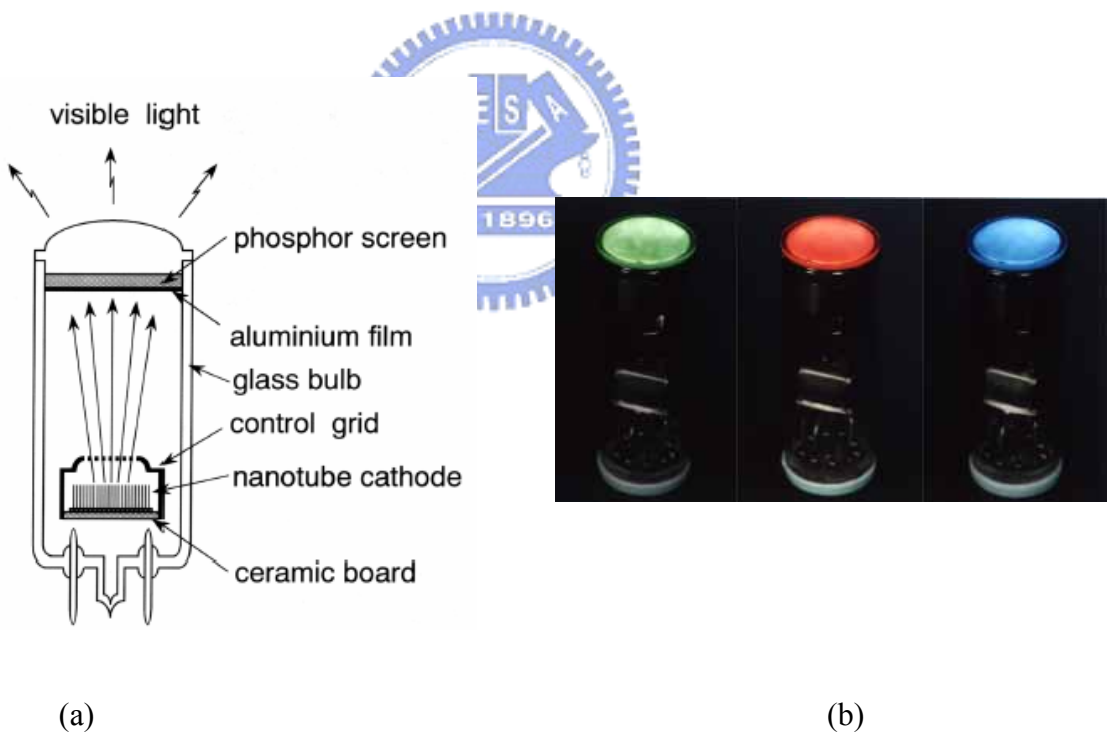


Fig. 2-18 Schematic drawing : (a) and physical object, and (b) of a longitudinal cross section of a CRT fluorescent display with a field emission cathode composed of carbon nanotubes. [Saito-1998-L346]

FET is a very important electronic device in history. The overwhelming majority of FET is silicon or III–V based just because these materials are semiconductors. But some of CNTs also have semiconducting properties, it makes researchers want to fabricate the CNTs based FET. In 1998, Sander reported the room-temperature transistor based on a single SWNTs FET. [Sander-1998-49] Fig. 2.19 shows the I-V curve of the CNT-FET. In 2001, Derycke in IBM corporation prepared both p-type and n-type nanotubes transistors to build the first nanotubes-based logic gates: voltage inverters [Figs. 2.20(a) and 2.20(b)]. [Derycke-2001-453] Surely, it still have lots of complicated problems to mass production above-mention devices, but these results have told that the nano-electronics is not hollow words any more.

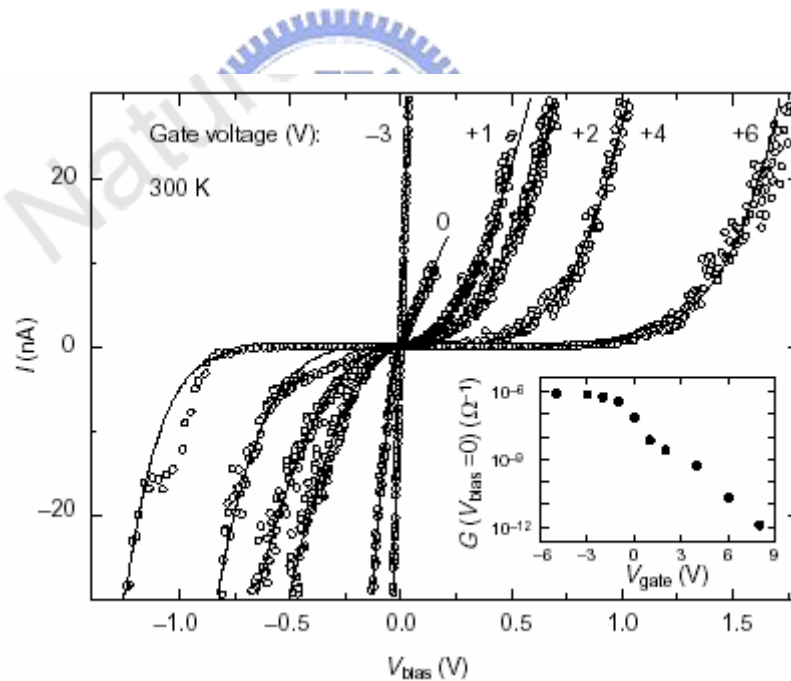


Fig. 2-19 Two probe I- V_{bias} curve for various values of the gate voltage from a CNTs-based FET. [Sander-1998-49]

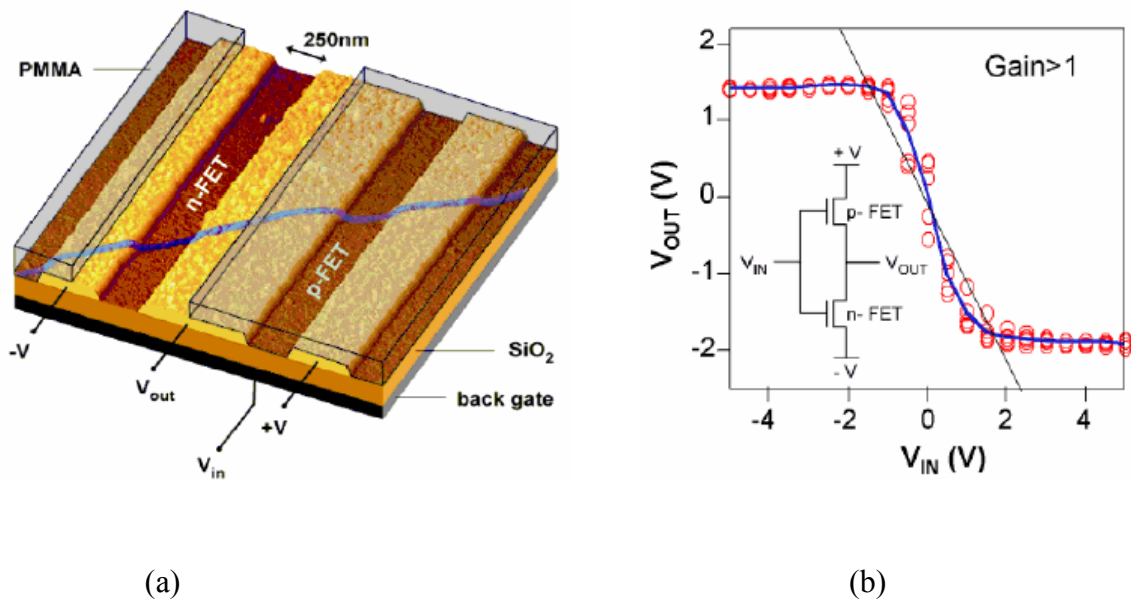


Fig. 2-20 (a) Atomic Force Microscopy (AFM) image shows the design of the voltage inverter, and (b) Characteristics of the resulting intra-molecular voltage inverter. [Derycke-2001-453]

(c) Lithium intercalation

The basic principle of rechargeable lithium batteries is electrochemical intercalation and de-intercalation of Li in both electrodes. An ideal battery has a high-energy capacity, fast charging time and long cycle time. The capacity is determined by the Li saturation concentration of the electrode material. The SWNTs have shown to possess both high reversible and irreversible capacities [Gao-1999-153].

(c) Gas sensor

In 2003, L. Valentini et al. [Valentini-2003-961] revealed that the electrical resistance of CNTs in a device could be reduced through the introduction of NO₂ gas and proposed that the amount of NO₂ can be calculated by the decrease of electrical resistance where sensitivity of 10 ppb was achievable. Furthermore, A. Modi et al. [Modi-2003-171] fabricated a gas sensor device with MWNT-arrays (Fig 2-18) whose accuracy can approach to 25 ppm.

(d) Hydrogen storage material

Face to possible energy-crisis of gasoline, people has started to find the substitution methods for many years. Fuel cell was considered to have potential among all of solutions. Once it does be generated, its use as a fuel that creates neither air pollution nor greenhouse gas emissions. But it needs a huge hydrogen storage capability material. SWNTs just can play this role. SWNTs can absorb higher hydrogen than conventional materials. A H₂ uptake of 4.2 weight %, which corresponds to a H/C atom ratio of 0.52, was obtained by these SWNTs with an estimated purity of 50 weight %. Also, ~80% of the adsorbed H₂ can be released at room temperature. These results indicate that SWNTs are highly promising for H₂ adsorption even at room temperature ^[Liu-1999-1127]. The hydrogen storage mechanisms of CNTs are still not well known yet, and these properties usually occur at high pressure or low temperature environment. It remains impossible to apply on commercial product so far.

(e) Composite materials

The SWNTs may be used as reinforcements in high strength, Low weight, and high performance composites due to their excellent mechanical properties. A main advantage of using SWNTs for structural polymer composites is that SWNT reinforcements will increase the toughness of the composites by absorbing energy during their highly flexible elastic behavior. Other advantages are the low density of the nanotubes, an increased electrical conduction and better performance during compressive load, or induced high thermal conductivity reinforced material.

Application of SWNT-polymer solar cell ^[Kymakis-2002-112] was recently studied because the extremely high surface area, ~1600 m²/g, reported for purified SWNTs ^[Cinke-2002-69], offers a tremendous opportunity for excitation dissociation. Very recently, J. Landi et al. ^[Landi-2005-165] reported a photovoltaic device (Fig. 2-21), which was constructed with P3OT and purified, 95% w/w, laser-generated SWNTs. This P3OT composites were deposited on ITO-coated PET and I-V characterization showed a photo-response with an open-circuit voltage of 0.98 V and a short-circuit current density of 0.12 mA/cm².

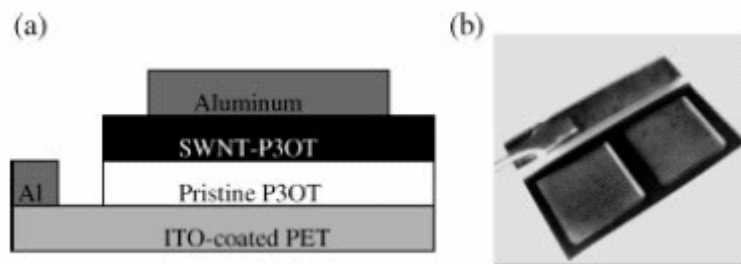


Fig. 2-21 (a) Schematic representation, and (b) image depicting the composition of fabricated SWNT – P3OT flexible solar cells [Landi-2005-165]

(f) Other applications

Atomic Force Microscope (AFM) is employed to obtain the surface morphologies and roughness. It uses a probe scanning the surface of sample, and an incident laser beam irradiates the arm of probe reflecting to a detector which passes signals to computer and draws the images. In order to obtain a high resolution images, the tip must be ultra thin, extremely sharp and high strength. General type of AFM tip is made of Si_3N_4 . The first article that utilized SWNTs as AFM tip was reported in 1996[Fig. 2.22]. [Dai-1996-147] From Fig. 2.23, one can clearly see the SWNTs tip shows the better image resolution. At the same time, SWNTs with excellent mechanical properties can make the damage ratio of tip decrease as low as possible. It has been some commercial products of SWNTs AFM tip at present.

In 1998, Wong demonstrated that CNTs tip can be used for chemical and biological discrimination. [Wong-1998-52] Another possible application applied to biotechnology of medicine carriers are developing as well. In the future, people will easily get to know what disease that we get. Also, people can use CNTs filled with drugs injecting into body, then induce it to the proper position relaxing the medicine to destroy the etiology without hurting normal cell nearby.

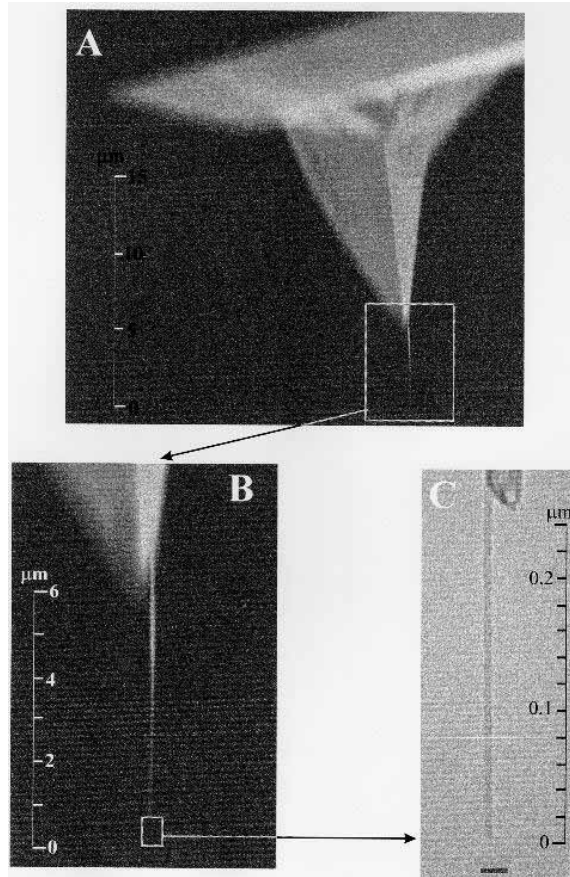
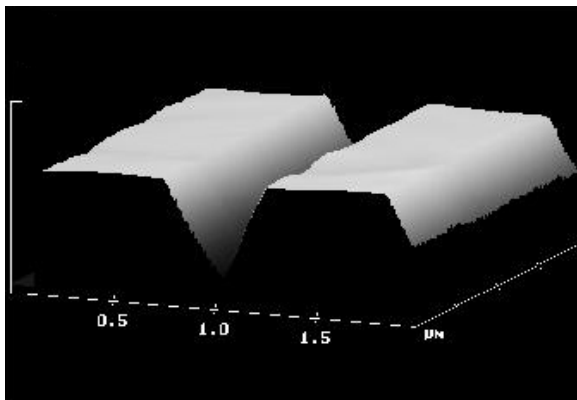
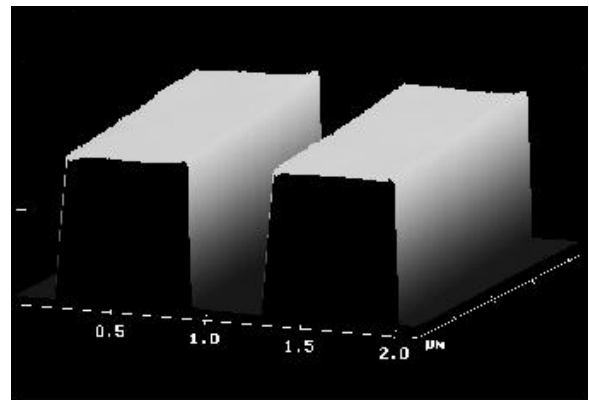


Fig. 2-22 SWNT attached to the pyramidal tip of a silicon cantilever for AFM. [Dai-1996-147]



(a)



(b)

Fig. 2.23 (a) Tapping mode AFM image of a 400-nm-wide, 800-nm-deep trench taken with a bare pyramidal tip, and (b) The image taken with a nanotubes attached to the pyramidal tip with the same specimen. [Dai-1996-147]

Chapter 3

Experimental Methods

3.1 Experimental flowchart

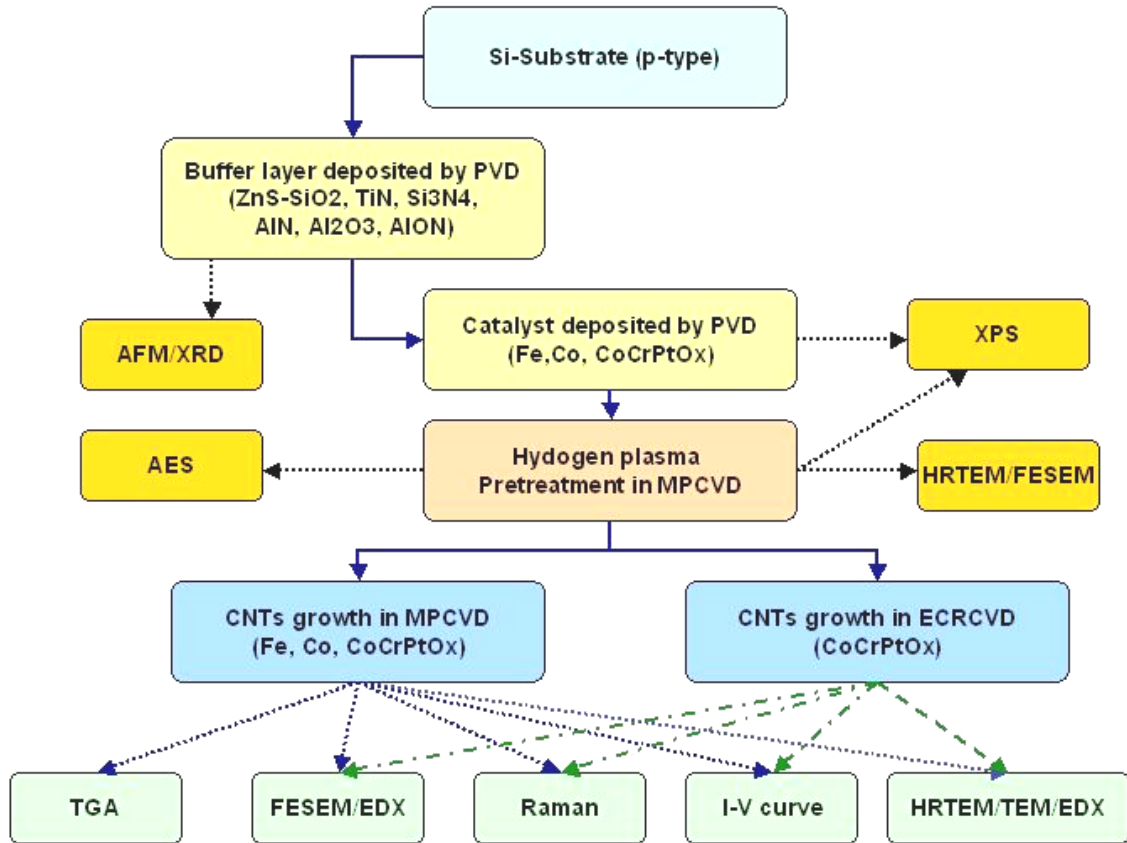


Figure 3-1 Experimental flowchart

Figure 3.1 shows the experimental flowchart for the fabrication and analyses of buffer-layer-assisted single-walled carbon nanostructures (SWNTs) at each process step. Buffer layer and catalyst materials were deposited on Si wafer by physical vapor deposition (PVD). Atomic force microscopy (AFM) and X-ray diffraction (XRD) were utilized to characterize the surface morphologies and structures of as-deposited buffer layer. The binding structures and chemical states of as-deposited catalyst films before and after H-plasma pretreatment were characterized by X-ray photoelectron spectroscopy (XPS). The

morphologies and elemental distributions of catalyst films after H-plasma pretreatment were examined by field emission SEM (FESEM), high resolution transition electron microscopy (HRTEM) and Auger electron spectroscopy (AES). The characteristics of as-grown carbon nanostructures were characterized by HRTEM/TEM, FESEM, Raman spectroscopy, energy-dispersive X-Ray analyses (EDX), field emission measurements (*J-E*) and thermal gravimetric analysis (TGA).

3.2 Raw materials

(a) Substrates: P-type (100) silicon wafer

(b) Source gases:

Source gases used in these experiments include hydrogen (purity 99.9995%), oxygen (purity 99.9995%) and nitrogen (purity 99.998%) from Jian Ren Chemical Co.; methane gas (purity 99.999%) and argon gas (purity 99.9995%) from San Fu Chemical Co.

(c) Targets for buffer layer preparation:

Target materials include ZnS-SiO₂ (80 wt%-20 wt%), Si (p-type), pure Ti (purity 99.999%) and pure Al (purity 99.999%) from Mitsubishi Material Company.

(d) Targets for catalyst precursor film preparation:

Target materials include pure Fe (purity 99.99%), pure Co (purity 99.9998%), CoCrPt (Co 57.08 %, Cr 10.97 %, Pt 31.95 %) and CoCr (Co 67.19%, Cr 32.81%) from Sumitomo Co.

3.3 Deposition of buffer layer and catalyst thin films

P-type (100) silicon wafer was utilized as the substrate. Buffer layer was deposited onto Si wafer and catalyst film was subsequently deposited by physical vapor deposition (PVD). Buffer layer materials (TiN, Si₃N₄, AlN, Al₂O₃ and AlON) were deposited using Al, Ti and Si target under a atmosphere (N₂, O₂ and mixed O₂/N₂), respectively, by DC reactive sputtering

(Unaxis Cube Trio). ZnS-SiO₂ (80-20 wt%) film was deposited by RF- sputtering (Unaxis Cube Trio). Detailed deposition conditions are summarized in Table 3-1.

Catalyst films, Co and Fe, were deposited using pure Co and Fe target by DC sputtering (Helix system). CoCrPtOx and CoCrOx films are deposited by DC reactive sputtering (Helix system) using CoCrPt and CoCr target, respectively, under O₂ atmosphere. Detailed deposition conditions are summarized in Table 3-1.

Table 3-1 Deposition conditions of catalyst and buffer layer thin films

Catalyst or Buffer layer material [#]	Gas flow rate	Power (kW)
ZnS-SiO ₂	Ar, 12 sccm	3.0
Si ₃ N ₄	Ar/N ₂ , 10 sccm / 15 sccm	1.0
TiN	Ar/N ₂ , 10 sccm / 10 sccm	1.0
Al ₂ O ₃	Ar/O ₂ , 15 sccm / 10 sccm	1.0
AlN	Ar/ N ₂ , 15 sccm / 10 sccm	1.0
AlON	Ar/O ₂ / N ₂ , 15 sccm / 2 sccm / 8 sccm	1.0
Co	Ar, 15 sccm	0.4
Fe	Ar, 10 sccm	0.7
CoCrOx	Ar/O ₂ , 10 sccm / 30 sccm	1.0
CoCrPtOx	Ar/O ₂ , 10 sccm / 30 sccm	1.0

[#]Other conditions:

- (1) Pre-sputtering conditions : Ar flow rate, 30 sccm ; pressure, 5×10^{-3} Torr and 20 min pre-sputtering time.
- (2) Working pressure : 2×10^{-3} Torr.

3.4 Design principle of CoCrPtO_x as catalyst precursor

In previous study, small-sized catalyst particle is favorable for SWNT growth, however, how to obtain pretreated catalyst particles with small size and well distribution is still a challenge for CNTs researchers all over the world. In this study, we design a novel catalyst precursor material to achieve the goal of formation of very fine catalyst particles, which is favorable for fabrication of SWNTs. Our design principle is described as below:

The oxidized phase of PtOx is unstable and can be easily reduced to the metallic state in

the form of very fine particles; it has therefore been studied recently in optical storage media and nonvolatile memory applications^{[Kikukawa-2002-4697][Tseng-2004-2595]}. Kim et al.^[Kim-2003-1701] proposed that PtO_x film would decompose to Pt nano-particles and O₂ by laser thermal pretreatment where the decomposition temperature is approximately 500°C. Figures 2-12(a) and 2-12(b) show that PtO_x film was decomposed to form nano-particles after laser pretreatment and transmittance is decreased due to formation of Pt nano-particles and O₂ shown in Fig. 2.13. Additionally, the Ni-Cr alloy was reported to act as catalyst for CNTs growth, indicating that the Cr in the Ni-Cr alloy can be readily oxidized to become Cr₂O₃ to effectively prevent Ni nanoparticles from agglomeration^[Shaijmon-2002-192]. Co is an appropriate element for dissolving carbon species. We take the advantages of these unique characteristics and design a novel oxidized CoCrPt thin film acting a catalyst precursor film to study its feasibility in fabricating SWNTs in this work.

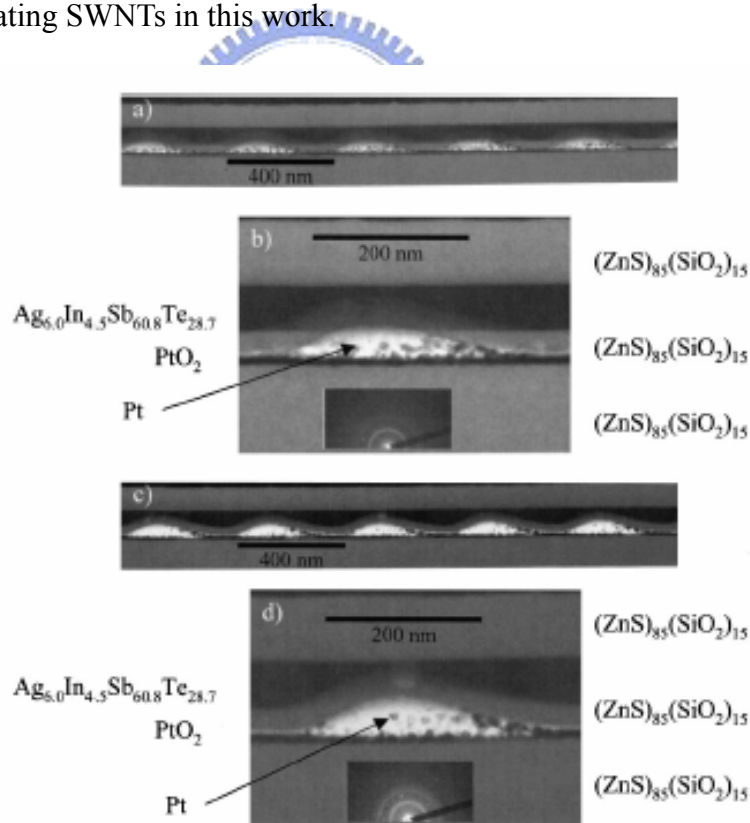


Fig. 3-2 TEM images of PtO_x thin film after laser pretreatment where small-sized self-assembled Pt nanoparticles are formed.^[Kikukawa-2002-4697]

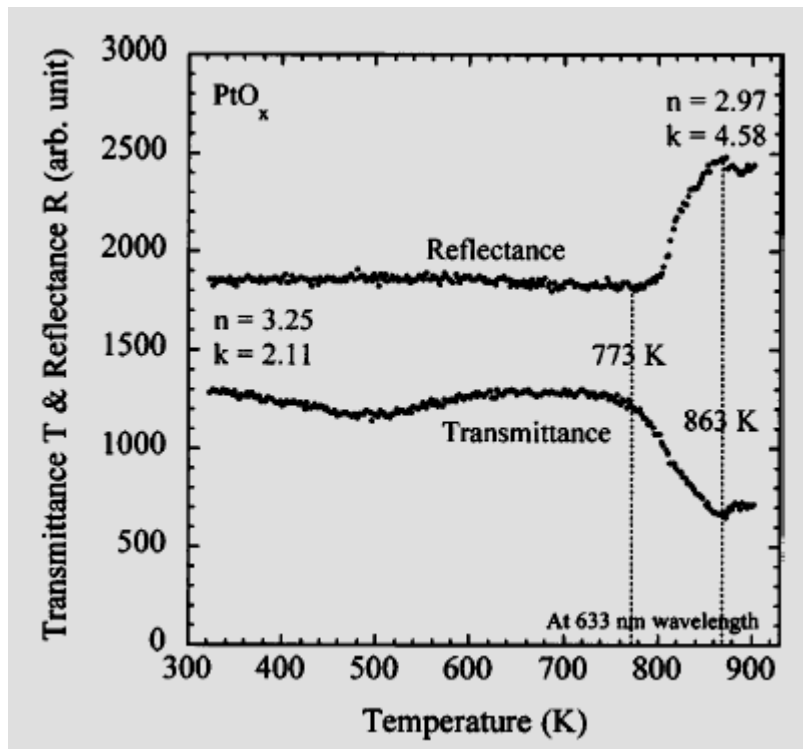


Fig. 3-3 Thermo-optical properties of PtO_x single layer. [Kim-2003-1701]

3.5 Microwave plasma chemical vapor deposition system (MPCVD)

The schematic diagram of MPCVD system is shown in Fig. 3-4. The main components of the system can be divided into six parts: the microwave generator, wave-guides, reaction chamber, gas flow controller, gas pressure controller and pumping system. The 1.3 kW microwave (2.45 GHz) generator from Tokyo electronic Corp. was used. The reaction chamber is a quartz tube (inner and outer diameters = 47 mm and 50 mm, respectively; China Quartz Corp.) in a microwave applicator made of aluminum alloy. The other components of the system include stainless steel specimen loading chamber, stainless specimen holder and rotary pump (Hitachi Corp. Ltd). An upper electrode above the specimen holder can be used for applying the DC bias on the specimen during deposition. A thermal couple embedded in the holder monitors the substrate temperature. Mass flow controller (MKS model 247) is used for metering the flow rates of source gases (Ar , NH_3 , H_2 , CH_4 , C_2H_2). The pressure of the

chamber is monitored by a thermal couple vacuum gauge, and is regulated by APC controller (MKS model 263) through an absolute pressure gauge (MKS Baratron) and a throttling valve. The temperature of the specimens is determined by the microwave power, pressure and the distance to the plasma zone. There is no external heating system.

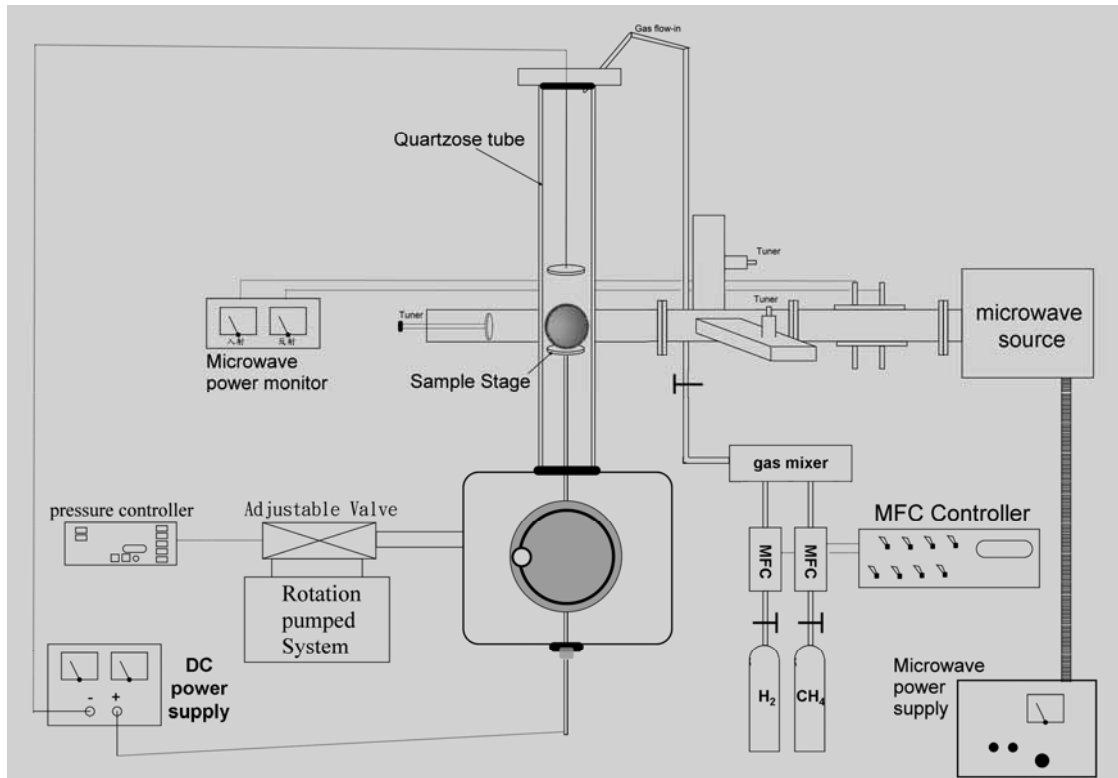


Fig. 3-4 Schematic drawing of MPCVD system

3.6 Electron cyclotron resonance chemical vapor deposition system (ECR-CVD)

The experimental apparatus of Electron Cyclotron Resonance Chemical Vapor Deposition (ECR-CVD) system is shown in Fig.3.5. ECR-CVD system consists of microwave generator (2.45 GHz) which can reach the maximum power of 1200 W, three-spot circulator, tuner, wave guides, microwave applicator, reaction chamber, mass flow controller, electric coils, cooling copper coils, substrate heating stage, vacuum pump, and D.C. bias.

The main advantages of ECR-CVD system include high dissociation efficiency, low deposition temperature of CNTs, wider deposition area. The electronic field E and the

magnetic field B can characterize the ECR-CVD system. In this system, the electrons are accelerated by E to the direction perpendicular to B and orbited in a plane perpendicular to B . The cyclotron radius is r_c .

The working principle is as noted later. When the microwave angular frequency (ω) is identical to the angular frequency of the electron (v / r_c), the electrons will be in phase with the field at either positive or negative E . This phenomenon is so called electron cyclotron resonance (ECR). It will occur when $B = 875$ Gauss for frequency of activated media = 2.45 GHz. The cyclotron radius, r_c , for electrons orbiting in a magnetic field can be expressed by $r_c = m_e v / eB$. These symbols such as v , e , m_e and ω mean the electron velocity (v) component perpendicular to B , the electron charge (coulombs), mass of electron, and the electron angular frequency respectively.

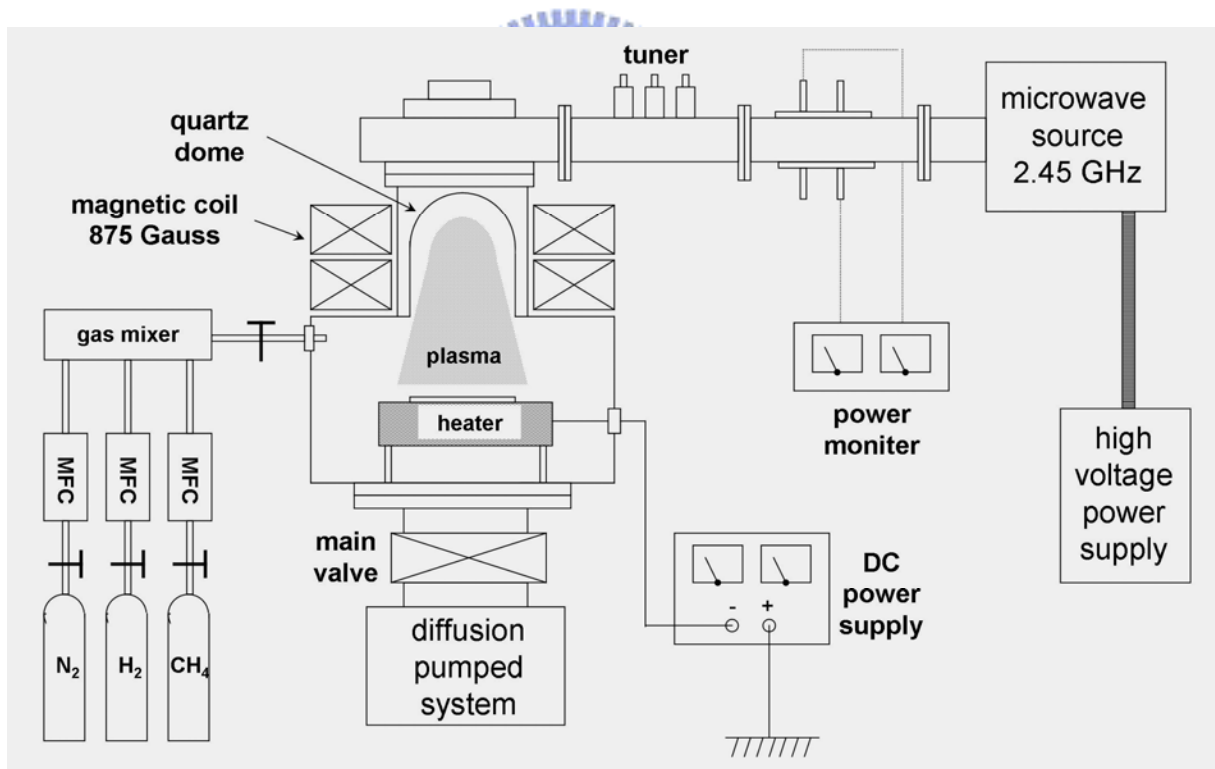


Fig. 3-5 Schematic diagram of ECR-CVD system

3.7 Pretreatment and growth procedures of CNTs

Upward growth of CNTs in this work is not available because catalyst particles are directly etched by H-plasma or poisoned by excess carbon species; thus, we change the stacking position of specimens from upward to downward direction. The specimen stacking sequence is shown in Fig. 3.6, where catalyst-coated substrate is downward and put on the top of Si wafer.

The catalyst-coated substrates were loaded into MPCVD system and hydrogen gas was introduced under a pressure of ~30 Torr forming an H-plasma to heat or etch the coated substrates to obtain the well-distributed catalyst nanoparticles. The sizes of the nanoparticles can be manipulated by adjusting the pretreatment conditions such as microwave power, working pressure, temperature, and H₂ flow rate and process time. The following conditions were used under Co and Fe catalysts: Microwave power 400 W, working pressure 30 Torr, temperature 500°C, H₂ flow rate 100 sccm and process time 10 minutes. The following conditions was used under CoCrPtOx act as precursor catalyst film: Microwave power 600 W, working pressure 30 Torr, temperature 580°C, H₂ flow rate 100 sccm and process time 10 minutes.

Temperature of specimens after H-plasma pretreatment is increased to deposition temperature by adjusting microwave power when H₂ atmosphere and CH₄ are introduced to the chamber for CNTs growth for 6 min. Experimental conditions under Co, Fe and CoCrPtOx thin film as catalyst are listed in Table 3-2, 3-3 and 3-4, respectively.

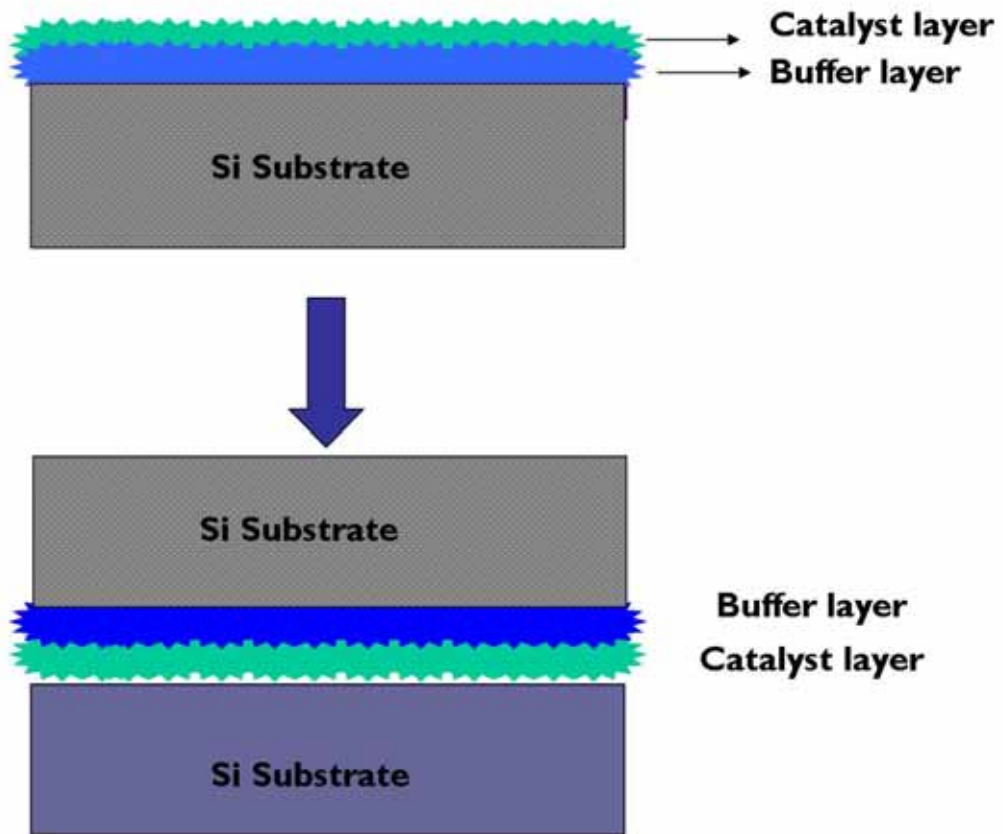


Fig. 3-6 Schematic diagram of specimen stacking sequences

Table 3-2 Specimen designations and their process conditions of the Co-assisted nanostructures on Si wafer with various buffer layer materials by MPCVD.

Specimen designation	Buffer layer materials (10 nm)	Catalyst thickness (nm)	Pressure (Torr)	Substrate temperature (°C)
A1	Native SiO ₂	5	32	~640
A2		10	32	~640
B1	ZnS-SiO ₂	5	32	~640
B2		10	32	~640
C1	Al ₂ O ₃	5	32	~640
C2		10	32	~640
D1	AlN	5	32	~640
D2		10	32	~640
E1	AlON	5	32	~640
E2		10	32	~640
E3	AlON	5	23	~620
E4		5	16	~610

Notes : **MPCVD**

(1) H plasma pretreatment conditions : H₂ flow rate, 100 sccm ; pressure, 30 Torr; microwave power, 400 W; substrate temperature ~ 500°C and 10 min pretreatment time.

(2) The other deposition conditions of CNTs : CH₄/H₂ flow ratio, 5/50 (sccm/sccm) ; microwave power, 800 W ;and 6 min deposition time.

Table 3-3 Specimen designations and their process conditions of the Fe-assisted nanostructures on Si wafer with various buffer layer materials by MPCVD.

Specimen designation	Buffer layer materials	Buffer layer thickness (nm)	Fe Catalyst thickness (nm)	CH ₄ /H ₂ Ratio [#] (sccm/sccm)
FB1	Si ₃ N ₄	10	5	5/50
FC1	TiN	10	5	5/50
FA1				5/50
FA2	Native SiO ₂	10	5	1.5/50
FA3				1.5/100
FA4				5/50
FA5	Native SiO ₂	10	10	1.5/50
FA6				1.5/100
FD1				5/50
FD2	Al ₂ O ₃	10	5	5/50
FD3				1.5/100
FD4				5/50
FD5	Al ₂ O ₃	10	10	5/50
FD6				1.5/100
FE1				5/50
FE2	AlN	10	5	1.5/50
FE3				1.5/100
FE4				5/50
FE5	AlN	10	10	1.5/50
FE6				1.5/100
FD7		5		
FD8	Al ₂ O ₃	10	5	1.5/200
FD9		15		
FE7		5		
FE8	AlN	10	5	1.5/200
FE9		15		
FD10	Al ₂ O ₃	10	1	1.5/200
FE10	AlN	10	1	1.5/200

Notes : **MPCVD**

[#] (1) H-plasma pretreatment conditions : H₂ flow rate, 100 sccm ; pressure, 30 Torr;

microwave power, 400 W; substrate temperature ~ 500°C ; and 10 min pretreatment time.

(2) The other deposition conditions of CNTs : pressure, 16 Torr; microwave power, 800 W; substrate temperature ~ 610°C ; and 6 min deposition time.

Table 3-4 Specimen designations and their process conditions of nanostructures on Si wafer using CoCrPtO_x catalyst precursor, where Co and CoCrO_x are used for comparison.

Specimen designation	Catalyst precursor , (thickness, nm)	Buffer layer (thickness, nm)	Substrate temperature (°C)	Working pressure (Torr)	Growth method ^{#1,2}
G1	CoCrPtO _x , (10)	Native SiO ₂	~ 600	24	MPCVD
G2	CoCrPtO _x , (5)	Native SiO ₂	~ 600	24	MPCVD
G3	CoCrPtO _x , (3)	Native SiO ₂	~ 600	24	MPCVD
G4	CoCrPtO _x , (2)	Native SiO ₂	~ 600	24	MPCVD
G5	CoCrPtO _x , (1)	Native SiO ₂	~ 600	24	MPCVD
G6	CoCrPtO _x , (1)	AlON (10)	~ 600	24	MPCVD
H1	Co, (5)	Native SiO ₂	~ 600	24	MPCVD
H2	CoCrO _x , (5)	Native SiO ₂	~ 600	24	MPCVD
H3	CoCrPtO _x , (5)	Native SiO ₂	~ 600	24	MPCVD
I1	CoCrPtO _x (2)	Native SiO ₂	673	4x10 ⁻³	ECRCVD
I2	CoCrPtO _x (2)	Native SiO ₂	665	4x10 ⁻²	ECRCVD
I3	CoCrPtO _x (2)	Native SiO ₂	662	4x10 ⁻¹	ECRCVD
I4	CoCrPtO _x (2)	Native SiO ₂	658	4	ECRCVD
I5	CoCrPtO _x (1)	Native SiO ₂	658	4	ECRCVD
I6	CoCrPtO _x (1)	AlON (10)	658	4	ECRCVD

Notes :

#1. MPCVD method:

- (1) H-plasma pretreatment conditions : H₂ flow rate, 100 sccm ; pressure, 30 Torr; microwave power, 600 W; substrate temperature ~ 580°C ; and 10 min pretreatment time.
- (2) The other deposition conditions of CNTs : pressure, 24 Torr; microwave power, 750 W; H₂/CH₄ ratio = 50/4 (sccm/sccm) ; substrate temperature ~ 600°C ; and 6 min deposition time.

#2. ECRCVD method:

- (1) H-plasma pretreatment condition: substrate temperature, ~ 630°C ; H₂, 30 sccm ; bias, -30 V ; magnetic field, 875 G ; microwave power, 750 W ; base pressure, ~ 10⁻⁶ Torr ; working pressure, ~ 2x10⁻³ Torr ; pretreatment time, 10 mins
- (2) Other deposition conditions of carbon nano-structures: H₂/CH₄ ratio = 50/4 ; bias, -100 V ; magnetic field, 875 G ; microwave power, 1000 W ; base pressure, ~ 2x10⁻³ Torr ; and 45 min deposition time.

3.8 Structures and properties of analyses

a. Atomic force microscopy (AFM)

AFM measures inter-atomic interactions between a scanning probe tip and the specimen surface. It can generate topographic images for the specimen surface in atomic scale. In addition, due to its superior vertical and horizontal resolution, AFM are very good for roughness measurement. In this study, AFM was employed to measure the average roughness of as-deposited buffer layer where a 5x5 μm^2 area was scanned. VEECO (DI3100) and Asylum Research (MFP3D ORCA) performed AFM analyses with the tapping mode.

b. X-ray diffraction (XRD)

The diffraction angle and the associated peak intensity are the unique characteristic of crystalline materials. Therefore, by using the XRD method, various crystal structure information of the specimen can be determined. XRD θ - 2θ scan and rocking curve were utilized to investigate the preferred orientation and crystal quality of the specimens, respectively. In this study, XRD (Shimadzu XRD-6000) was used to examine the crystal structure of as-deposited buffer layer films where the Cu-K α line at 0.1541 nm was used as the source for diffraction.

c. Scanning electron microscopy (SEM)

SEM is a very useful tool for observing surface morphology of specimen. SEM has secondary electrons or backscattered electrons detectors passing the signal to computer and forming image. In this study, the surface morphologies of catalyst film after pretreatment and as-grown carbon nanostructures were characterized by a focused ion beam & field emission SEM (FIBSEM/FESEM).

d. Transmission electron microscopy (TEM)

TEM image is the result of electron transmitting through the specimen. TEM reveals the interior microstructure of the specimen, and it can give the high-resolution lattice image and the electron diffraction pattern as well. In this study, morphologies of as-grown SWNTs, cross-sectional view and top-view of pretreated CoCrPtOx film were characterized by HRTEM (JEOL, JEM-2010F) operating at 200 kV accelerating voltage to examine the diameters of nano-particles and SWNTs, where the magnification is ranging from 50 k to 100 k. Cross-sectional specimens for the TEM analysis were prepared by mechanical polishing and subsequent argon ion milling.

e. Raman spectroscopy (Raman)

Raman spectroscopy was used to examine bonding structure of as-grown carbon nanostructures of the specimens. For carbon-based materials, there are two obvious bands located at about 1330 cm^{-1} (*D* band) and 1590 cm^{-1} (*G* band), which correlate with the vibration of sp^3 -bonded and sp^2 -bonded carbon atoms, respectively. Additionally, the special radial breathe mode (RBM) in the Raman spectrum is a unique feature to prove the presence of SWNTs. Since RBM peaks involve a collective vibration movement of the carbon atoms towards and away from the central axis of a SWNT, the associated RBM wavelength and frequency are directly related to the diameter of the nanotubes. A Jobin Yvon LABRAM HR Micro-Raman system with a He-Ne laser (wavelength: 632.8 nm) was utilized to study the structural characterization of the SWNT in the experiments.

f. X-ray photoelectron spectroscopy (XPS)

Surface analysis by XPS involves irradiating a solid in vacuum with mono-energetic soft X-rays and analyzing the emitted electrons by energy. The spectrum is a plot of the number of detected electrons per energy interval versus their kinetic energy. Quantitative data can be

obtained from peak height or peak areas, and identification of chemical states often can be made from exact measurement of peak positions and separations. In this study, XPS was employed to characterize binding energy and chemical state of the ultra-thin as-deposited CoCrPtO_x film before and after H-plasma pretreatment. XPS analyses were performed on ESCA system (VG Scientific, Microlab 350) with Al-K α (1486.6 eV) excitation. X-ray emission energy was 400 W with 15 kV accelerating voltage. Argon ion with ion energy of 5 keV was used for sputter profiling.

g. Energy-dispersive X-Ray analyses (EDX)

EDX is used to identify the elemental composition of samples. The EDX analysis system works as an integrated feature of SEM or TEM. In the experiment, the elemental composition of CoCrPtO_x film and as-grown Fe-catalyst CNTs were characterized by TEM/EDX (Philips, TECNAI 20) and FESEM/EDX (Hitachi S-4700), respectively.



h. Auger electron spectroscopy (AES)

AES analysis technique employs an electron beam (2-30 keV) irradiating the specimen surface to excite Auger electrons, which possess specific energy. Through assaying the kinetics energy of the Auger electrons by an electron energy analyzer, one can get to know the element composition and chemical state of the specimen. Since the incident electrons with low-energies have very short inelastic mean free paths inside the solid phase materials, AES is usually used to identify the information within 50 Å away from the surface. In this study, Auger depth analysis was employed to investigate the elements distribution in Fe/AlN coated substrate after pretreatment.

i. Field emission measurements (*J-E*)

The measurements were conducted by the simple diode configuration and carried out in a high vacuum chamber pumped down to a pressure of about 10^{-6} Torr with a turbo molecular pump, backed up by a rotary mechanical pump. Figure 3.7 shows the instrument setup and the test configuration used during field emission characterization. A steel probe with a diameter of 1.8 mm as anode was used for the measurement. The distance between the specimen and anode was about $100\ \mu\text{m}$ controlled by a precision screw meter, and effective field emission area of the specimen was $0.025\ \text{cm}^2$. The specimen (cathode) was biased with a voltage swept positively from 0 to 1000 V at room temperature to extract electrons from emitters. A high voltage source-measure unit (Keithley 237) was used for providing the sweeping electric field (E) and monitoring the emission current density (J). The measurement instruments are auto-controlled by the computer. Prior to the field emission measurement, a high constant voltage of about 600 V was applied to the emitters to exhaust the adsorbed molecules.

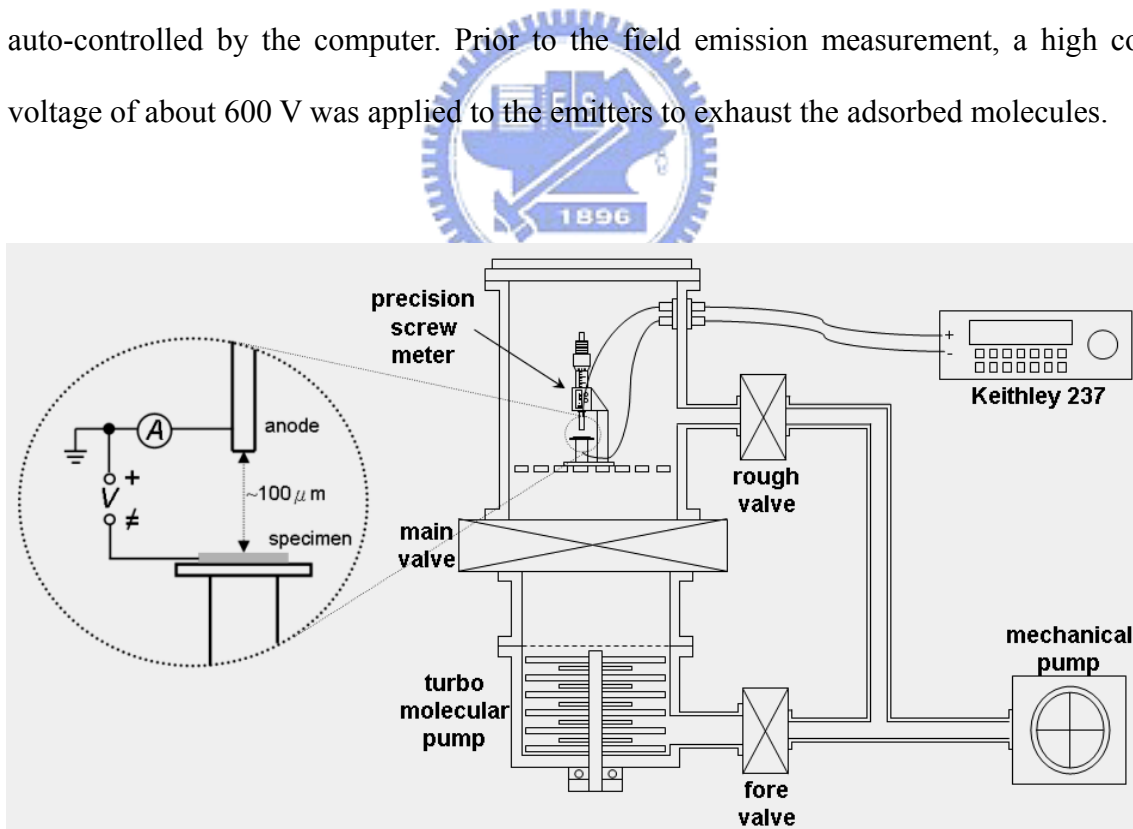


Fig. 3-7 Schematic diagram of the field emission measurement setup

j. Thermal gravimetric analysis (TGA)

In this experiment, Shimadzu TGA-50 was implemented on 5 mg of the as-grown SWNTs. SWNT films were removed from the silicon substrate by razor blade and place into the alumina cell. Set the initial weight reading to 100%, and then initiate the heating program with a 10°C/min ramp rate under air gas environment (air, 30 sccm/min.).



Chapter 4

Result and Discussion

4.1 Characteristics of buffer layer

The surface structure of as-deposited Al_2O_3 、 AlN 、 $\text{Al}_{0.405}\text{O}_{0.450}\text{N}_{0.145}$ 、 ZnS-SiO_2 、 TiN and Si_3N_4 films are characterized by X-ray diffraction and AFM, respectively. The X-ray diffraction results show that all as-deposited buffer films are amorphous state. The roughness (R_{ms} and R_{max}) of as-deposited buffer films on Si wafer is summarized in Table 4.1. AlON with 5 nm thickness demonstrates highest value and AlN shows lowest roughness either in 5 nm and 10 nm. Figures 4-1 to 4-4 illustrate the AFM morphologies of native SiO_2 , as-depositd AlN, AlON, and Al_2O_3 buffer layers with thickness of 10 nm, respectively. AlON and Al_2O_3 show very rough surface with numerous mesoporous pore sizes. In contrast, AlN is quite neat and similar to native SiO_2 .

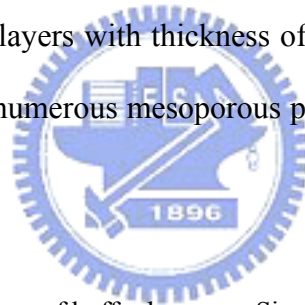


Table 4-1 Surface roughness of buffer layers on Si wafer (AFM)

Buffer layer materials	Buffer layer thickness (nm)	Mean Square Roughness (R_{ms} , nm)	Max. Roughness (R_{max} , nm)
Si_3N_4	10	~0.25	~1.69
TiN	10	~0.14	~0.81
Al_2O_3	5	~0.22	~1.02
	10	~0.37	~1.55
AlN	5	~0.10	~0.37
	10	~0.12	~0.48
$\text{Al}_{0.405}\text{O}_{0.450}\text{N}_{0.145}$	5	~0.42	~1.93
	10	~0.29	~0.97

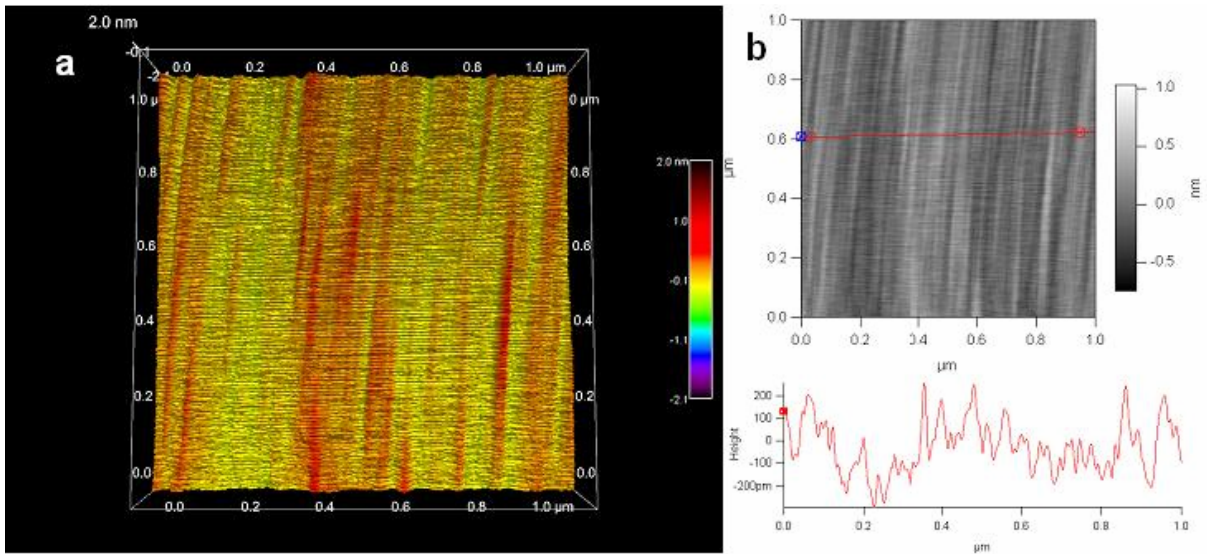


Fig.4-1 AFM images of the native SiO₂ on Si wafer. : (a) top-view, and (b) scanning profile of roughness.

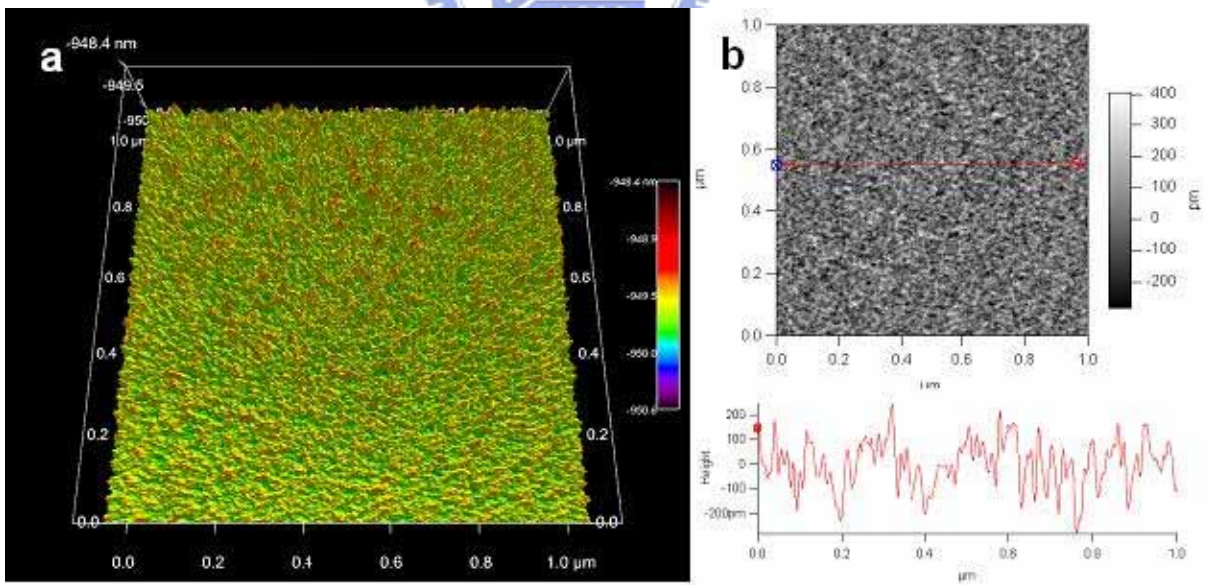


Fig.4-2 AFM images of the as-deposited AlN on Si wafer. : (a) top-view, and (b) scanning profile of roughness.

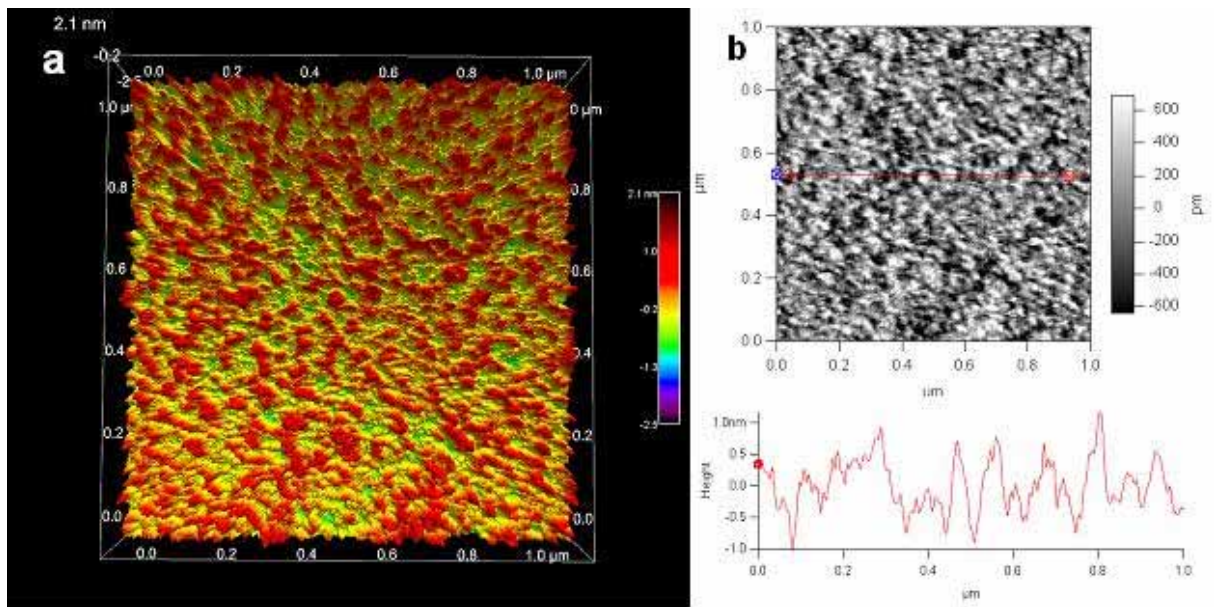


Fig.4-3 AFM images of the native Al_2O_3 on Si wafer. : (a) top-view, and (b) scanning profile of roughness.

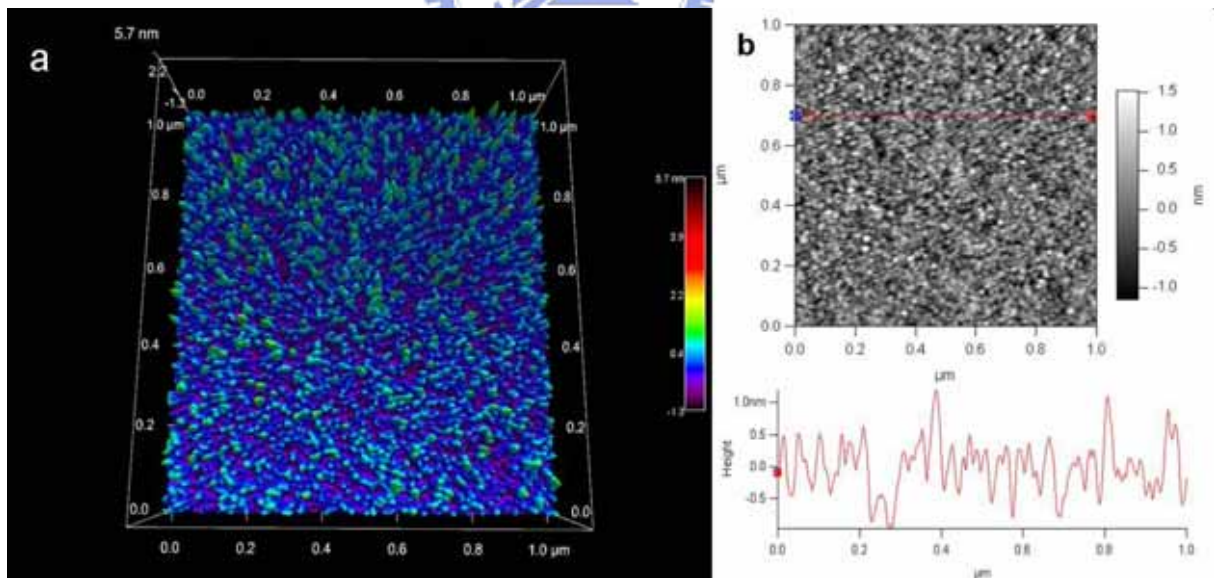
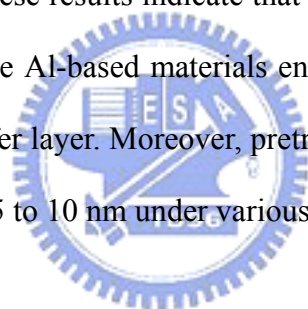


Fig.4-4 AFM images of the native AlON on Si wafer. : (a) top-view, and (b) scanning profile of roughness.

4.2 Morphologies of nanostructures after hydrogen plasma pretreatment

4.2.1 Morphologies of pre-treated Co catalyst films by MPCVD

This study used five buffer layer materials (native SiO₂, ZnS-SiO₂, Al₂O₃, AlON, AlN) with Co catalyst films of 5 nm and 10 nm, respectively. Figures 4-5 and 4-7 illustrate the FESEM morphologies of Co films with thickness of 5 and 10 nm after H-plasma pretreatment, respectively, under different buffer layer materials. In the case of Co film with 5 nm thickness, the catalyst particles size after pretreatment are in order of AlON \approx Al₂O₃ (60 nm) > AlN (45 nm) > ZnS-SiO₂ \approx native SiO₂ (35 nm). In case of 10 nm Co films, the catalyst particles size after pretreatment are in order of AlON \approx Al₂O₃ (180 nm) > AlN (160 nm) > ZnS-SiO₂ (120 nm) > native SiO₂ (50 nm). These results indicate that buffer layer material will influence the pre-treated particle sizes, where Al-based materials enlarge particle size and ZnS-SiO₂ show similar size as native SiO₂ buffer layer. Moreover, pretreated particles size become larger with increase of Co thickness from 5 to 10 nm under various buffer layers application.



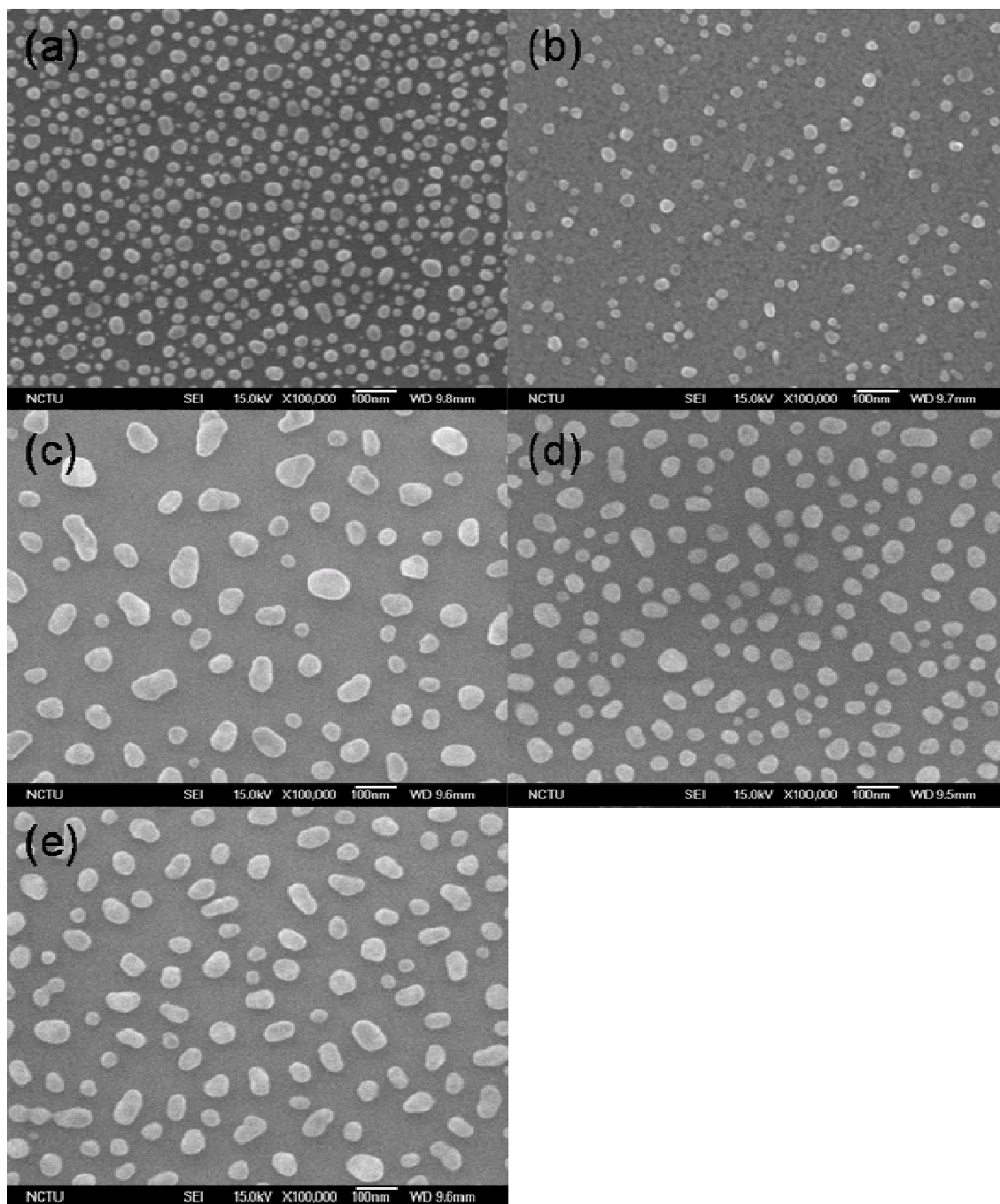


Fig.4-5 SEM micrographs of the Co catalyst films (5 nm) after H-plasma pretreatment on silicon wafers with various materials as buffer layers : (a) native SiO_2 , (b) ZnS-SiO_2 , (c) Al_2O_3 , (d) AlN , and (e) AlON , respectively.

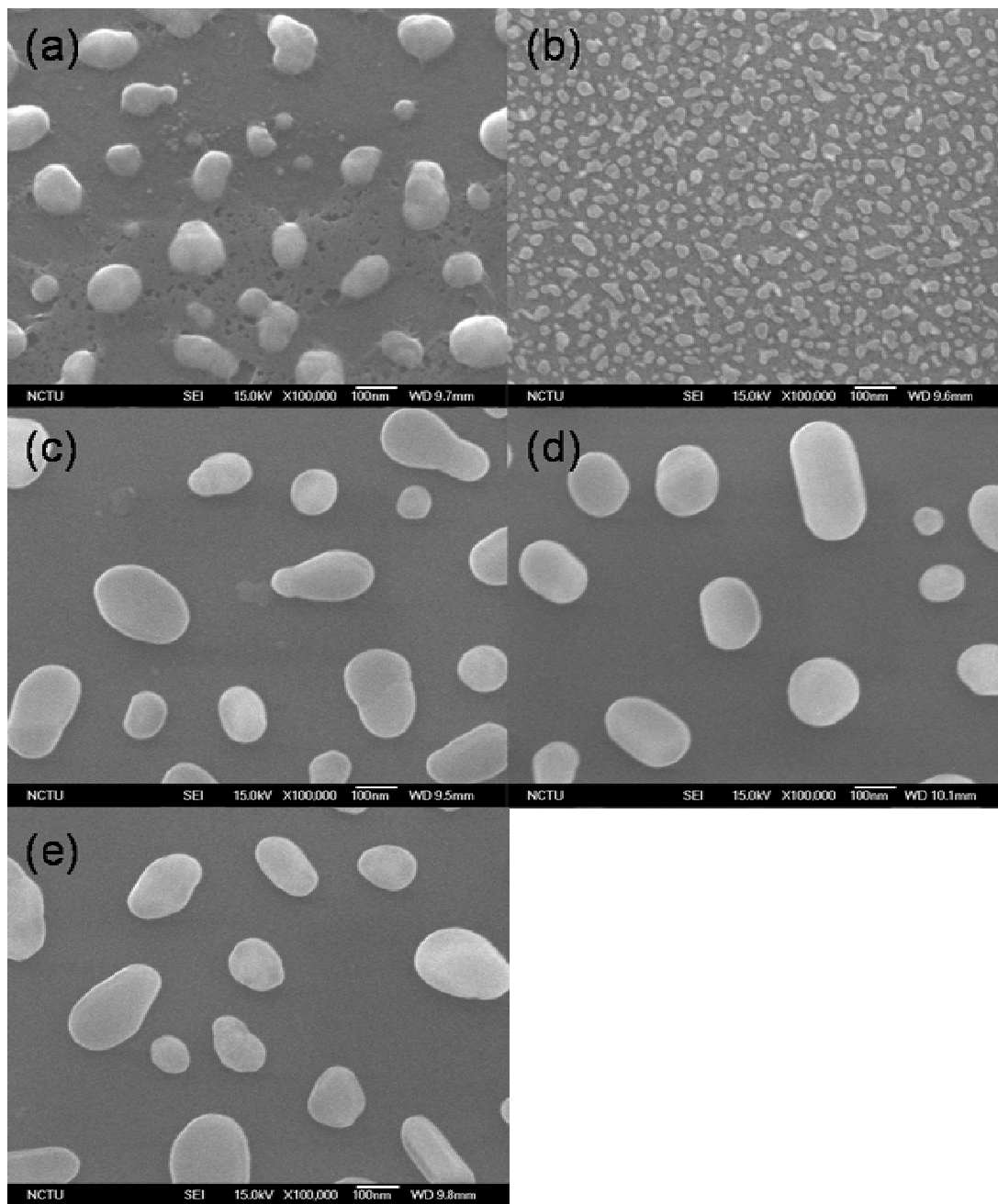
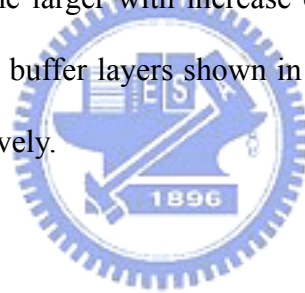


Fig.4-6 SEM micrographs of the Co catalyst films (10 nm) after H-plasma pretreatment on silicon wafers with various materials as buffer layers : (a) native SiO_2 , (b) ZnS-SiO_2 , (c) Al_2O_3 , (d) AlN , and (e) AlON , respectively.

4.2.2 Morphologies of pre-treated Fe catalyst films by MPCVD

This study used five buffer layer materials (native SiO_2 , Si_3N_4 , TiN, Al_2O_3 , AlN) with Fe catalyst films of 5 nm and 10 nm, respectively. Figures 4-7 and 4-8 illustrate the FESEM morphologies of Fe films with thickness of 5 and 10 nm after H-plasma pretreatment, respectively, with different materials as buffer layers. In the case of Fe films with 5 nm thickness, well-distributed particles are formed in the Figs. 4-7(a), (d) and (e) for Specimens with native SiO_2 , Al_2O_3 and AlN materials as buffer layer materials, whose sizes are 30 nm, 23 nm and 15 nm, respectively. By contrast, no well-dispersed nanoparticles are formed with Si_3N_4 and TiN as buffer layers. These results indicate that buffer layer material will influence the pretreated particle sizes, in which Al-based materials effectively enhance the formation of well-distributed and small-sized particle, and Si_3N_4 , TiN show hardly effect. Besides, pretreated particles size become larger with increase of Fe thickness from 5 to 10 nm with native SiO_2 , Al_2O_3 and AlN as buffer layers shown in Figs. 4-8, where particle sizes are 100 nm, 30 nm and 25 nm, respectively.



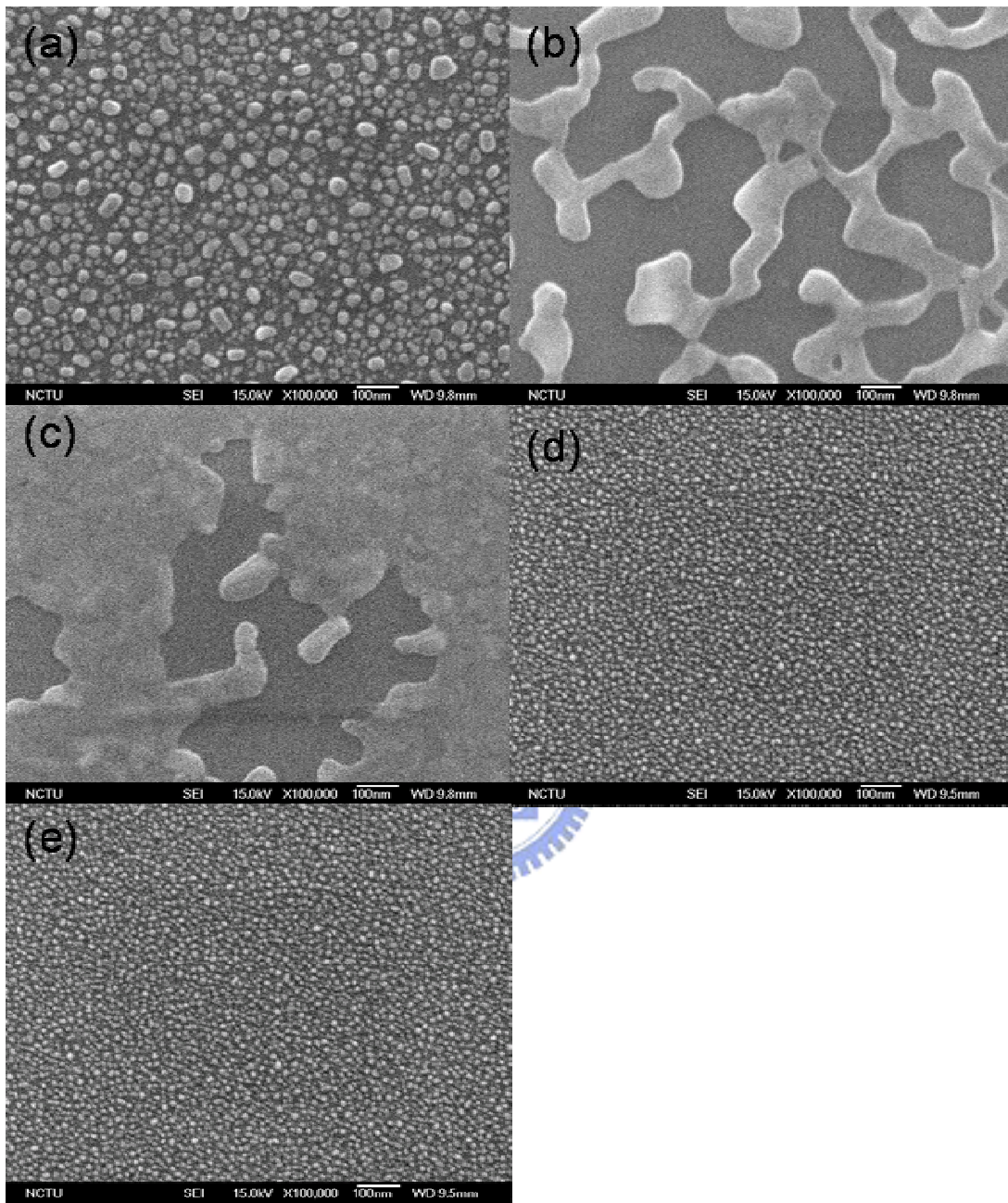


Fig.4-7 SEM micrographs of the Fe catalyst films (5 nm) after H-plasma pretreatment on silicon wafers with various materials as buffer layers : (a) native SiO₂, (b) Si₃N₄, (c) TiN, (d) Al₂O₃, and (e) AlN, respectively.

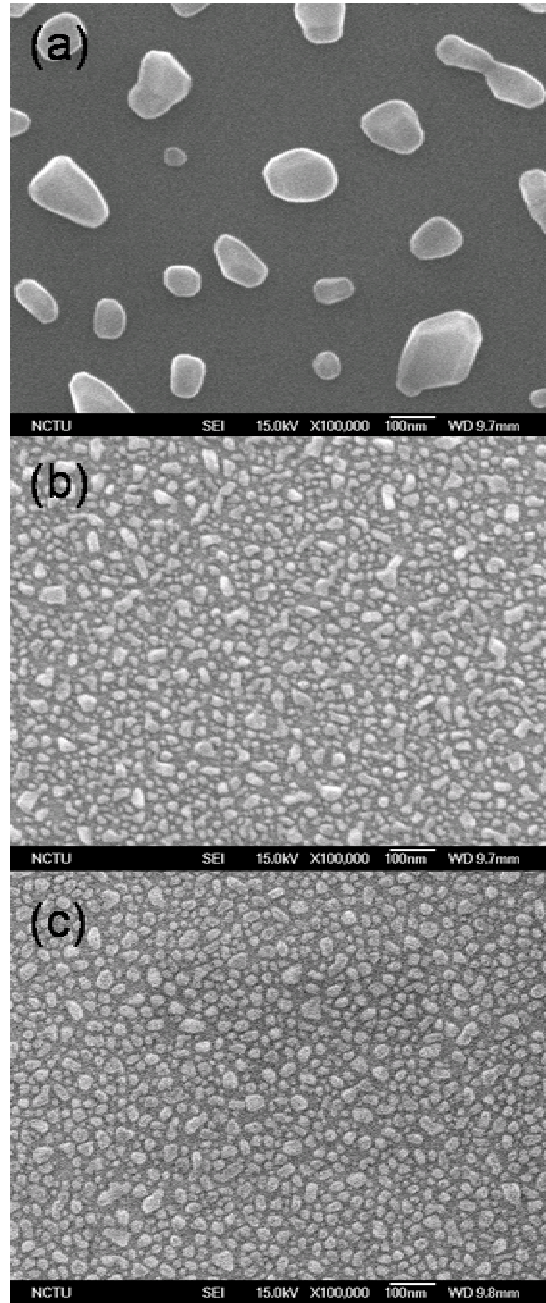


Fig.4-8 SEM micrographs of the Fe catalyst films (10 nm) after H-plasma pretreatment on silicon wafers with various materials as buffer layers : (a) native SiO₂, (b) Al₂O₃, and (c) AlN, respectively.

4.2.3 Morphologies of pre-treated CoCrPtO_x films by MPCVD

Figure 4-9 illustrates the typical FESEM morphologies of the pretreated CoCrPtO_x precursor films on silicon wafers with native SiO₂ buffer layer application and with various catalyst precursor thicknesses: (a) 10 nm, (b) 5 nm, (c) 3 nm, (d) 2 nm, (e) 1 nm and (f) 1 nm, respectively, except Fig. 4.10 (f) with 10 nm AlON as buffer layer. It indicates that the average catalyst size after pretreatment becomes smaller as decrease of catalyst precursor thickness, moreover, the specimen with AlON buffer layer demonstrates the smallest particles whose size is difficult to define due to resolution limitation of FESEM. It is believed that very fine and uniform distributed catalyst particles are formed after H-plasma pre-treatment. In order to examine this assumption, top-view and cross-sectional HRTEM micrographs of the H-plasma pretreated catalyst particles (catalyst film is 1 nm) with no buffer layer and AlON buffer layer are shown in Figs. 4-10 and 4-11, respectively.

Figure 4-10(a) demonstrates that high density and well-distributed nanoparticles are synthesized, consistent with our earlier assumption. The cross-sectional HRTEM in Fig. 4-10 (b) confirms that the native SiO₂ layer (~3 nm) is formed above the Si substrate and the catalytic particles have a diameter of around 2.5 to 3.5 nm. Figures 4-11(a) and (b) present cross-sectional HRTEM micrographs of samples with AlON as buffer layer following H-plasma pre-treatment was compared with that with native SiO₂ as buffer layer. The cross-sectional HRTEM in Fig. 4-11 (b) indicates that the catalytic particles are trapped in buffer layer and have a smaller diameter of around 1 to 3.5 nm.

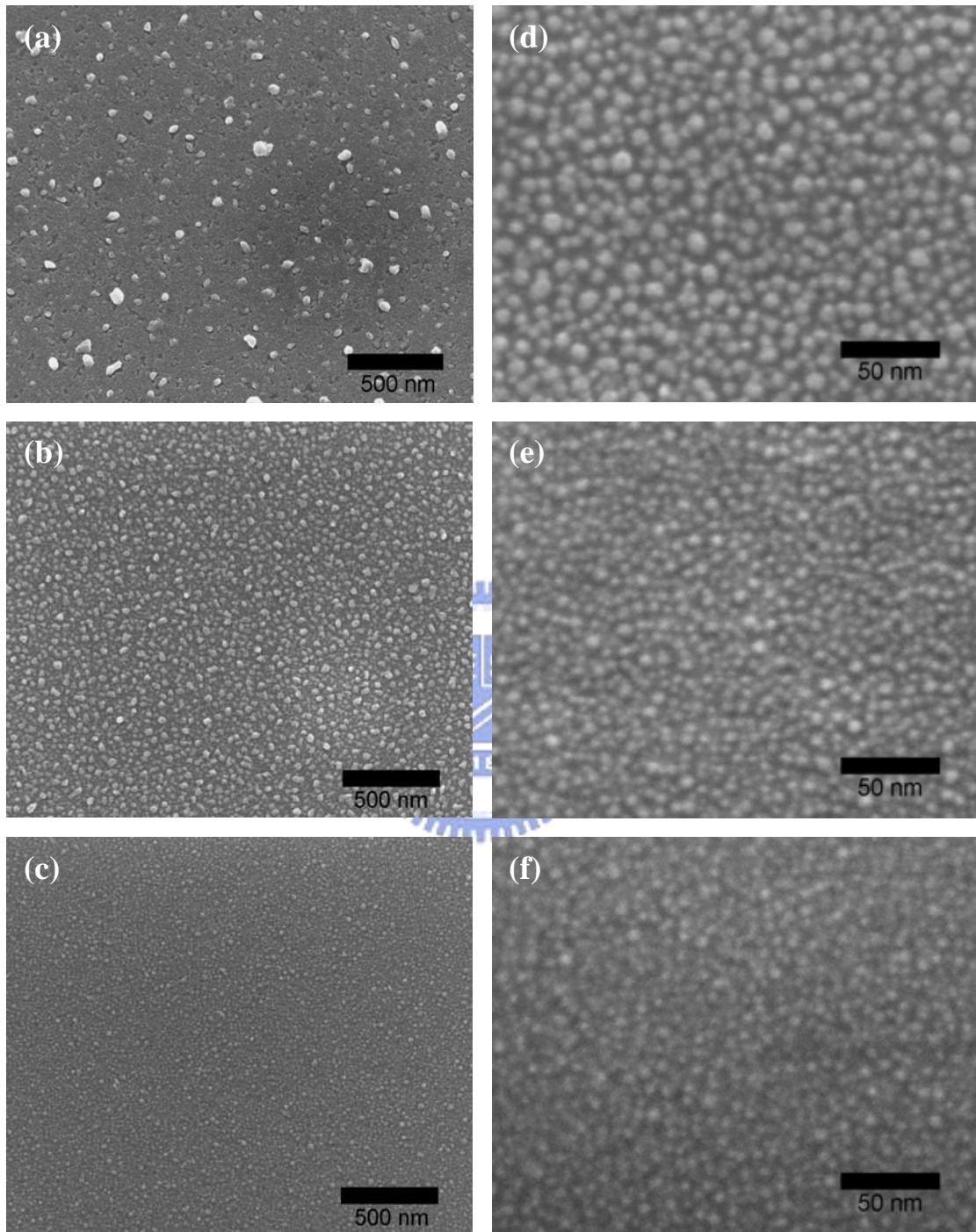


Fig.4-9 SEM micrographs of the CoCrPtO_x precursor films with various thickness after H-plasma pretreatment on silicon wafers with native SiO_2 as buffer layer : (a) 10 nm, (b) 5 nm, (c) 3 nm, (d) 2 nm, (e) 1 nm, and (f) 1 nm, respectively, except (f) with 10 nm AlON as buffer layer.

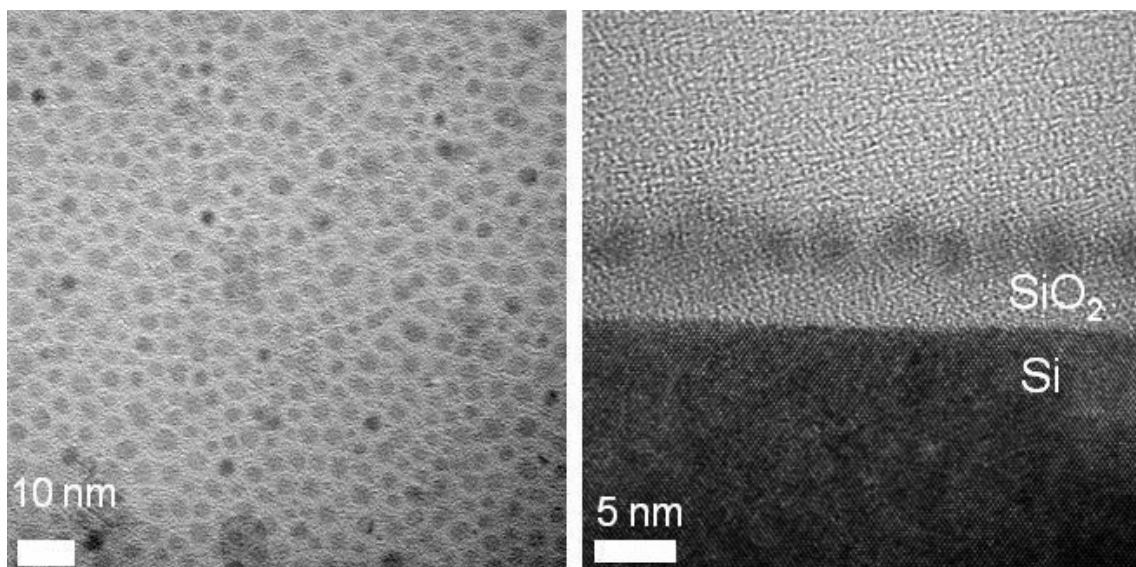


Fig.4-10 (a) Top-view HRTEM micrograph of CoCrPtO_x precursor nanoparticles following H-plasma treatment, showing uniform and close arrangement. (b) The cross-sectional HRTEM micrograph indicates that the sizes of the nanoparticles range from 2.5 to 3.5 nm.

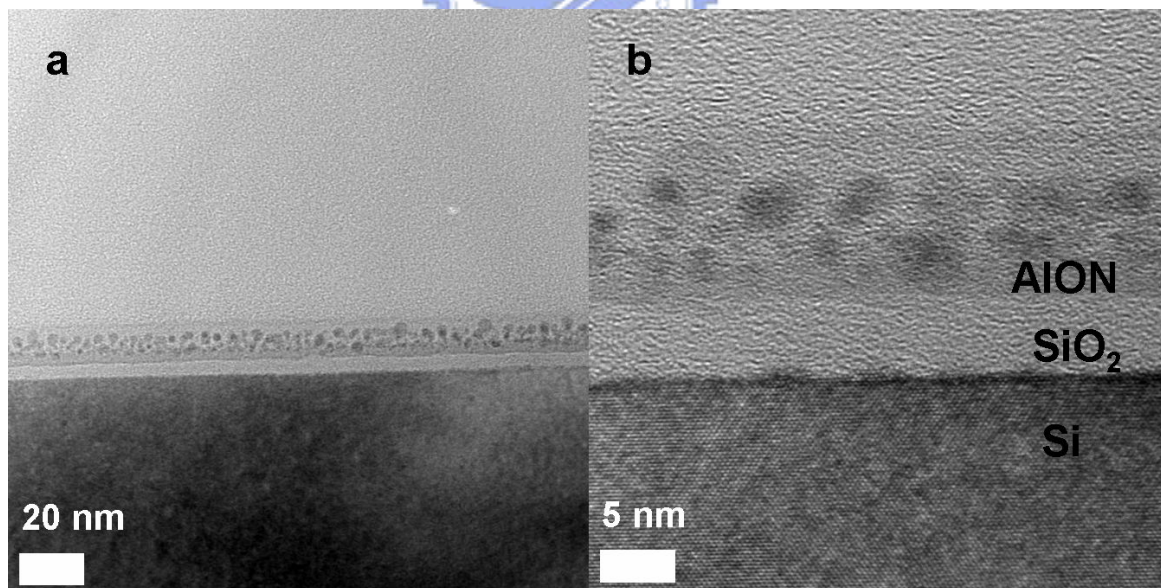


Fig.4-11 (a) The cross-sectional HRTEM micrograph of CoCrPtO_x precursor nanoparticles following H-plasma treatment, showing close arrangement and highly distribution density, and (b) the highly magnified image in (a) indicates that the sizes of the nanoparticles range from 1.0 to 3.5 nm.

4.2.4 Morphologies of pre-treated CoCrPtO_x films by ECRCVD

Figures 4-12(a) to (c) present the FESEM morphologies of the nanostructures of Specimens after H-plasma pretreatment by ECRCVD with different catalyst thickness: (a) 2 nm, (b) 1 nm, and (c) 1 nm with AlON buffer layer. The wafers in Figs. 1(a) and 1(b) for Specimens with 2 nm and 1 nm thickness illustrating that very fine and well distributed particles are formed. Furthermore, no particles are observed in specimen with buffer layer because of FESEM resolution. It is believed that smaller sized particles are formed due to buffer layer effect. These results are in agreement with those fabricated by MPCVD.

Top-view HRTEM micrographs of the H-plasma pretreated catalyst particles (catalyst film is 1 nm) with no buffer layer and AlON buffer layer are shown in Figs. 4-13 and 4-14, respectively. Figure 4-13(a) to (b) demonstrate that small-sized particles with non-uniform diameter (2~6 nm) are synthesized. The HRTEM in Fig. 4-14 (a) to (b) indicate that the well-distributed pretreated particles with uniform sizes (2~4 nm) are formed under AlON buffer layer. These results suggest that buffer layer obviously affect the distribution conditions and size of pre-treated particles.

From previous results, it is concluded that buffer layer materials will strongly affect the nanostructures of Co, Fe and CoCrPtO_x film after H-plasma treatment and their average pre-treated catalyst size are summarized in Table 4-2.

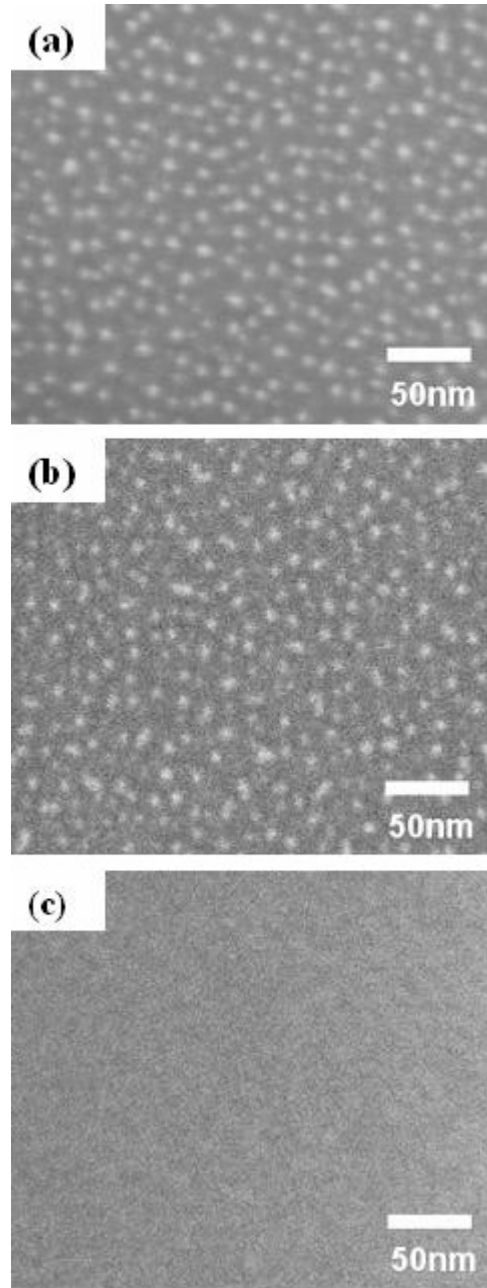


Fig.4-12 SEM micrographs of the CoCrPtO_x precursor with various thickness following H-plasma pretreatment by ECRCVD on silicon wafers with native SiO_2 as buffer layer : (a) 2 nm, (b) 1 nm, and (c) 1 nm, with 10 nm AlON as buffer layer, respectively.

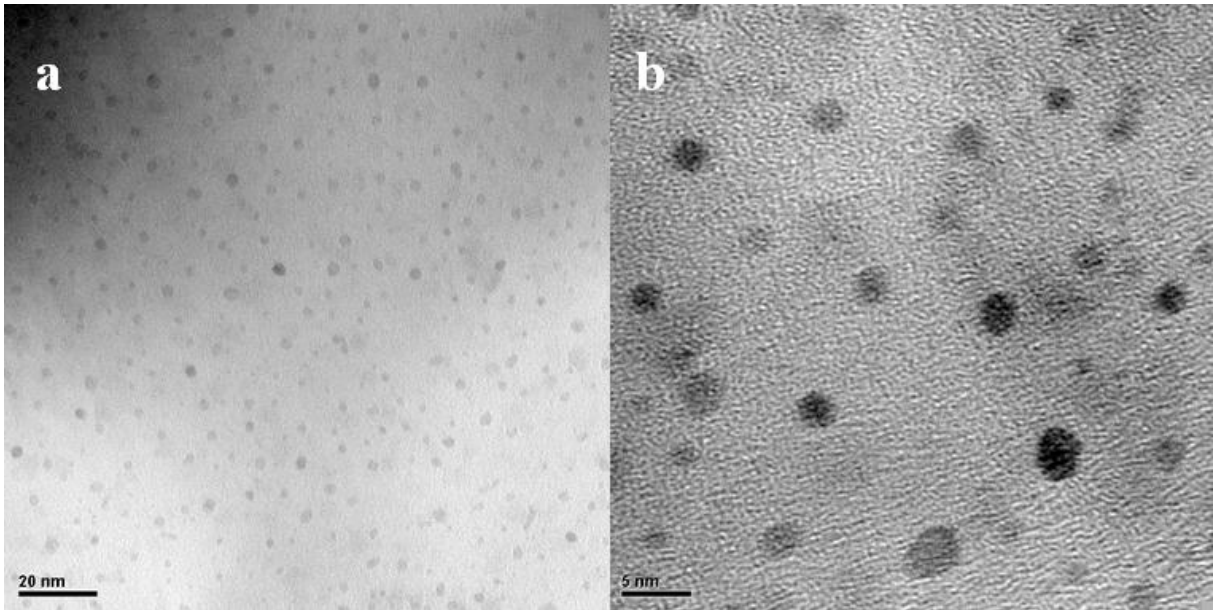


Fig.4-13 (a) The top-view HRTEM micrograph of CoCrPtO_x precursor nanoparticles (with native SiO₂ as buffer layer) following H-plasma treatment by ECRCVD, showing a dispersed distribution density, and (b) the highly magnified image in (a) indicates that the sizes of the nanoparticles range from 2.0 to 6.0 nm.

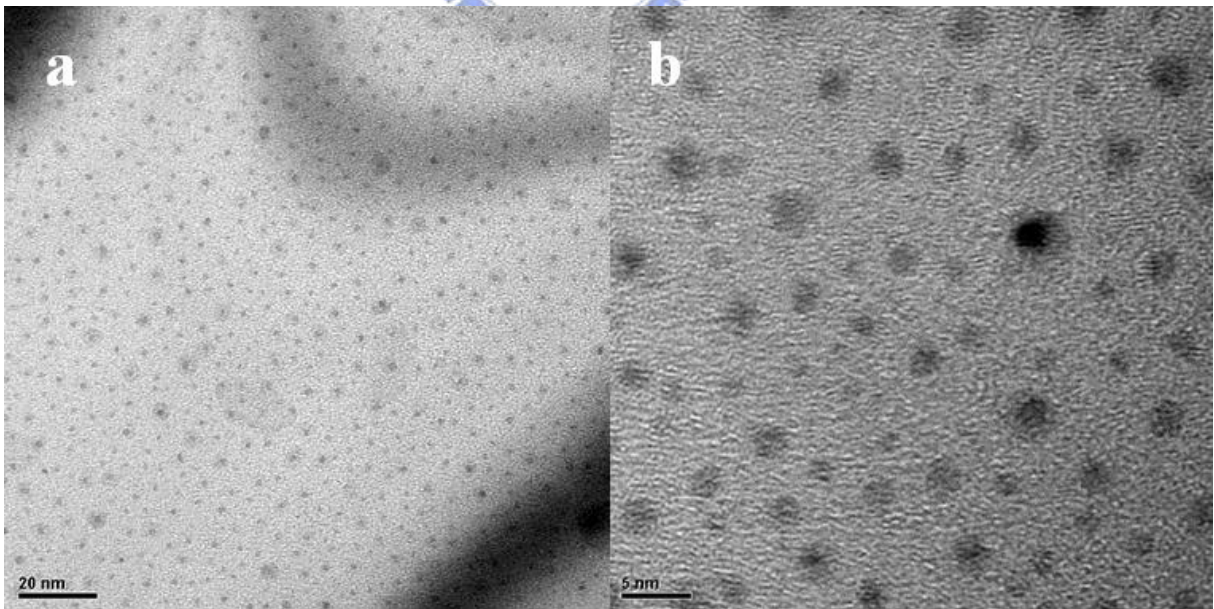
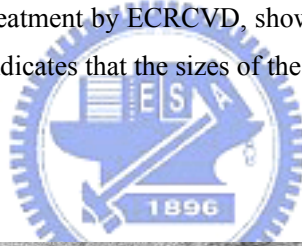


Fig.4-14 (a) The top-view HRTEM micrograph of CoCrPtO_x precursor nanoparticles (with AlON as buffer layer) following H-plasma treatment, showing a moderate distribution density, and (b) the highly magnified image in (a) indicates that the sizes of the nanoparticles range from 2.0 to 4.0 nm.

Table 4-2 Catalyst particle sizes after H-plasma pretreatment with various buffer layer, catalyst materials and application methods.

Specimen designation	Buffer layer / film thickness (nm)	Buffer layer/ film thickness (nm)	Average particle diameter from SEM figure (nm) ¹	Corresponding figure	Particle size from TEM
A1	Co /5	Native SiO ₂	35	4-5(a)	
B1	Co /5	ZnS-SiO ₂	35	4-5(b)	
C1	Co /5	Al ₂ O ₃	60	4-5(c)	
D1	Co /5	AlN	45	4-5(d)	
E1	Co / 5	AlON	60	4-5(e)	
A2	Co / 10	Native SiO ₂	50	4-6(a)	
B2	Co /10	ZnS-SiO ₂	120	4-6(b)	
C2	Co /10	Al ₂ O ₃	180	4-6(c)	
D2	Co /10	AlN	160	4-6(d)	
E2	Co /10	AlON	180	4-6(e)	
FB1	Fe/5	Si ₃ N ₄	—	4-7(a)	
FC1	Fe/5	TiN	—	4-7(b)	
FA1~FA3	Fe/5	Native SiO ₂	30	4-7(c)	
FD1~FD3	Fe/5	Al ₂ O ₃	23	4-7(d)	
FE1~FE3	Fe/5	AlN	15	4-7(e)	
FA4~FA6	Fe/10	Native SiO ₂	100	4-8(a)	
FD4~FD6	Fe/10	Al ₂ O ₃	30	4-8(b)	
FE4~FE6	Fe/10	AlN	25	4-8(c)	
G1	CoCrPtO _x , (10)	Native SiO ₂	50	4-9(a)	
G2	CoCrPtO _x , (5)	Native SiO ₂	22	4-9(b)	
G3	CoCrPtO _x , (3)	Native SiO ₂	8	4-9(c)	
G4	CoCrPtO _x , (2)	Native SiO ₂	5	4-9(d)	
G5	CoCrPtO _x , (1)	Native SiO ₂	3	4-9(e)	2.5~3.5 ^(*2)
G6	CoCrPtO _x , (1)	AlON	3	4-9(f)	1~3.5 ^(*3)
H1	Co, (5)	Native SiO ₂	80	4-9(a)	
H2	CoCrO _x , (5)	Native SiO ₂	30	4-9(b)	

H3	CoCrPtO _x (5)	Native SiO ₂	20	4-9(c)	
I1~I4	CoCrPtO _x (2)	Native SiO ₂	4	4-12(a)	
I5	CoCrPtO _x (1)	Native SiO ₂	3	4-12(b)	2~6 ^(*4)
I6	CoCrPtO _x (1)	AlON	— ^{*1}	4-12(c)	2~4 ^(*5)

Note : *1 : cannot detectable; *2 : refer to Fig. 4-10; *3: refer to Fig. 4-11, *4: refer to Fig. 4-13 and *5: refer to Fig. 4-14.



4.3. Structures of the Co-assisted carbon nanostructures by MPCVD

4.3.1 Effects of buffer layer materials and catalyst thickness

Figures 4-15(a) to (e) illustrate the FESEM morphologies of the nanostructures of Co catalyst layer with 5 nm thickness, under the same process conditions but different buffer layer materials, respectively. The wafers in Figs. 4-15(a), (b) and (d) for Specimens A1, B1 and D1 with no buffer application, ZnS-SiO₂ and AlN materials as buffer layer materials, respectively, have not CNTs. By contrast, the networks of small sized CNTs can be found in Figs. 4-15(c) and 1(e) for Specimens C1 and E1 with Al₂O₃ and AlON as buffer layers, respectively, where the networks are linked between the neighboring catalyst nanoparticles.

Figure 4-16 shows the Raman spectra of the nanostructures with five different buffer layer materials (Specimens A1 to E1). The Raman spectra for Specimens A1, B1 and D1 contained no obvious G-band and D-band peaks with native SiO₂, ZnS-SiO₂ and AlN buffer layer materials. Conversely, a strong peak of radial breath mode (RBM) and a high I_G/I_D ratio were obtained for Specimens C1 and E1 with Al₂O₃ and AlON as buffer layers, respectively, showing the existence of highly graphitized MWNTs and SWNTs. This finding is based on the proposition that the peak intensity of RBM is linked to the quantity of SWNTs in the nanostructures^[Rao-1997-187]. Moreover, the RBM peak is stronger in nanostructures with a buffer layer of AlON than those with Al₂O₃, indicating that AlON promotes SWNT formation more effectively than Al₂O₃. Restated, Al₂O₃ and AlON materials can be the buffer layer candidate materials to encourage the formation of SWNT networks by MPCVD. The other materials (native SiO₂, AlN, ZnS-SiO₂) are poor in these applications. Detailed conditions of nanostructures on Si wafer with various buffer layer materials are summarized in Table 4-3.

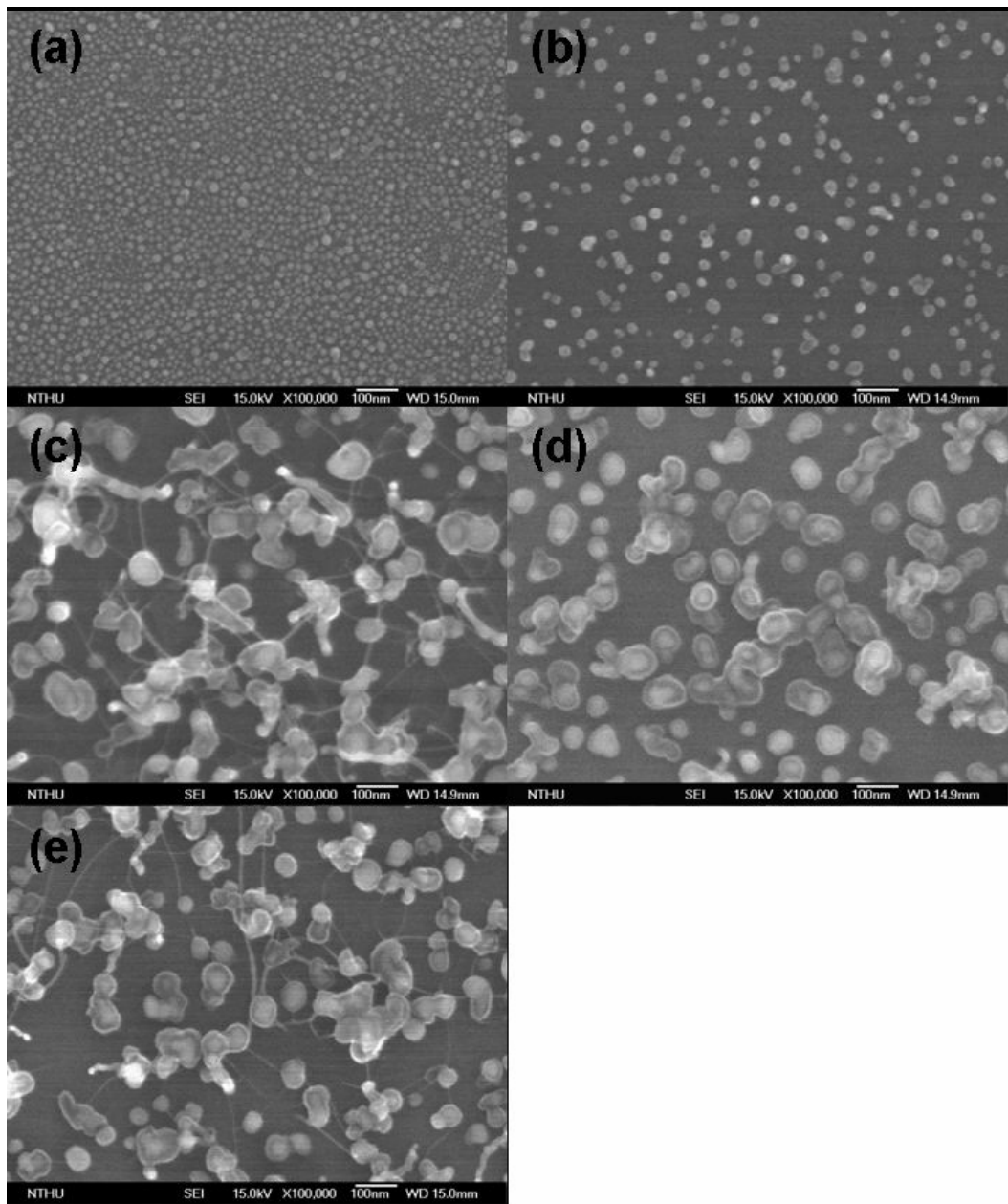


Fig.4-15 SEM micrographs of the Co-assisted carbon nanostructures (Co: 5 nm) on silicon wafers with various buffer materials : (a) native SiO_2 , (b) ZnS-SiO_2 , (c) Al_2O_3 , (d) AlN and (e) AlON , respectively (Specimens A1 to E1).

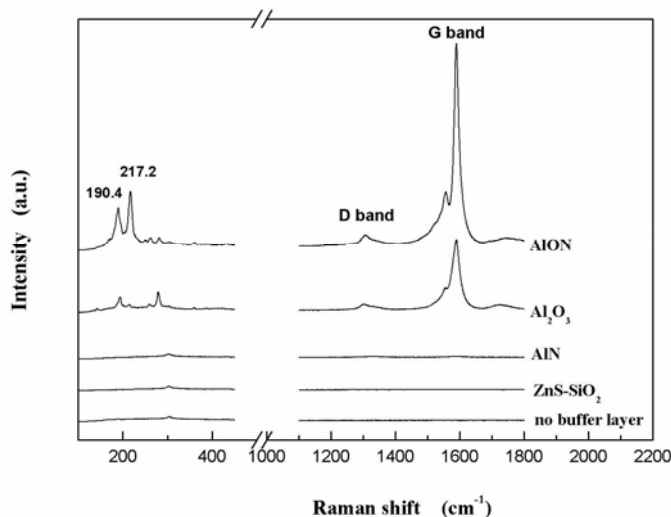


Fig. 4-16 Raman spectra of the Co-assisted carbon nanostructures (Co: 5 nm) on silicon wafers with various buffer materials.

To explore the effect of catalyst thickness, figures 4-17(a) to (e) illustrate the FESEM morphologies of the nanostructures of Co catalyst film, whose thickness are varying from 5 nm to 10 nm, under the same process conditions but different buffer layer materials, respectively. The wafers in Figs. 4-17(a), (b) and (d) for Specimens A2, B2 and D2 with native SiO₂, ZnS-SiO₂ and AlN materials as buffer layer materials, respectively, have not CNTs. This result is same as that with 5 nm thickness and the difference is that very few networks of small sized CNTs can be found in Figs. 4-17(c) and 1(e) for Specimens C2 and E2 with Al₂O₃ and AION as buffer layers, respectively, indicating that thick Co thickness is not favor condition for SWNTs fabrication.

Figure 4-18 shows the Raman spectra of the nanostructures with different Co thickness under Al₂O₃ and AION buffer layer materials (Specimens C1, C2, E1 and E2). The Raman spectra for all specimens show RBM peaks but stronger peak of RBM and higher I_G/I_D ratio are obtained for Specimens of C1 and E1, showing the thin thickness (5 nm) is more favorable to encourage the formation of SWNT.

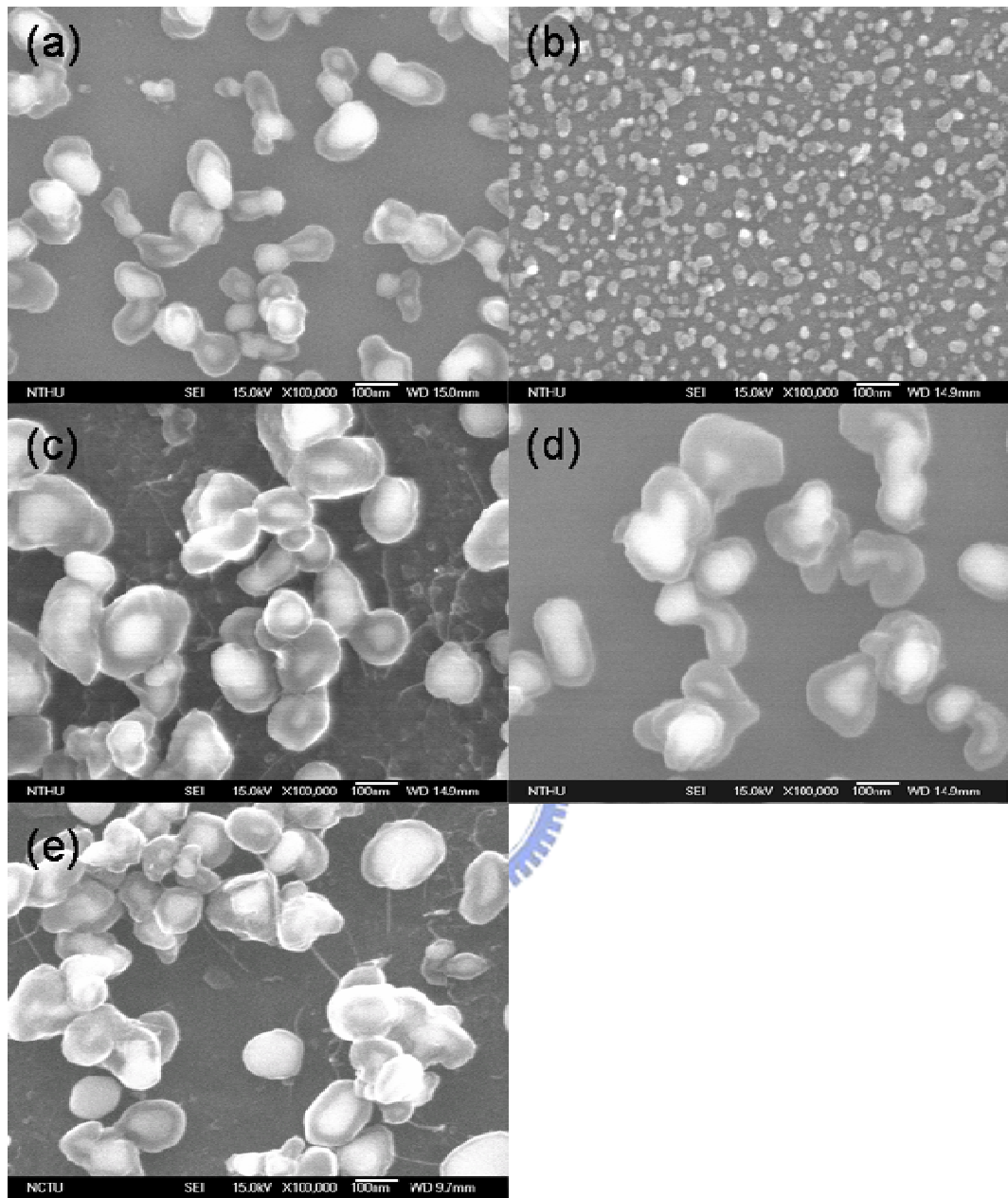


Fig.4-17 SEM micrographs of the Co-assisted carbon nanostructures (Co : 10 nm) on silicon wafers with various buffer materials: (a) native SiO₂, (b) ZnS-SiO₂, (c) Al₂O₃, (d) AlN, and (e) AlON, respectively (Specimens A2 to E2).

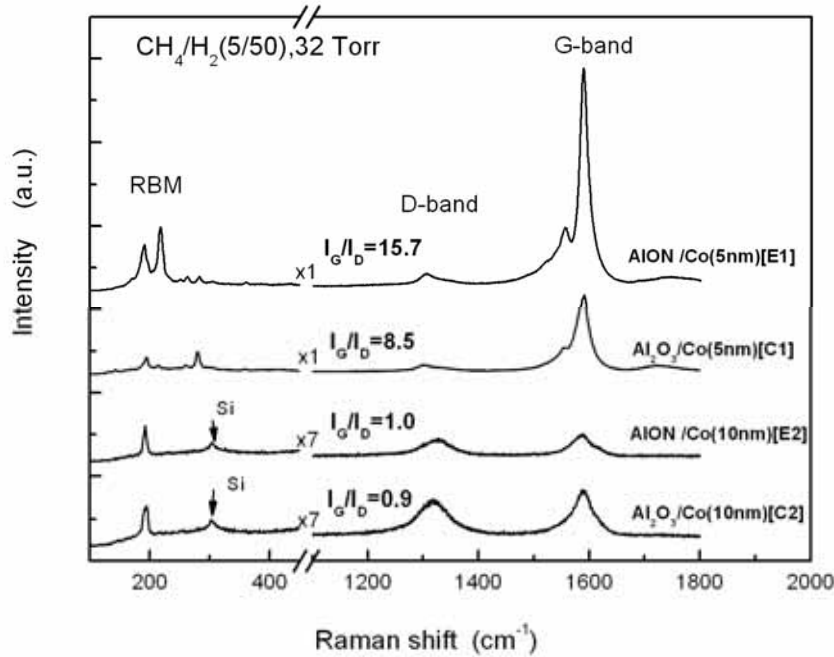


Fig. 4-18 Raman spectra of the Co-assisted carbon nanostructures (Co : 5 nm and 10 nm) on silicon wafers with Al₂O₃ and AlON materials as buffer layers.

4.3.2 Effects of pressure

Previous results are based on working pressure of 32 Torr. Figures 4-19(a) to (b) illustrate the FESEM morphologies of the nanostructures of Co catalyst layer with 5 nm thickness, under working pressure are varying from 32 Torr to 23 Torr and 16 Torr, respectively. The wafers in Fig. 4-19 display that dense CNT networks are synthesized at 23 Torr but no CNTs are formed at 16 Torr. Figure 4-20 shows the Raman spectrum of CNT networks synthesized at 23 Torr. There are strong peak of radial breath mode (RBM) and high I_G/I_D ratio can be found in Raman spectrum, indicating existence of highly graphitized CNTs and more SWNTs. These results indicate that the networks of CNT are indeed synthesized successfully in this experiment. Notably, the deposition temperature in these cases is around 640 °C, which is much less than that found in the previous works^{[de los Arcos -2004-187] [Ting-2002-324] [Delzeit-2001-368][Cassell-2003-817]}. The diameter of SWNTs can be estimated by the theoretical calculating from the positions of RBM peaks^[Jorio-2002-155412] and predict their diameters are varied from 0.8 to 1.3 nm.

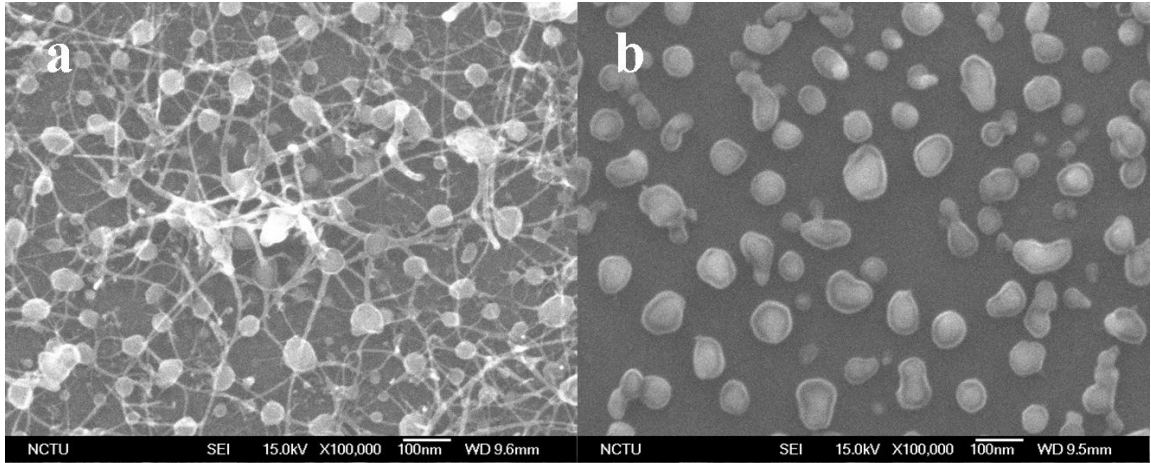


Fig.4-19 SEM micrographs of the Co-assisted carbon nanostructures (Co: 5 nm) with AlON as buffer layer on silicon wafers under different working pressures: (a) 23 Torr and (b) 16 Torr (Specimens E3 and E4).

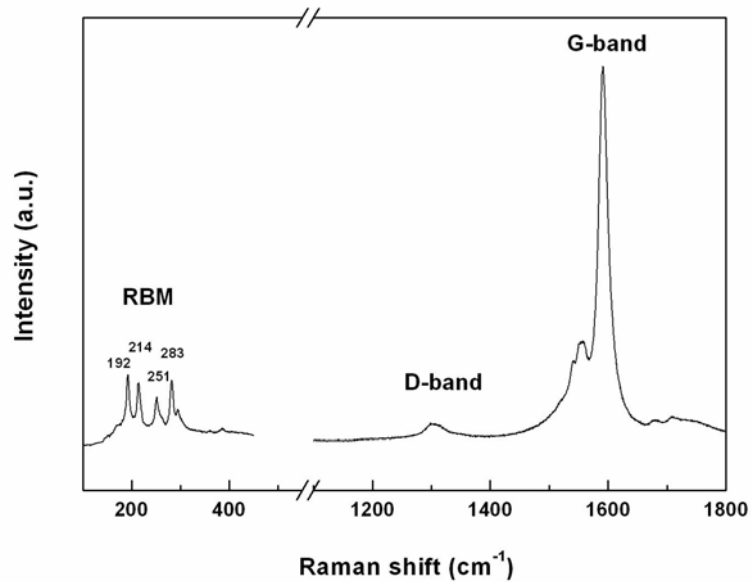


Fig. 4-20 Raman spectra of the Co-assisted carbon nanostructures (Co: 5 nm) with AlON as buffer layer on silicon wafers under 23 Torr of working pressure (Specimens E3).

4.3.3 TEM microstructures

The HRTEM images of networks of CNT are shown in Figs. 4-21(a) and (b). It consists of SWNTs with diameter of 1.1 nm and networks are formed by bundles of SWNTs as shown in Fig. 4-21(a). The diameters of SWNTs observed in HRTEM image are in agreement with those of calculating in Raman spectrum. It is interesting to observe some networks are connected by individual SWNTs as depicted in Fig. 4-21 (b). Besides, MWNTs with diameter of ~15 nm are found to be synthesized accompany with SWNTs. Hence, it is concluded that as-produced CNT networks consist of SWNTs and MWNTs.

These FESEM and HRTEM results show the SWNTs ropes grown from catalyst particles radially, where their morphologies are similar as those of observed by Saito et al. ^[Saito-1994-526] ^[Gavillet-2001-275504]. It suggests that formation of buffer-layer-assisted SWNT networks may follow the proposed root-growth mechanism ^[Gavillet-2001-275504] and will be discussed in paragraph of formation mechanism. The most interesting to note is that the suggested Ni catalyst size to grow SWNTs ropes by arc-discharge method following root-growth is ~15 nm in previous research ^[Saito-1994-526] ^[Zhou-1994-1593]. However, these SWNTs ropes with network structures can be found to grow from large-sized Co catalyst particles (~50 nm, ref to Fig. 4-21). It indicates that the critical catalyst size to form SWNTs ropes strongly depends on the fabrication methods and catalyst materials. Several metal materials, such as Fe, Ni, and Gd, have been studied as catalysts for fabricating SWNTs successfully and present similar morphologies in previous study. In this work, we obtain a microstructure of SWNT networks with Co metal as the catalyst material under the assistance of buffer layer and find the catalyst size for SWNTs growth is quite large.

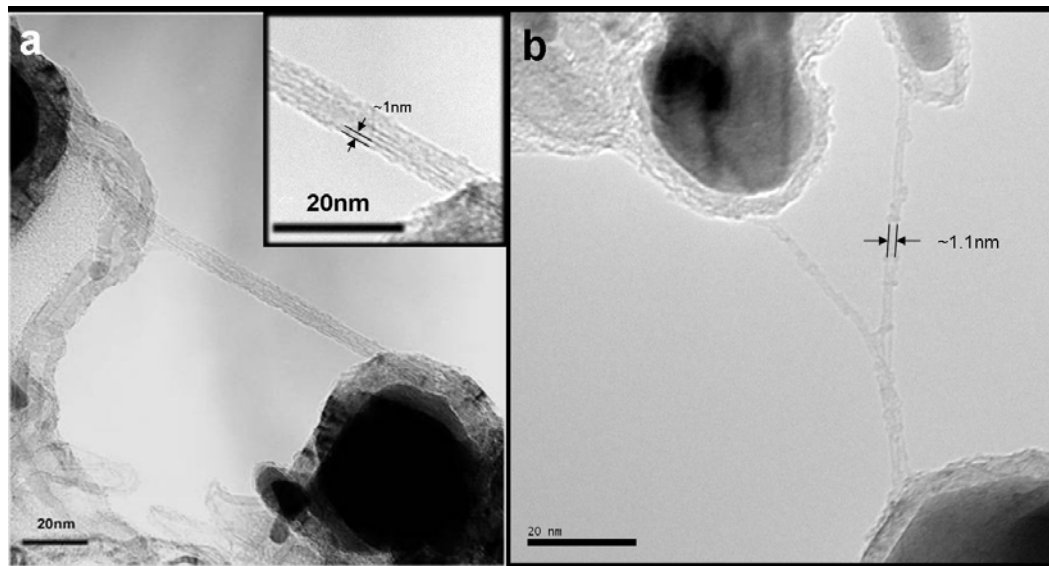
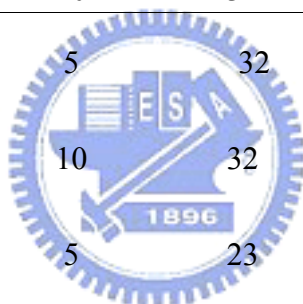


Fig. 4-21 HRTEM images of SWNTs networks grown on silicon wafers with AlON buffer layer: (a) the networks of bundles of SWNTs, and (b) networks are formed by individual SWNT.

Co-catalyst and buffer-layer assisted SWNT networks on Si wafers were successfully fabricated in a MPCVD system with CH₄ and H₂ as source gases. The lowest temperature in the present conditions to form SWNTs is ~ 620°C (23 Torr). Experimental results demonstrate that the materials which most effectively promote SWNTs formation are AlON followed by Al₂O₃. Our results further demonstrate that AlN buffer material is good only for MWNT fabrication, while native SiO₂ and ZnS-SiO₂ are not candidate buffer materials for CNTs growth. Moreover, the results also indicate that the favorable conditions for synthesizing CNTs networks are a working pressure of 23 Torr and thin catalyst thickness (5 nm) with AlON as the buffer layer material. Detailed conditions of nanostructures on Si wafer with various buffer layer materials are summarized in Table 4-3.

Table 4-3 Summaries of the Co-assisted carbon nanostructures on Si wafer with various buffer layer materials.

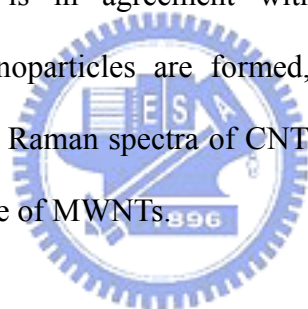
Specimen designation	Buffer layer material and thickness (nm)	Co catalyst layer thickness(nm)	Pressure (Torr)	Nanostructure morphology	Corresponding figure
A1	Native SiO ₂	5	32	Particle-like	4-15(a)
A2	Native SiO ₂	10	32	Particle-like	4-17(a)
B1	ZnS-SiO ₂ (10)	5	32	Particle-like	4-15(b)
B2	ZnS-SiO ₂ (10)	10	32	Particle-like	4-17(b)
C1	Al ₂ O ₃ (10)	5	32	Network-like MWNTs and SWNTs,	4-15(c)
C2	Al ₂ O ₃ (10)	10	32	Network-like MWNTs and SWNTs,	4-17(c)
D1	AlN (10)	5	32	Particle-like	4-15(d)
D2	AlN (10)	10	32	Particle-like	4-17(d)
E1	AlON (10)	5	32	Network-like MWNTs and SWNTs	4-15(e)
E2	AlON (10)	10	32	Network-like MWNTs and SWNTs	4-17(e)
E3	AlON (10)	5	23	Dense network-like MWNTs and SWNTs	4-19(a)
E4	AlON (10)	5	16	Particle-like	4-19(b)



4.4 Structures and properties of the Fe-assisted carbon nanostructures by MPCVD

4.4.1 Effects of buffer layer materials, CH₄/H₂ ratio and catalyst thickness

Figures 4-22(a) to (e) illustrate the FESEM morphologies of the nanostructures of Fe catalyst layer with 5 nm thickness, under a same CH₄/H₂ ratio (5/50 sccm/sccm) but different buffer layer materials, respectively. The wafers in Figs. 4-22(a) for Specimens with native SiO₂ have few CNTs. By contrast, the CNT films can be found in Figs. 4-22(d) and 22(e) for Specimens FD1 and FE1 with Al₂O₃ and AlN as buffer layers, respectively. Figures 4-22(b) and (c) present the FESEM morphologies of the nanostructures of Specimens with Si₃N₄ and TiN buffer layer materials, illustrating that not CNTs are formed and few CNTs are synthesized, respectively. It is in agreement with the results in Figs 4-7 that no well-distributed pretreated nanoparticles are formed, which are not favorable for CNTs growth. Figure 4-23 shows the Raman spectra of CNTs that there are not RBM peaks can be found, indicating only existence of MWNTs.



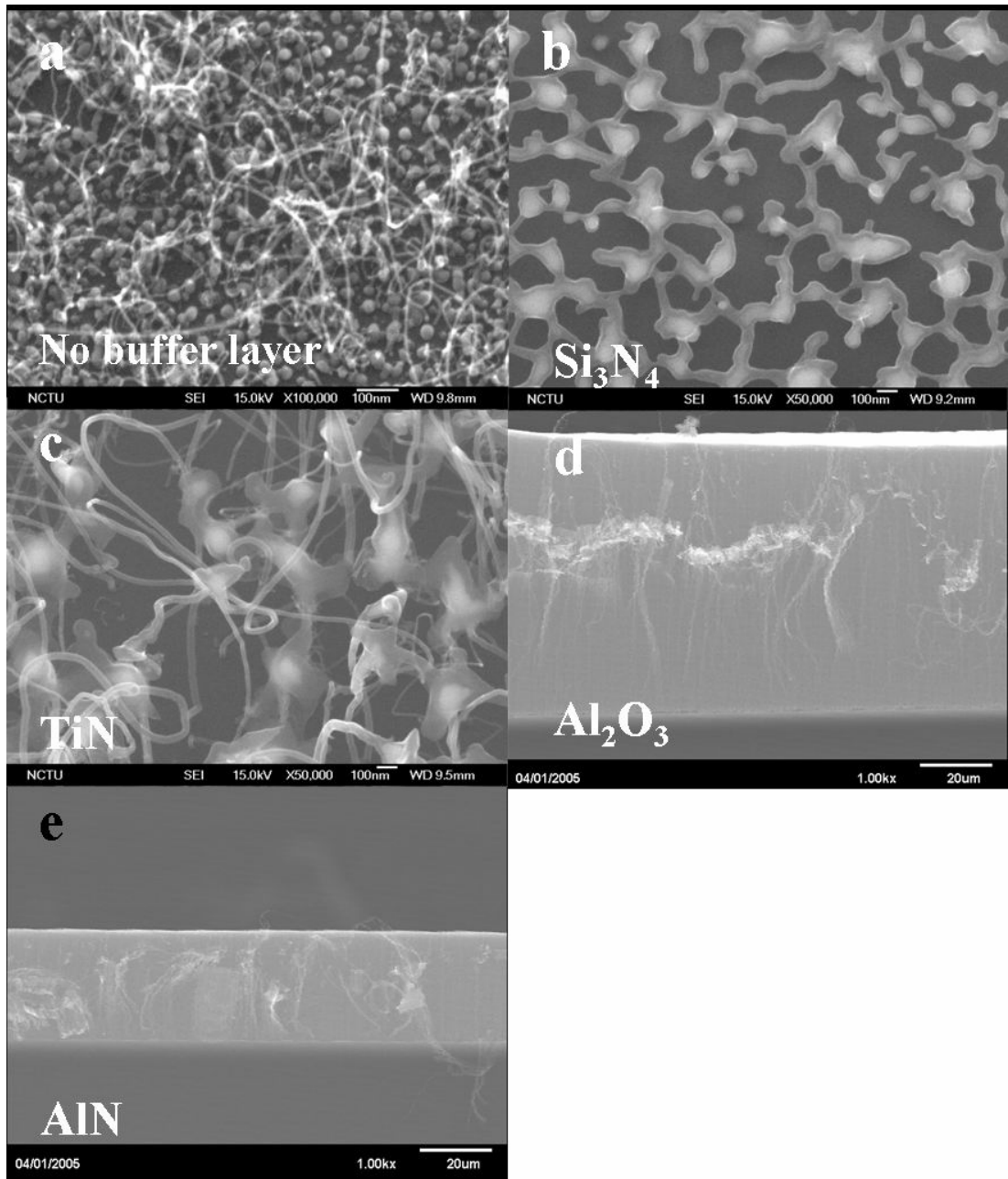


Fig. 4-22 SEM micrographs of the Fe-assisted carbon nanostructures (Fe : 5 nm) on silicon wafers with various buffer materials: (a) native SiO_2 , (b) Si_3N_4 , (c) TiN, (d) Al_2O_3 , and (e) AlN, respectively (Specimens FA1, FB1, FC1, FD1, and FE1).

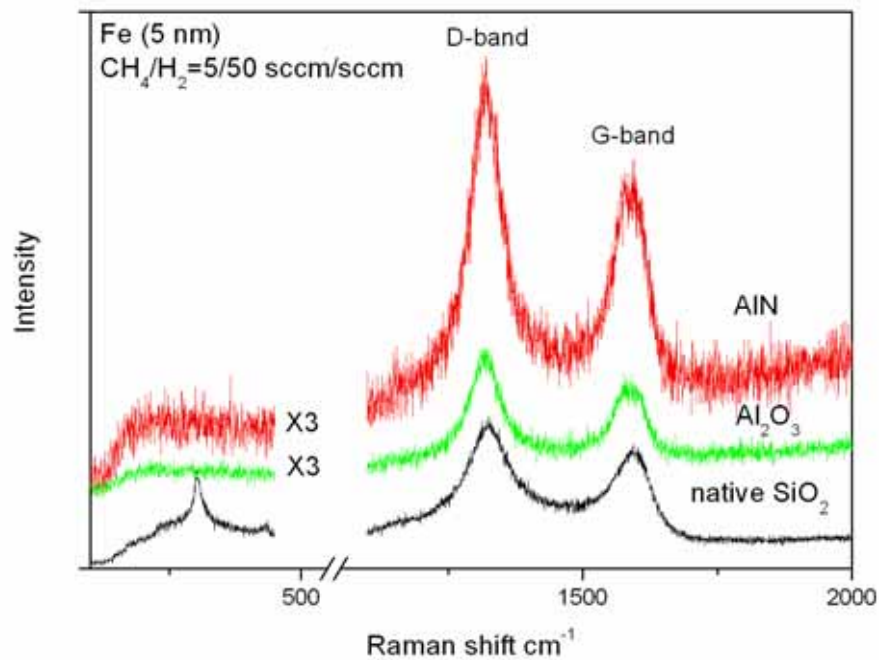


Fig. 4-23 Raman spectra of the Fe-assisted carbon nanostructures (Fe: 5 nm) on silicon wafers with native SiO₂, Al₂O₃ and AlN materials as buffer layers (Specimens FA1, FD1, and FE1).

CH₄/H₂ ratio is further reduced from 5/50 to 1.5/50 and 1.5/100 (sccm/sccm), respectively, to study its effect on the nanostructures of Fe catalyst layer with 5 nm thickness under native SiO₂, Al₂O₃ and AlN buffer layer materials. Figures 4-24(a) to (f) present the FESEM morphologies of the nanostructures of Specimens (FA2, FA3, FD2, FD3, FE2 and FE3), illustrating that spaghetti-like CNTs are still synthesized in the specimens with native SiO₂ and the thickness of as-grown CNT films are decreased as CH₄/H₂ ratio reducing in the specimens with Al₂O₃ and AlN as buffer layers. Raman spectra of as-grown CNTs in Figs. 4-25 and 4-26 demonstrate that RBM peaks and higher I_G/I_D ratio can be found in the specimens with Al₂O₃ and AlN as buffer layers under a CH₄/H₂ ratio of 1.5/100 (sccm/sccm), indicating that the existence of SWNTs. By contrast, no detectable SWNTs signal is found in the specimen with native SiO₂ as buffer layer.

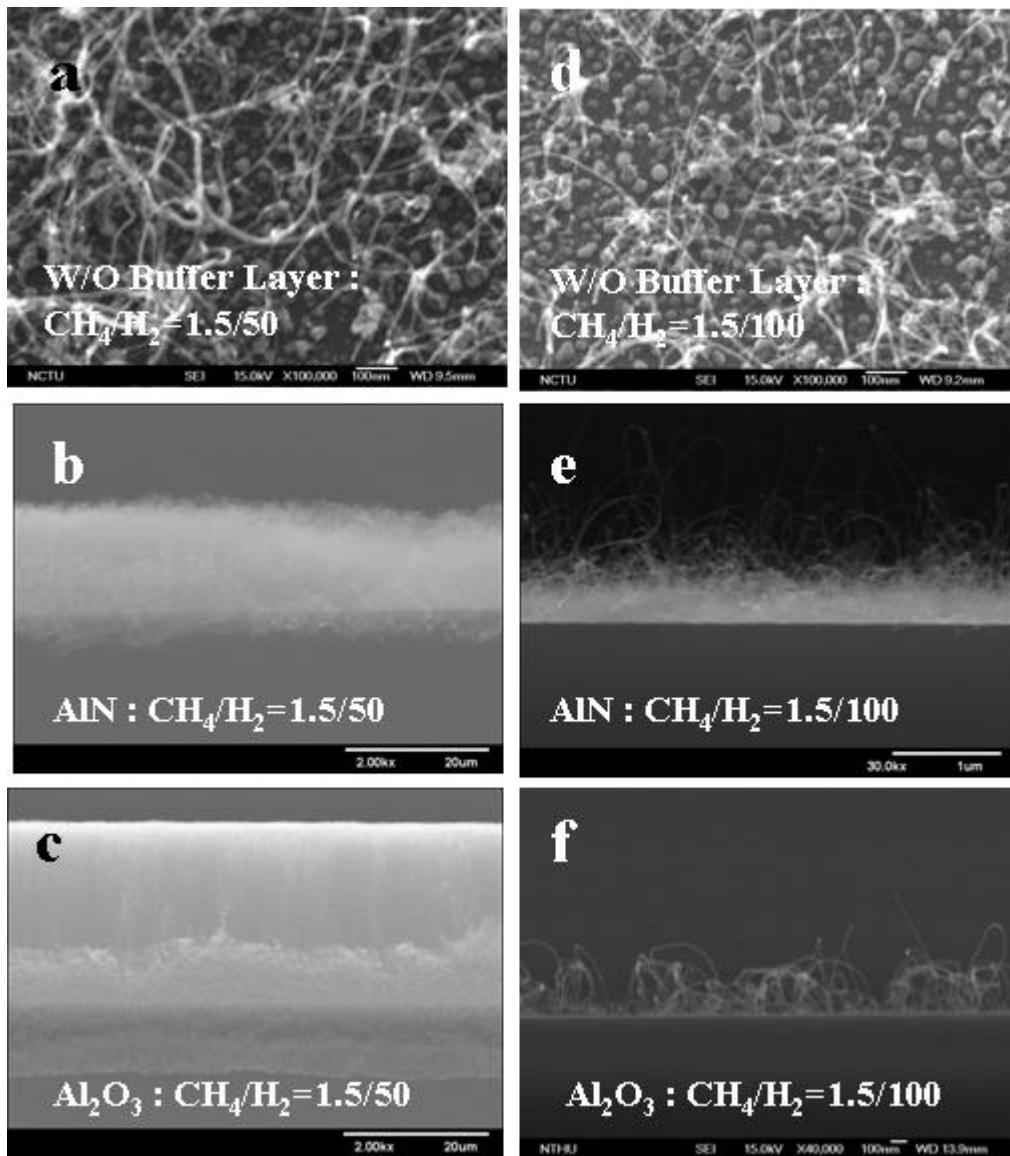


Fig. 4-24 SEM micrographs of the Fe-assisted carbon nanostructures (Fe: 5 nm) on silicon wafers with various buffer materials and under a CH₄/H₂ ratio of 5/50 (sccm/sccm): (a) native SiO₂, (b) AlN, (c) Al₂O₃, (d) native SiO₂, (e) AlN, and (f) Al₂O₃, respectively (Specimens FA2, FE2, FD2, FA3, FE3 and FD3).

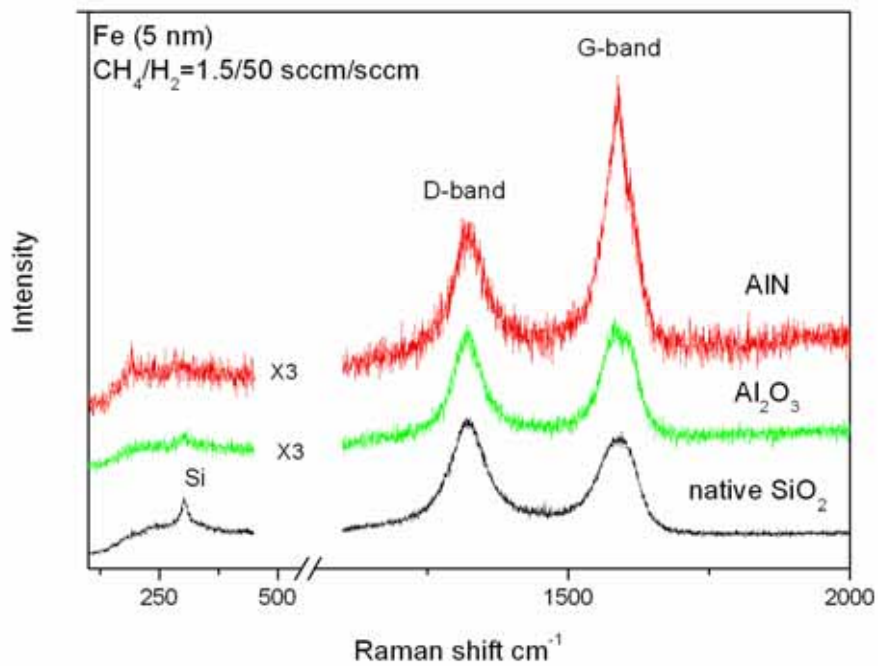


Fig. 4-25 Raman spectra of the Fe-assisted carbon nanostructures (Fe: 5 nm) on silicon wafers with native SiO₂, Al₂O₃ and AlN materials as buffer layers under a CH₄/H₂ ratio of 1.5/50 (sccm/sccm) (Specimens FA2, FD2, and FE2).

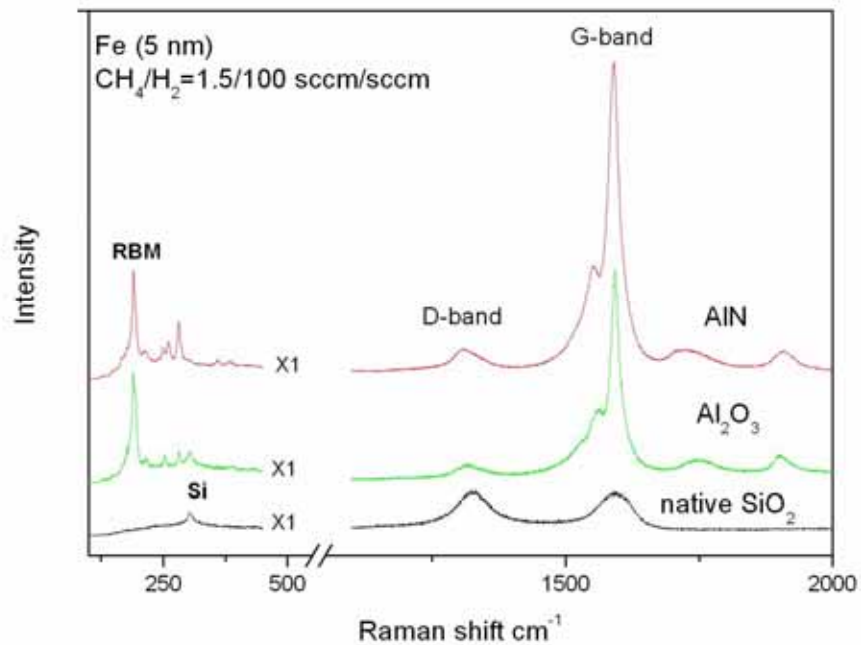


Fig. 4-26 Raman spectra of the Fe-assisted carbon nanostructures (Fe: 5 nm) on silicon wafers with native SiO₂, Al₂O₃ and AlN materials as buffer layers under a CH₄/H₂ ratio of 1.5/100 (sccm/sccm) (Specimens FA3, FD3, and FE3).

In the case of Fe layer with 10 nm thickness, their typical FESEM micrographs are similar with that of 5 nm thickness. The difference is that Raman spectra shown in Fig. 4-27 demonstrate that SWNTs are only found in the specimen with AlN as buffer layer at a CH₄/H₂ ratio of 1.5/100 (sccm/sccm), suggesting that AlN has a stronger effect than Al₂O₃ to enhance SWNTs formation. Detailed experimental result is summarized in Table 4-4. It is concluded that Al₂O₃ and AlN materials can be the buffer layer candidate materials under a low CH₄/H₂ ratio (1.5/100 sccm/sccm) and a thin Fe catalyst film (5 nm) to encourage the formation of SWNTs by MPCVD.

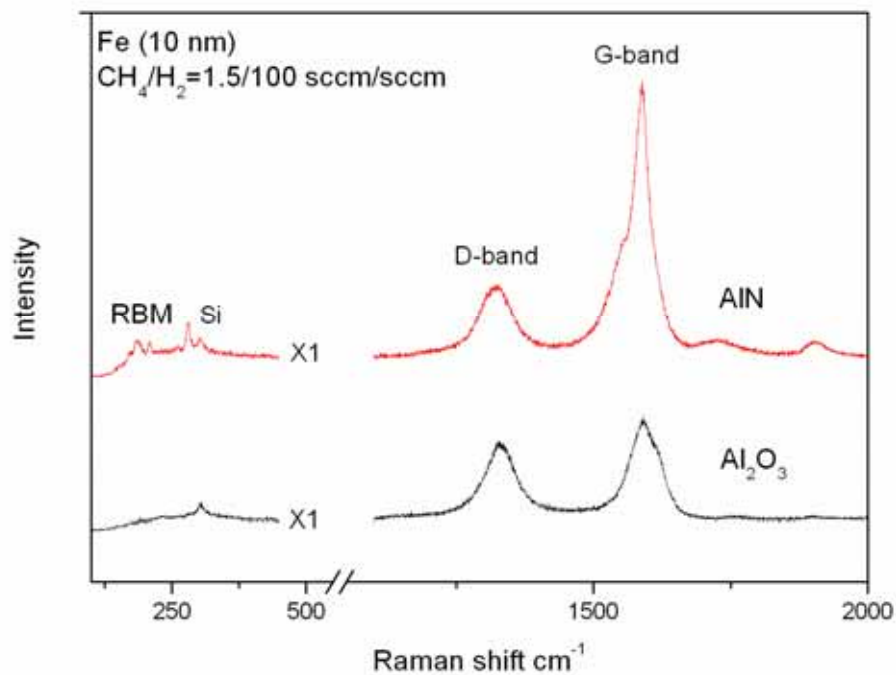


Fig. 4-27 Raman spectra of the Fe-assisted carbon nanostructures (Fe: 10 nm) on silicon wafers with native Al₂O₃ and AlN materials as buffer layers at a CH₄/H₂ ratio of 1.5/100 (sccm/sccm) (Specimens FD6, and FE6).

Table 4-4 Summaries of the Fe-assisted carbon nanostructures on Si wafer with various buffer layer materials.

Specimen designations	Buffer layer material	Catalyst Thickness (nm)	CH ₄ /H ₂ ratio (sccm/sccm)	I _G /I _D ratio	Morphology	CNTs orientation	Corresponding figure
FB1	Si ₃ N ₄	5	5/50	-	particle-like	-	4-22(b)
FC1	TiN	5	5/50	0.7	trace MWNTs	spaghetti	4-22(c)
FA1	native SiO ₂	5	5/50	0.9	trace MWNTs	spaghetti	4-22(a)
FA2	native SiO ₂	5	1.5/50	0.9	trace MWNTs	spaghetti	4-24(a)
FA3	native SiO ₂	5	1.5/100	1.0	trace MWNTs	spaghetti	4-24(d)
FA4	native SiO ₂	10	5/50	0.9	particle-like	spaghetti	-
FA5	native SiO ₂	10	1.5/50	0.9	particle-like	spaghetti	-
FA6	native SiO ₂	10	1.5/100	1.0	particle-like	spaghetti	-
FD1	Al ₂ O ₃	5	5/50	0.7	MWNTs	aligned	4-22(d)
FD2	Al ₂ O ₃	5	1.5/50	1.1	MWNTs	aligned	4-24(c)
FD3	Al ₂ O ₃	5	1.5/100	1.0	MWNTs and SWNTs	spaghetti	4-24(f)
FD4	Al ₂ O ₃	10	5/50	0.8	MWNTs	aligned	-
FD5	Al ₂ O ₃	10	1.5/50	0.9	MWNTs	aligned	-
FD6	Al ₂ O ₃	10	1.5/100	1.3	MWNTs	spaghetti	-
FE1	AlN	5	5/50	0.7	MWNTs	aligned	4-22(e)
FE2	AlN	5	1.5/50	1.7	MWNTs	aligned	4-24(b)
FE3	AlN	5	1.5/100	10.5	MWNTs and SWNTs	spaghetti	4-24(e)
FE4	AlN	10	5/50	0.7	MWNTs	aligned	-
FE5	AlN	10	1.5/50	1.7	MWNTs	aligned	-
FE6	AlN	10	1.5/100	2.9	MWNTs and SWNTs	spaghetti	-

4.4.2 Effect of Al₂O₃ and AlN thickness

To compare carefully the effects of Al₂O₃ and AlN buffer layer, their thickness was varied from 5 to 15 nm under a reduced CH₄/H₂ ratio of 1.5/200 (sccm/sccm) because low ratio is concluded to be favorable for SWNTs growth in last paragraph. Typical FESEM micrographs in Figs 4-28 (a) to (f) display the CNTs with random orientation are grown and no obvious difference are observed between specimens using Al₂O₃ and AlN buffer layer,

suggesting different buffer layer thickness will not affect the morphologies of as-grown CNTs. Figures 4-29 and 4-30 show the Raman spectra of as-grown CNT films with Al_2O_3 and AlN as buffer layer materials and with different thickness, respectively, demonstrating that no obvious I_G/I_D ratio difference is observed as buffer layer thickness change and RBM peaks are obtained in all specimens, in which specimens using AlN as buffer layer show higher RBM peaks and I_G/I_D ratio than those using Al_2O_3 . This result indicates that AlN have stronger effect than Al_2O_3 to encourage the formation of SWNTs. We will further discuss the reason in next paragraph. Furthermore, FESEM results demonstrated that many particles were not reacted, indicating only some of pretreated particles involved CNTs growth. Since small particles are easily poisoned to lose activity, low carbon concentration is favorable for SWNTs growth, which explains the SWNTs are more favorable to be synthesized under a lower CH_4/H_2 ratio (1.5/200 sccm/sccm). It is concluded that thickness (5~15 nm) of Al-based buffer layer will not affect the nano-structures of as-grown CNTs but buffer material will dominate the growth of SWNTs in which AlN shows stronger effect than Al_2O_3 . Detailed experimental results are summarized in Table 4-5.

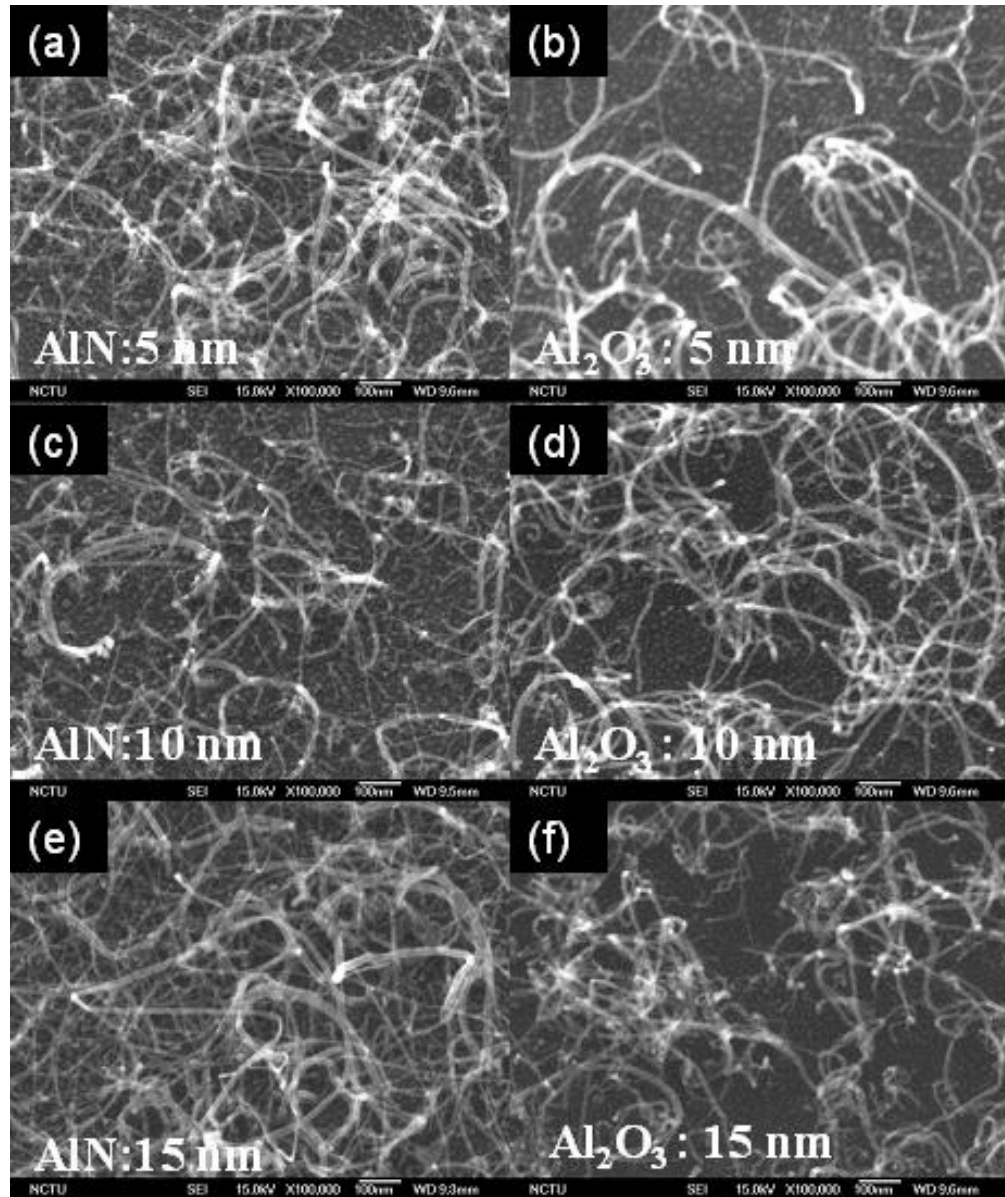


Fig. 4-28 FESEM micrographs of the Fe-assisted carbon nanostructures (Fe: 5 nm) on silicon wafers with various thicknesses of buffer layers: (a) AlN (5 nm), (b) Al₂O₃ (5 nm), (c) AlN (10 nm), (d) Al₂O₃ (10 nm), (e) AlN (15 nm), (f) Al₂O₃ (15 nm), respectively (Specimens FE7, FD7, FE8, FD8, FE9 and FD9).

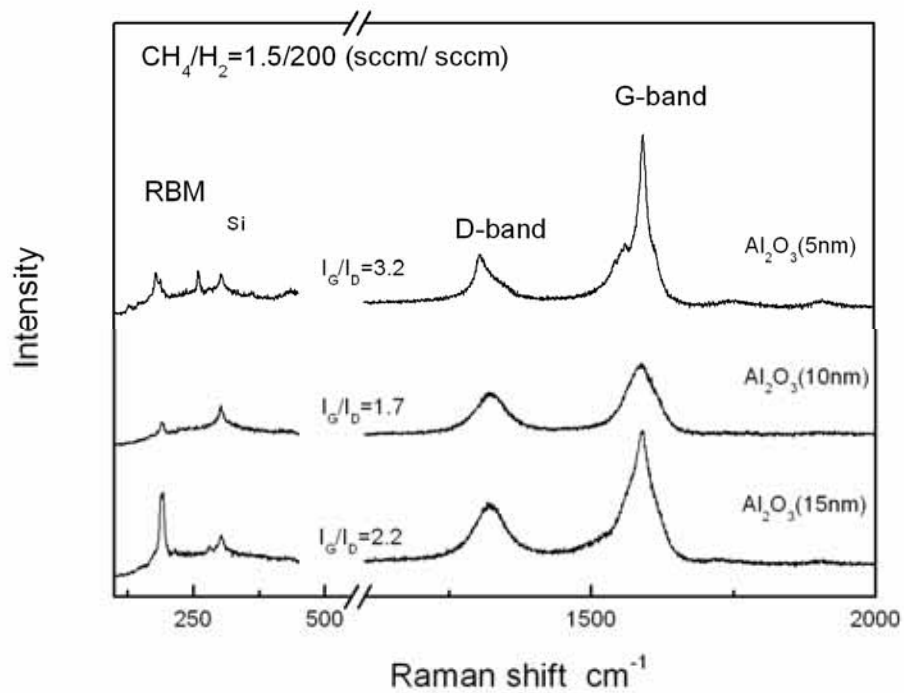


Fig. 4-29 Raman spectra of the Fe-assisted carbon nanostructures (Fe: 5 nm) on silicon wafers with different thicknesses of Al₂O₃ buffer layers at a CH₄/H₂ ratio of 1.5/200 (sccm/sccm) (Specimens FD7, FD8, and FD9).

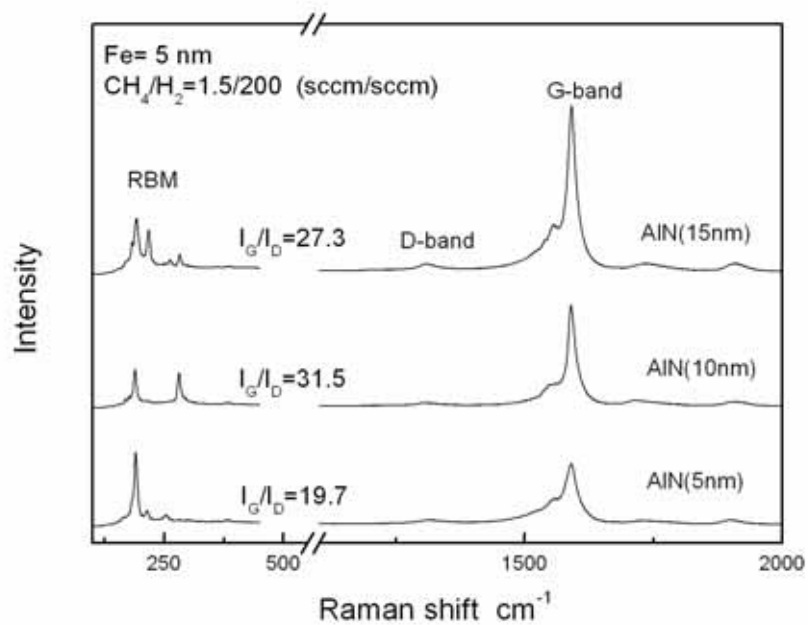
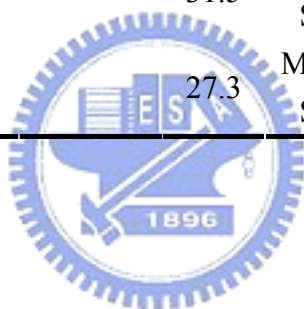


Fig. 4-30 Raman spectra of the Fe-assisted carbon nanostructures (Fe: 5 nm) on silicon wafers with different thicknesses of AlN buffer layers at a CH₄/H₂ ratio of 1.5/200 (sccm/sccm) (Specimens FE7, FE8, and FE9).

Table 4-5 Summaries of the Fe-assisted carbon nanostructures on Si wafer with various thicknesses of Al₂O₃ and AlN buffer layers.

Specimen designation	Buffer layer materials and its thickness (nm)	Catalyst Thickness (nm)	CH ₄ /H ₂ ratio (sccm/sccm)	I _G /I _D ratio	CNTs type	CNTs Morphology	Corresponding figure
FD7	Al ₂ O ₃ (5)	5	1.5/200	3.2	MWNTs + few SWNTs	Spaghetti-like	4-28(b)
FD8	Al ₂ O ₃ (10)			1.7	MWNTs + few SWNTs	Spaghetti-like	4-28(d)
FD9	Al ₂ O ₃ (15)			2.2	MWNTs + few SWNTs	Spaghetti-like	4-28(f)
FE7	AlN (5)			19.7	MWNTs + SWNTs	Spaghetti-like	4-28(a)
FE8	AlN (10)			31.5	MWNTs + SWNTs	Spaghetti-like	4-28(c)
FE9	AlN (15)			27.3	MWNTs + SWNTs	Spaghetti-like	4-28(e)



4.4.3 TEM microstructures

The typical HRTEM micrograph of as-grown CNTs (Specimens FE3) is shown in Fig. 4-31, comprising DWNTs (~ 3.5 nm in diameter), individual SWNT (~2 nm in diameter) and bundles of SWNTs (0.9~ 2.1 nm in diameter). Few MWNTs with diameter of ~8 nm were also found in HRTEM observation, indicating that as-grown CNTs are mainly consisted of SWNTs, DWNTs and few MWNTs. These results are in agreement with previous assumptions from Raman spectra.

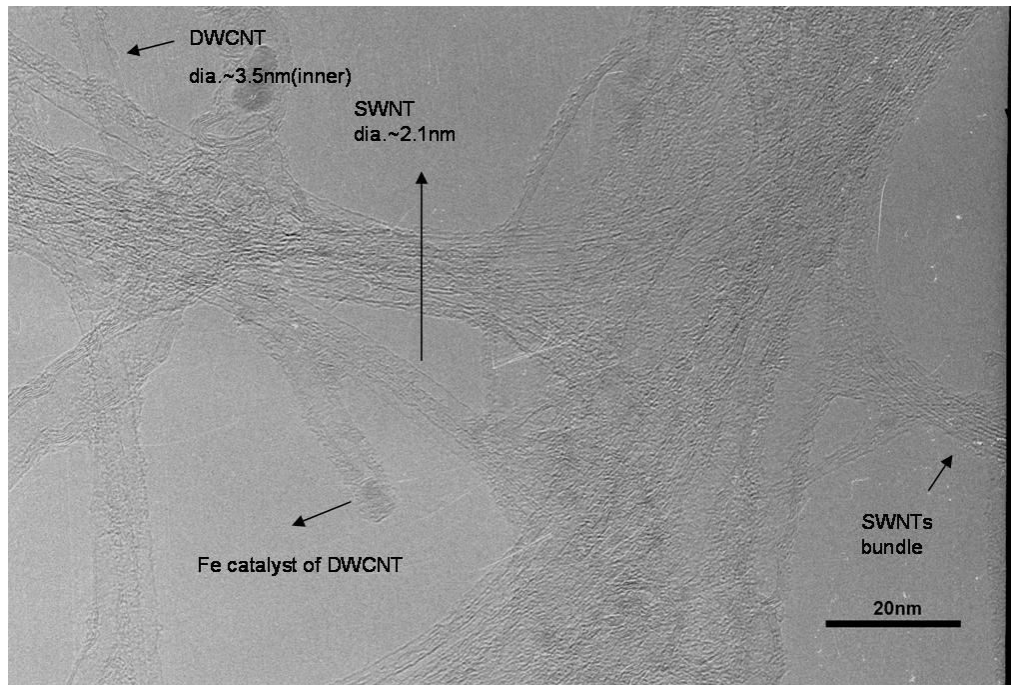


Fig. 4-31 Typical HRTEM micrograph of the Fe-assisted CNTs (Specimen FE3), in which CNTs consist of SWNTs, DWNTs and MWNTs.

4.4.4 Field emission properties

Figure 4-32 displays the field emission current densities as a function of electric field for the as-grown Fe-assisted CNT with native SiO₂, Al₂O₃, and AlN as buffer layers (Fe, 5 nm; CH₄/H₂, 50/5 sccm/sccm), showing similar characteristics in which the turn-on voltages (0.01 mA/cm²) are around 3.6, 3.4, and 3.5 V/μm and the highest current densities are ~33, ~34, and ~34 mA/cm² (at 5.6 V/μm) for specimens with native SiO₂, Al₂O₃, and AlN as buffer

layers, respectively. Since the tube densities and structures of CNTs with Al_2O_3 and AlN buffer layers are quite similar, it is reasonable that there are no differences on field emission properties. However, almost same turn-on voltage is obtained from random orientation Fe-assisted CNTs with native SiO_2 buffer layer. It is proposed that screening effect from dense and well-aligned CNTs increase the turn-on voltage and thus showed similar value as random-like as-grown CNTs.

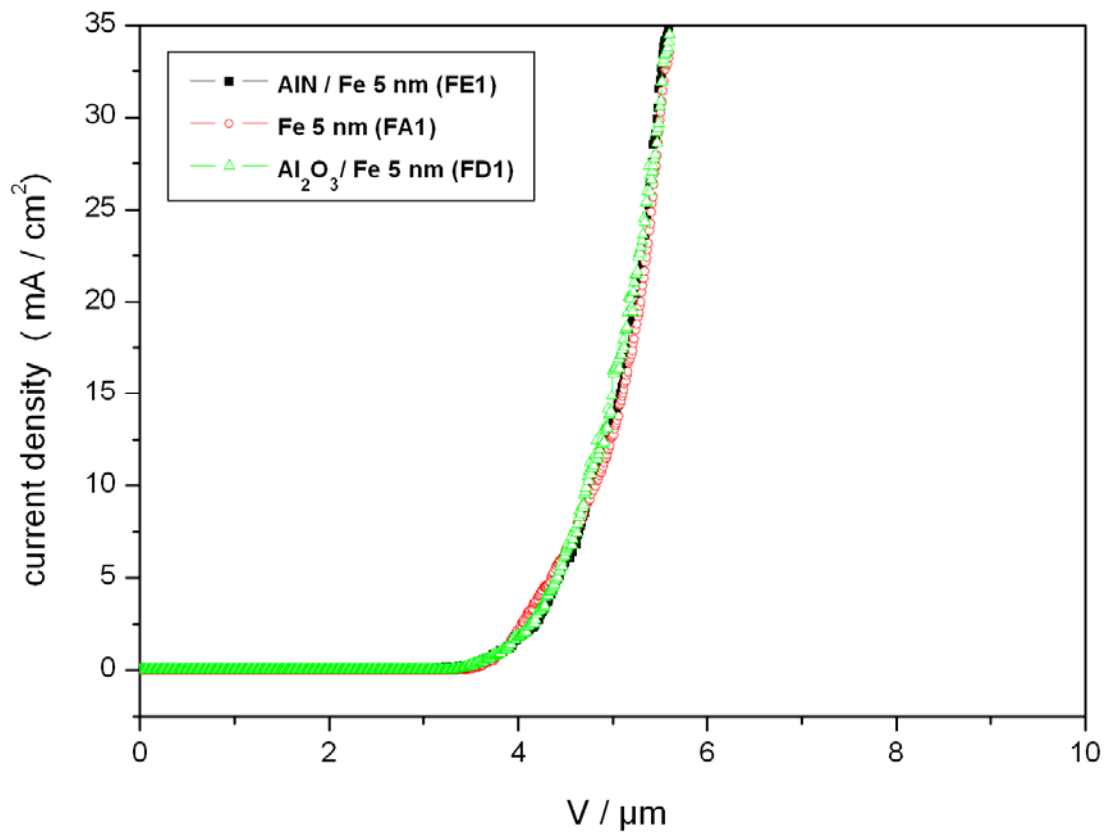


Fig. 4-32 Field emission I-V curves for the Fe-assisted CNT with native SiO_2 , Al_2O_3 , and AlN as buffer layers (Fe, 5 nm; CH_4/H_2 , 50/5 sccm/sccm).

4.4.5 Role of nitrogen

The Raman results that were presented in the previous paragraph reveal that specimens with AlN as buffer layer have higher I_G/I_D ratio and higher RBM peaks than those with Al_2O_3 . XPS and Auger analysis were employed to determine the cause. Auger depth analysis was

applied to characterize the interface conditions between Fe and AlN layer before and after H-plasma pretreatment, where Ar ion sputtering is started from the Fe catalyst and terminated on the Si wafer. Figure 4-33(a) plots the depth distribution of each element, the presence of oxygen is caused by oxidation of the film surface before loading into the chamber. Figure 4-33(b) indicates that the peaks appear at 383 eV and 389.5 eV in an etching time of 35 sec, indicating that nitrogen atoms diffuse into the Fe layer^[Soto-2004-27]. In this work, an AlN film was deposited by the PVD method and was in an amorphous state. Hence, nitrogen can move away during pretreatment because of its strong negative electron affinity^[Benjamin-1994-3288]. Nitrogen is immersed into Fe particles from the AlN layer and exhibits a concentration gradient from the interface. Kikkawa^[Kikkawa-2004-239] et al. also revealed that this behavior changes the physical properties of iron such as the large magnetization. Hence, the diffusion of nitrogen into Fe particles is believed to change the physical properties, and to be the main factor that affects the I_G/I_D ratio of as-grown CNTs. Two possible roles of nitrogen in the kinetics of the CNT growth^{[Jung-2001-150] [Lin-2003-1851]} have been proposed: (i) promotion of the formation of the graphitic layer on the catalyst surface and the improvement of the kinetics in the separation of the graphitic layer from the catalyst, (ii) maintenance of an active and prolonged carbon bulk diffusion of the catalysts at temperatures as low as ~ 600 °C. Since the catalyst of the growth of SWNTs is quite small and easily poisoned, we suggest that the latter role is the main reason for the higher I_G/I_D ratio of as-grown CNTs.

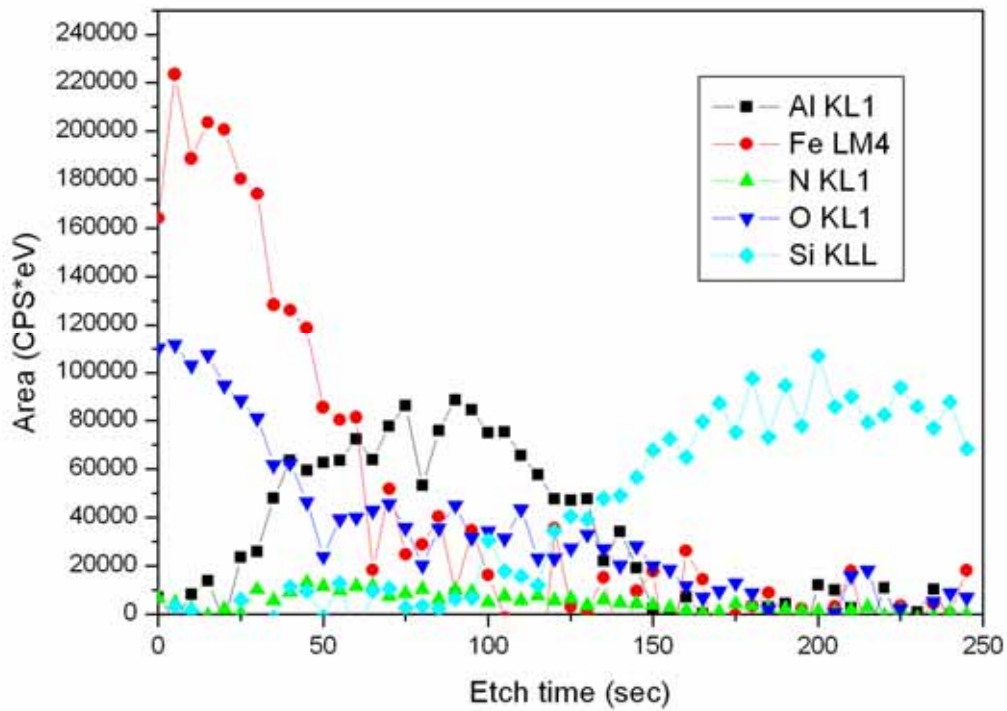


Fig. 4-33 (a) Auger depth profile as a function of etching time for the pretreated Fe/AlN/Si substrate.

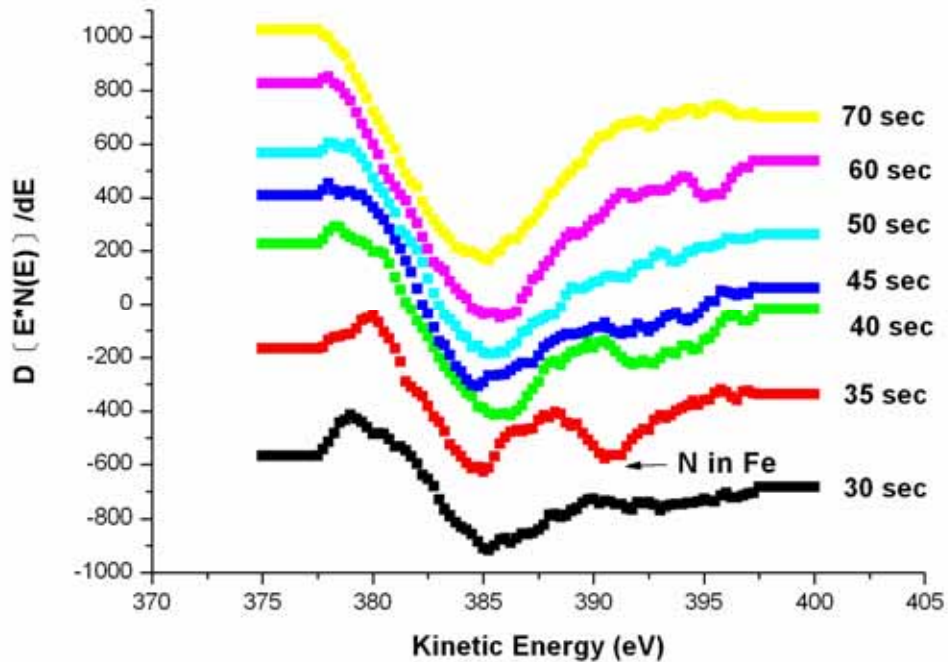


Fig. 4-33 (b) Auger electron spectra as a function of etching time for the pretreated Fe/AlN/Si substrate.

4.5 Structures and properties of the CoCrPtO_x-assisted carbon nanostructures by MPCVD

4.5.1 Morphologies and Raman spectra

Figures 4-34(a) to (f) illustrate typical FESEM morphologies of the as-grown carbon nanostructures on silicon wafer (native SiO₂) with different catalyst precursor thickness: (a) 10 nm, (b) 5 nm (c) 3 nm, (d) 2 nm, (e) 1 nm and (f) 1 nm with AlON buffer layer. Figure 4-35 (a) and (b) show the Raman spectra of as-grown carbon nanostructures, the RBM peaks in the Raman spectra indicate the presence of SWNTs in Figs. 4-32(d), (e) and (f). Therefore, it is concluded that vertically aligned SWNTs are successfully synthesized using CoCrPtO_x as precursor with thickness of 2 nm, 1 nm and 1 nm with AlON buffer layer. By contrast, entangled SWNTs rather than aligned tubes were found in the specimens that comprised a thicker as-deposited catalyst film of over ~2 nm and these results are consistent with a previous report that the catalyst must be ultra thin to enable SWNTs to be synthesized^[Noda-2005-173106]. Additionally, the specimen with buffer layer (G6) reveals a very high I_G/I_D ratio (~43), demonstrating that graphitized-degree of the as-grown SWNT films is good as that obtained by arc-discharge method, which is high temperature process^[Ando-2001-1185].

Figures 4-36(a) to (c) present typical FESEM morphologies of the as-grown SWNTs films on the silicon wafer with 1 nm thickness and AlON buffer layer. Figure 4-36(a) shows that vertically aligned SWNTs film with a height of ~60 micrometer was synthesized. The tilt-view of the specimen presented in Fig. 4-36 (b) displays SWNT films with an ultra-high volume density as high as 78 kg/m³ that considerably exceeds that reported elsewhere^[Zhong-2005-1558]. Figure 4-36(c) magnifies a portion of Fig. 36(b), to show the fabrication of the bundles of aligned SWNTs. Notably, the SWNT films can be easily removed from substrate and the SWNT films is very flexible and soft, likely the woolen blanket, as presented in Fig 4-37. Experimental results are summarized in Table 4-6.

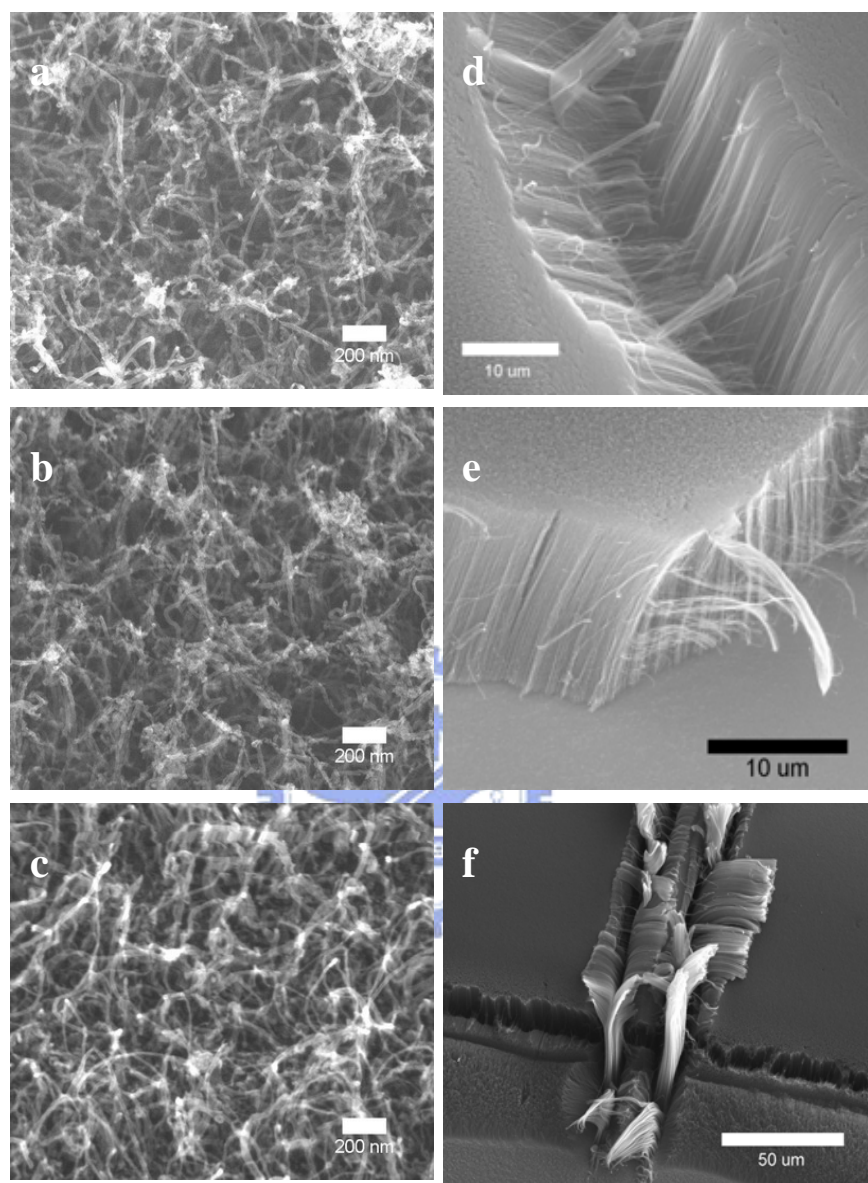


Fig. 4-34 FESEM micrographs of the CoCrPtO_x -assisted carbon nanostructures on silicon wafers (native SiO_2) with various thicknesses of catalyst layers: (a) 10 nm, (b) 5 nm, (c) 3 nm, (d) 2 nm, (e) 1 nm, and (f) 1 nm (with AlON as buffer layer), respectively.

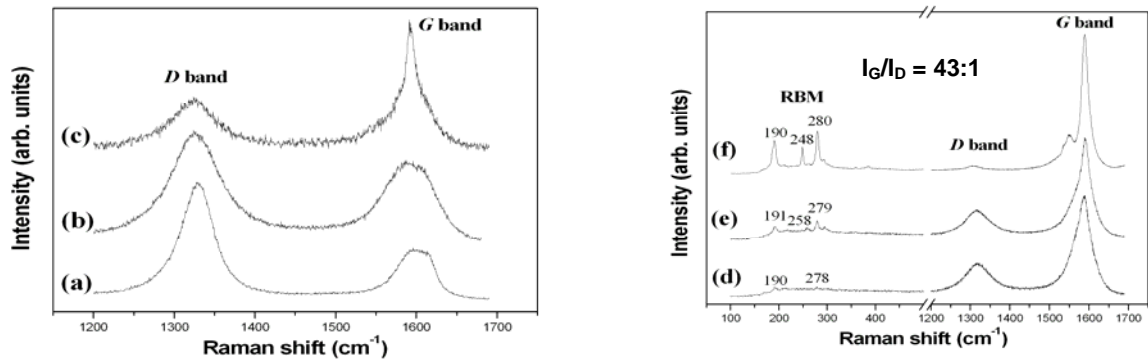


Fig. 4-35 Raman spectra of the CoCrPtO_x -assisted carbon nanostructures on silicon wafers (native SiO_2) with various thicknesses of catalyst layers: (a) 10 nm, (b) 5 nm, (c) 3 nm, (d) 2 nm, (e) 1 nm, and (f) 1 nm (with AlON buffer layer), respectively.

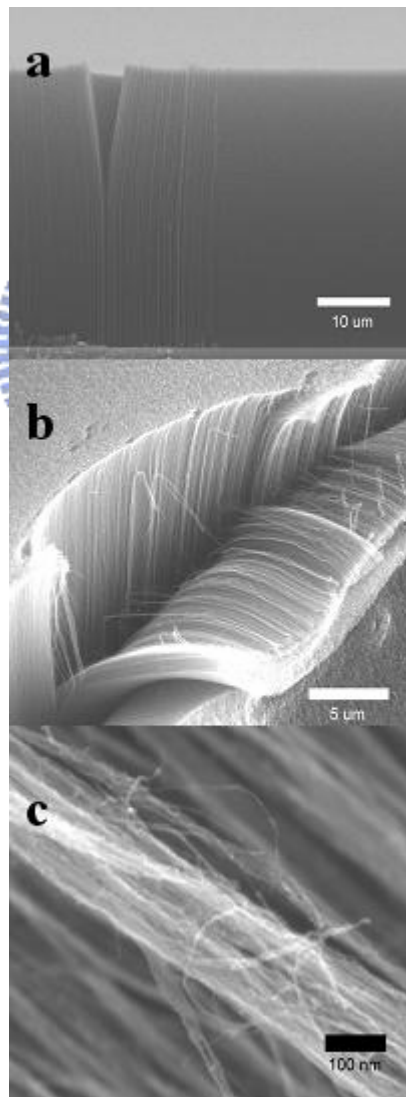


Fig. 4-36 Typical FE-SEM micrographs of extremely dense and vertically aligned CoCrPtO_x -assisted SWNTs films: (a) cross-sectional view, (b) tilt-view, and (c) highly magnified image of (b).

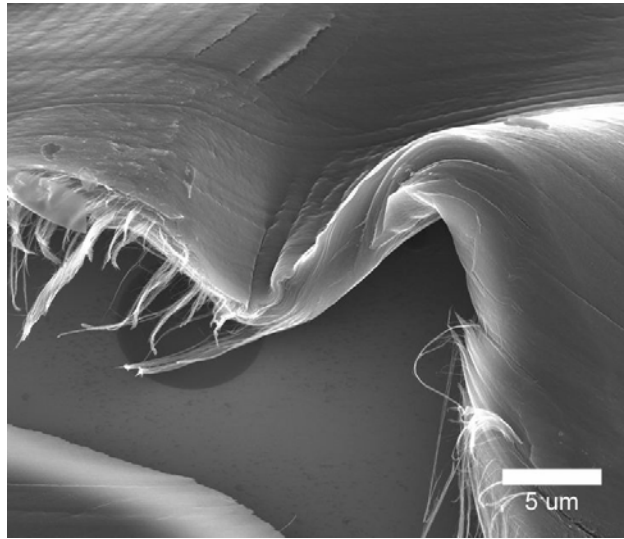


Fig. 4-37 Typical SEM micrograph of the CoCrPtO_x-assisted SWNTs films removed from silicon wafer, showing very flexible morphology.



Table 4-6 Summaries of the CoCrPtO_x-assisted carbon nanostructures on Si wafer with various catalyst thickness and buffer layer.

Specimen designations	catalyst layer thickness	Buffer layer thickness (nm)	I _G /I _D ratio	CNTs type	CNTs morphology	Corresponding figure
G1	10	Native SiO ₂	~0.5	MWNTs	Spaghetti	4-34(a)
G2	5	Native SiO ₂	~0.75	MWNTs	Spaghetti	4-34(b)
G3	3	Native SiO ₂	~2.8	MWNTs	Spaghetti	4-34(c)
G4	2	Native SiO ₂	~3.5	MWNTs + SWNTs	vertically aligned film	4-34(d)
G5	1	Native SiO ₂	~5.4	SWNTs+ trace DWNTs	vertically aligned film	4-34(e)
G6	1	AlON (10)	~43	SWNTs	vertically aligned film	4-34(f)

4.5.2 HRTEM microstructures

Figures 4-38 (a) to (c) show the TEM images of as-grown SWNT films of specimens with native SiO₂ buffer layer (G5), demonstrating that the nanotubes with diameter of ~3 nm are grown as SWNT bundles and few DWNTs (~4 nm) are detected. Hardly any MWNTs are detected by TEM and the Raman spectrum in Fig. 4-35 (e) reveals a high I_G/I_D ratio (~5.4), indicating that as-grown CNTs consist of mainly SWNTs and few DWNTs. Figures 4-39 (a) and (b) show the TEM images of as-grown SWNTs films of specimens with AlON as buffer layer (G6), demonstrating that the nanotubes are grown as SWNT bundles with diameters of 1.5 to 2 nm. Hardly any MWNTs or DWNTs are detected by TEM and the Raman spectrum in Fig. 4-35 (f) reveals a higher I_G/I_D ratio (43/1) than that with native SiO₂, supporting that almost as-grown CNTs are SWNTs.



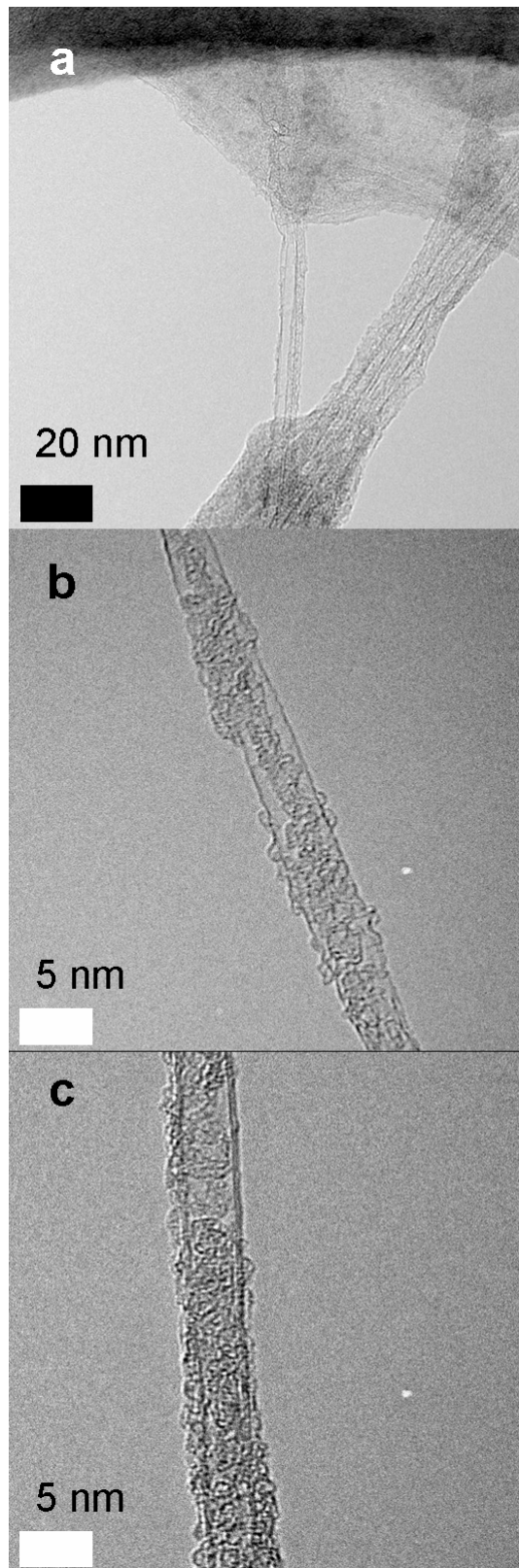


Fig. 4-38 HRTEM images : (a) typical bundle-rich SWNTs, (b) SWNT with a diameters of ~ 3 nm, and (c) DWNT with a diameter of ~ 4 nm.

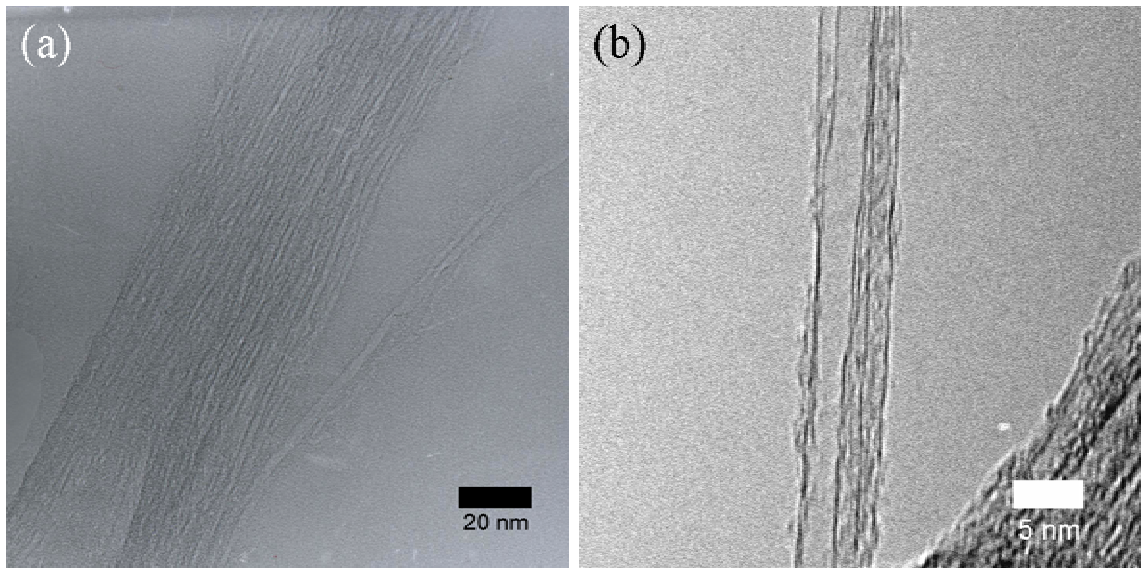


Fig. 4-39 HRTEM images of typical SWNTs: (a) most of the tubes are of the bundle type, and (b) the highly magnified image of SWNTs shows that their diameters range from 2.5 to 3.0 nm.

4.5.3 Field emission properties and TGA

Figure 4-40 displays the field emission current density as a function of electric field for the as-grown well-aligned SWNT of sample G6 (CoCrPtO_x 1 nm with AlON as buffer layer), showing a turn-on voltage of 4.6 V/μm (0.01 mA/cm²) and a current density of 6 mA/cm² (7.2 V/μm). Since the tube density is very high, no excellent field emission properties was obtained in this study due to screening effect.

Figure 4-41 presents the thermo-gravimetric analysis (TGA) result of the as-grown SWNTs of 5 mg, indicating the combustion range of the SWNTs was 586°C to 691°C, with the peak weight reduction occurring at 650°C, which is very similar to that of purified, high-quality SWNTs synthesized by a laser-oven method^[Chiang-2001-8297]. It is believed that the small initial weight increase is due to physisorption, supported by the fact that the weight returns to its initial value by subsequent annealing. No measurable residue remained after heating above 700°C, indicating purity of SWNTs is very high (~99 %).

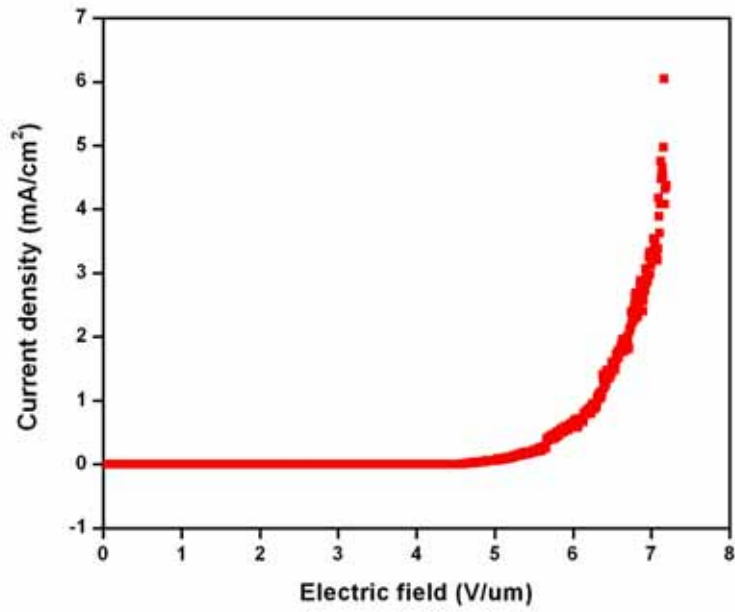


Fig. 4-40 Field emission I-V curve for the CoCrPtO_x-assisted SWNTs films with AlON as buffer layers (Specimen G6).

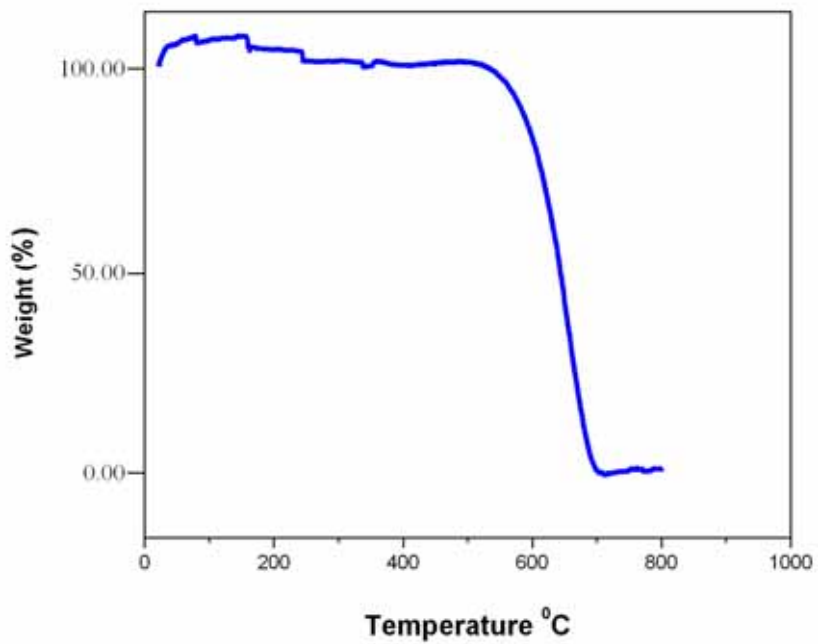
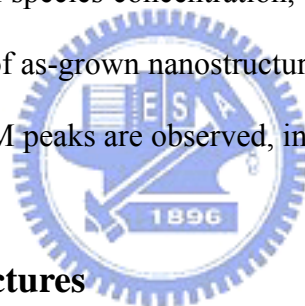


Fig. 4-41 TGA curve of the CoCrPtO_x-assisted SWNTs films in air (heating rate is 10°C/min).

4.6 Structures of CoCrPtO_x-assisted carbon nanostructures by ECR-CVD

4.6.1 Morphologies and Raman spectra

Figures 4-42 (a) to (f) display typical FESEM morphologies of the as-grown carbon nanostructures on silicon wafer (native SiO₂) with different catalyst thickness and working pressure: (a) 2 nm, 4x10⁻³ Torr; (b) 2 nm, 4x10⁻² Torr; (c) 2 nm, 4x10⁻¹ Torr; (d) 2 nm, 4 Torr; (e) 1 nm, 4 Torr and (f) 1 nm with AlON as buffer layer, 4 Torr. These results present that spaghetti-like CNTs were formed and its amount is increased as working pressure increases. By contrast, no obvious difference is observed when catalyst thickness is reduced to 1 nm (I5) or with buffer layer application (I6). It is assumed that high working pressure will increase ion colliding frequency and carbon species concentration, which provide favorable conditions for CNTs growth. Raman spectra of as-grown nanostructures (Specimens I4 to I6) display the low I_G/I_D ratios (~0.58) and no RBM peaks are observed, indicating the absence of SWNTs.



4.6.2 HRTEM microstructures

Figures 4-43(a) to (c) present typical HRTEM morphologies of the as-grown CNTs on the silicon wafer with 2 nm thickness, indicating the as-grown CNTs are consisted of mainly four-walled CNTs with an average diameter about 7.9 nm, few 3.6 nm double-walled CNTs (DWNTs) and SWNTs, which are the smallest reported sizes of CNTs in the literature by ECRCVD^[Minea-05-1101]. SWNTs are found by TEM observation but no RBM signals are detectable and low I_G/I_D ratio is obtained in Raman spectra, suggesting that as-grown CNTs possess many defects or disorders due to heavy ion bombardment from ECRCVD plasma.

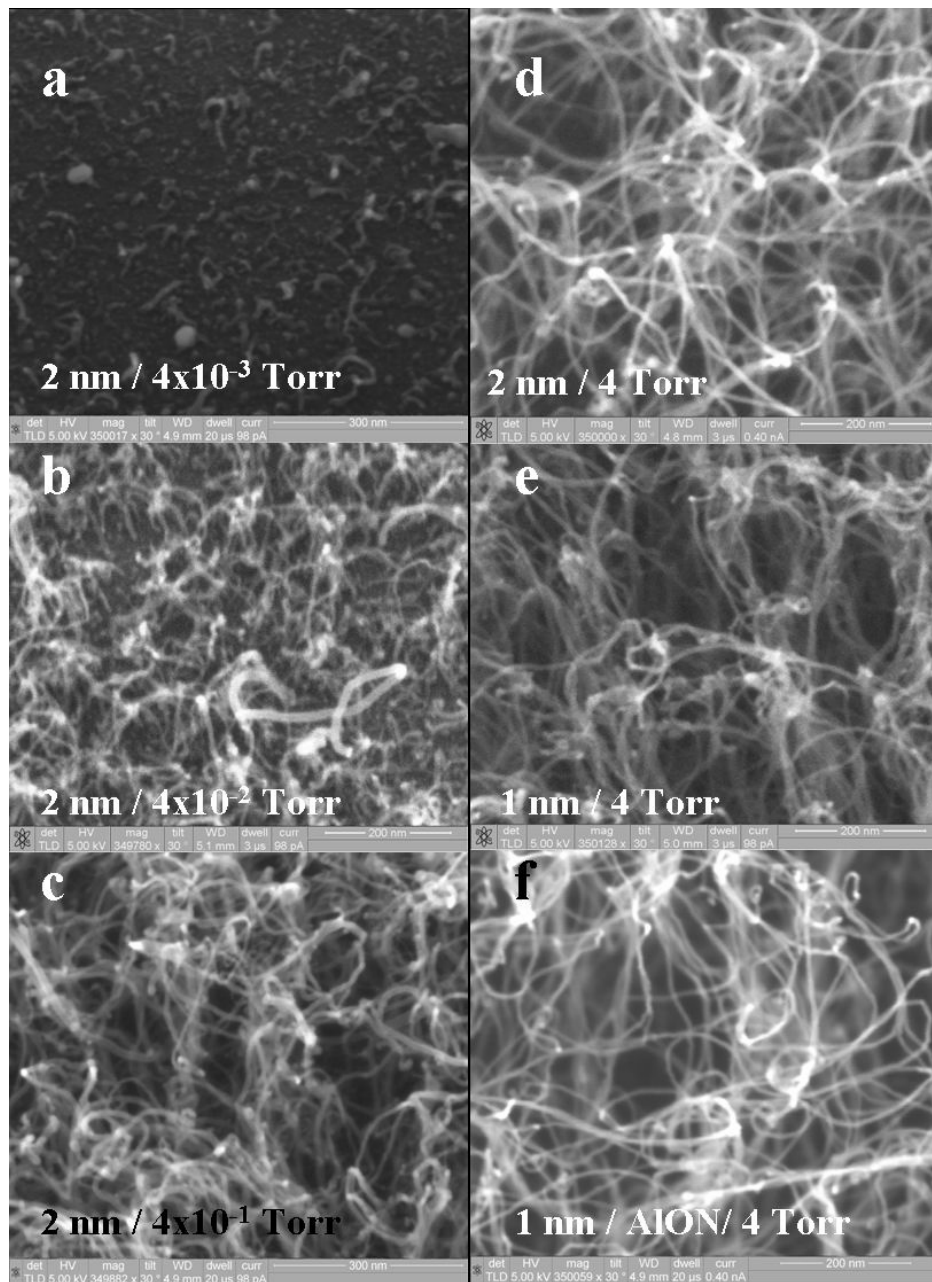


Fig. 4-42 FESEM micrographs of the CoCrPtO_x -assisted carbon nanostructures on silicon wafers (native SiO_2) with various thicknesses of catalyst layers and working pressures: (a) 2 nm, 4×10^{-3} Torr (b) 2 nm, 4×10^{-2} Torr (c) 2 nm, 4×10^{-1} Torr (d) 2 nm, 4 Torr (e) 1 nm, 4 Torr and (f) 1 nm with AION buffer layer, 4 Torr, respectively.

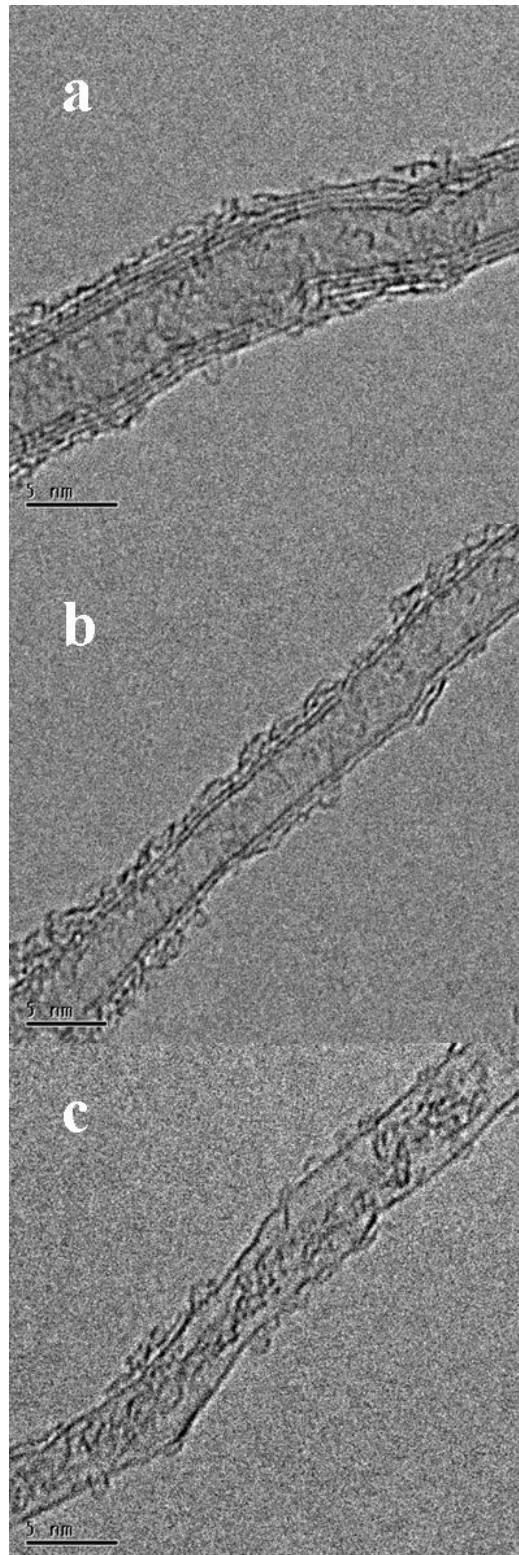


Fig. 4-43 HRTEM images of typical CNTs : (a) 4-wall MWNT (~ 7.9 nm), (b) DWNT with a diameters of ~ 3.6 nm, and (c) SWNT with a diameter of ~ 3 nm.

CoCrPtO_x catalyst precursor was applied to develop a process to successfully synthesize the small sized (< 8 nm in average diameter) carbon nanotubes (CNTs) on Si wafer by electron cyclotron resonance chemical vapor deposition (ECR-CVD) method with CH₄ and H₂. The experimental results demonstrate that as-grown CNTs consisted of small sized MWNTs (4-walled), DWNTs and SWNTs under the following conditions: negative substrate bias of -100 V, CH₄/H₂ of 4/50 sccm/sccm, microwave power of ~1000 W, ≤2 nm catalyst thickness and under ~ 4 Torr pressure. Experimental results are summarized in Table 4-7.

Table 4-7 Summaries of the CoCrPtO_x-assisted carbon nanostructures on Si wafer by ECRCVD.

Specimen designations	catalyst layer thickness	Buffer layer thickness (nm)	Working pressure (Torr)	I _G /I _D ratio	CNTs type	CNTs morphology	Corresponding figure
I1	2	no	4x10 ⁻³	-	-	Particle-like	4-22(a)
I2	2	no	4x10 ⁻²	0.58	MWNTs	spaghetti	4-22(b)
I3	2	no	4x10 ⁻¹	0.56	MWNTs	spaghetti	4-22(c)
I4	2	no	4	0.56	MWNTs, trace DWNTs and SWNTs	spaghetti	4-22(d)
I5	1	no	4	0.52	-*	spaghetti	4-22(e)
I6	1	AlON (10)	4	0.56	-*	spaghetti	4-22(f)

*: It was estimated to be MWNTs, trace DWNTs and SWNTs.

4.7 My proposed growth mechanism of SWNTs

4.7.1 Growth mechanism of network-like Co-assisted SWNTs

Figures 4-5 (c) and (e) show that Co catalyst films with AlON and Al₂O₃ as buffer layer become large particles after pretreatment and SWNT networks are following formed but not CNTs are synthesized in the specimen with AlN, ZnS-SiO₂, and native SiO₂ buffer layer. Therefore, it is believed that Al-based buffer layer (AlON and Al₂O₃) play a key role to affect growth mechanism.

Since Govindaraj^[Govindaraj -1999-2567] reported that CoAl₂O₄ is effectively to enhance SWNTs formation, to clarify whether CoAl₂O₄ and other compound (e.g., Co₃O₄) participate this effect, the XPS analysis of carbon nanostructures (specimen with AlON as buffer layer) was performed as shown in Fig. 4-44. It is found that Co peak appears at the 784 eV and a small shifted value (pure Co peak is at 782 eV) maybe resulted from the slightly oxidation due to the sample exposing to the air before analyzing. It is as expected that the most strong intensity oxygen peak appears at 532 eV from AlON layer which is very close to the peak of Al₂O₃ (531.1 eV), indicating no existence of other Co oxide (oxygen peak will appears at 536.1 eV if Co₃O₄ is formed^[Ram-2001-3745]). Furthermore, it is found that Al peak appears at 75 eV, indicating no other aluminum compounds forming, such as CoAl₂O₄, where Al peak is 73.6 eV^{[Patterson-1976-1702] [Nevedo-1982-29] [Wagner-1980-83]}. Therefore, we can conclude that there is no compounds formation and the effects to enhance SWNTs growth is mainly governed by Al-based buffer layer. Furthermore, it is proposed that the large-sized pre-treated Co particles are caused by higher surface tension between of Co and Al-based buffer layer.

Table 4-1 displays the roughness of AlON films and Al₂O₃ (5 and 10 nm) is larger than 1 nm, whereas AlN is quite neat whose roughness (R_{rms}) are on the order of angstroms at most. These results suggest the protrusion on rough buffer layer (e.g., AlON) can cause instabilities on Co catalyst surface and form nuclei sites for tubes growth afterwards. This heterogeneous nucleation phenomenon of metal deposited on oxide film has been revealed in past

study^[Baumer-1999-127]. On the other hand, Al-based buffer layer may act as template for Co catalyst film to promote formation of nano-sized extrusions (nuclei sites) for the root-growth SWNTs. Additionally, the specimen with AlON as buffer layer (R_{\max} , ~0.97 nm) demonstrates stronger RBM peaks and higher I_G/I_D ratio than that with Al_2O_3 which has larger roughness (R_{\max} , ~1.55 nm). Therefore, we conclude the buffer layer with appropriate roughness value is the favorable condition to form nano-sized extrusions on the catalyst for SWNTs growth.

Except the nucleation factor, it is well known that the carbon solubility of the catalyst is also the most important issue. Previous researches^[Kim-2001-35] reported that alumina supported transition metal possess higher reactivity for NO reduction by C_3H_6 . Furthermore, Matolin,s group^{[Stara-1996-69] [Nehasil-1997-813] [Jungwirthova -1997-644]} also revealed that adsorption and dissociation probability of CO gas on metal particles, which deposited on alumina substrate, will be increased due to the surface diffusion effect. These findings suggest that reaction activity of alumina-supported metal is increased remarkable. It is believed that carbon species dissociated from the source gas will diffuse into the catalyst particles along the alumina surface and dissolved into the catalyst. This phenomenon will cause the catalyst possess higher carbon species concentration than those without alumina supported (Si substrate or native SiO_2) and provides a favorable condition for CNTs growth. Another possible reason is that Al-based layer can inhibit the carbon diffuse into Si wafer directly and accelerate other carbon diffusion path during CNTs growth, which supports a reasonable explanation that SWNTs can grow from Co catalyst successfully under quite low temperature (~620 °C) in our study.

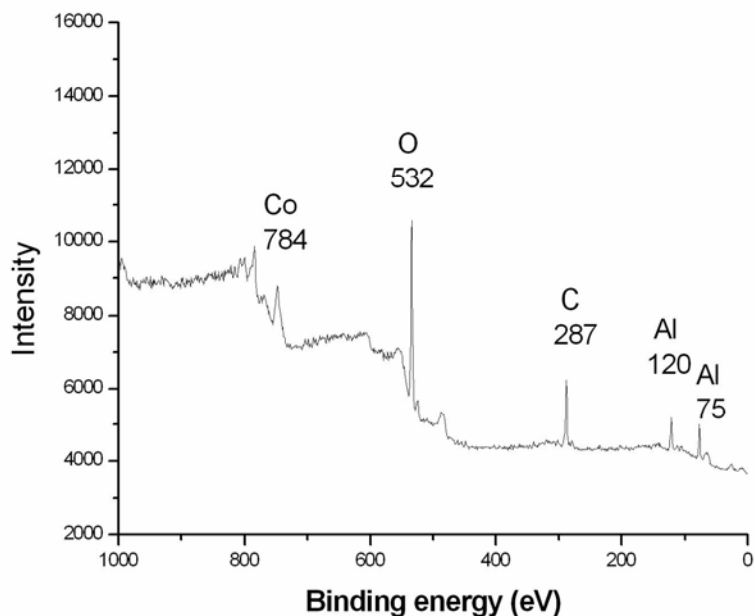


Fig. 4-44 XPS spectrum of as-deposited Co-assisted carbon nanostructures on silicon wafer with AlON as buffer layer.

We present a sketch of the proposed scenario in Fig. 4-45. The first step is that large sized crystallites are formed after pretreatment, which are determined by the surface tension between Co and buffer layer. The numerous instabilities (nano-sized extrusions), which are resulted from the protrusions on the rough AlON buffer layer, are formed on the surface of Co catalyst particles as the nuclei for tube growth (Fig. 4-45b). Second step is the dissolution of carbon and precipitation of supersaturation carbon from the catalyst particles (Fig 4-45c). Carbon species will diffuse into the catalysts along the substrate surface except catalyst surface and the supersaturation carbon will precipitate from nuclei at the lateral zone of Co particles where the temperature is relatively low.

Third stage is the growth process of root-growth SWNTs depicted in Fig. 4-45d. The numerous of SWNTs ropes are grown and formed as bundles of SWNTs due to van der Waal force. There is a competition between nucleation of SWNTs and graphitic layers at this stage. It is in agreement with the proposed models by Saito and Gavillet et al. and explains that we can observe some particles covered graphite layer only and CNTs were not found under some

experimental conditions. Saito et al. [Saito-1994-526] proposed the rapid cooling rate of catalyst particles, which can promote the nuclei formation, and high super-saturation carbon are the favorable conditions to grow SWNTs. However, the cooling rate in an MPCVD system cannot be achieved the similar rate as arc-discharge method because our presenting process temperature is only ~ 620 °C. Restated, formation of the nuclei on the catalyst surface is not dominated by cooling rate but the other factors. In this work, we propose that thin amorphous AlON buffer layer, which provides appropriate rough surface as the template for Co film to promote formation of nano-sized extrusions, mainly dominates the growth mechanism of root-growth SWNTs. Finally, when the growth time is long enough, few layers of graphitic layers will be formed and force SWNTs ropes to depart from catalyst (Fig. 4-45e).

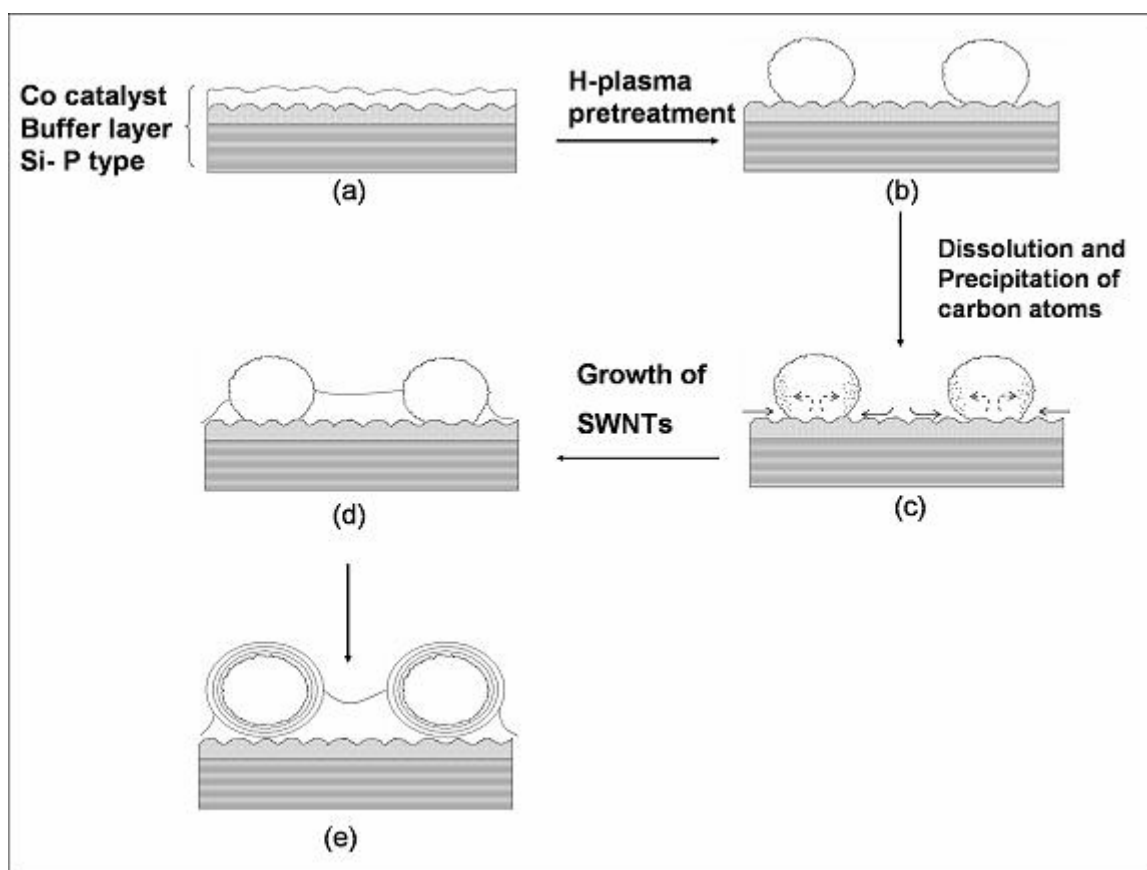


Fig. 4-45 Hypothetical growth process of network-like root-growth Co-assisted SWNTs at low temperature by MPCVD.

In summary, we suggest that Al-based buffer layer material is the key factor to enhance the formation of network-like root-growth Co-assisted SWNTs, the Al-based buffer layers essentially have the following functions: (i) affecting interactions^[郭正次-2004-p.8-18] between catalyst and buffer materials, in which higher surface tension of catalyst with Al-based buffer material cause the large-size catalyst particles after pretreatment, (ii) acting as template for the Co catalyst film to promote formation of nano-sized extrusions on catalyst surface, and (iii) acting as the carbon diffusion inhibitor to reduce the possible diffusion path of carbon through Si wafer and to accelerate other carbon diffusion paths during CNTs growth, which may reduce the deposition temperature (~ 600 °C) of SWNTs.

4.7.2 Growth mechanism of spaghetti-like Fe-assisted SWNTs

Previous results showed that well-distributed and small-sized particles were formed on Si wafers with Al_2O_3 and AlN as buffer layer materials and spaghetti-like Fe-assisted SWNTs can be synthesized afterward. By contrast, no SWNTs are fabricated with native SiO_2 , Si_3N_4 and TiN buffer layers where their pretreated particles size is quite large. Thus, it is proposed that size of pre-treated nanoparticles is the key factor to affect SWNTs growth where buffer layer materials determine the sizes of pre-treated particles. There are two possible reasons to explain why the small-sized catalyst particles can be formed with Al_2O_3 and AlN as buffer layers. Al-based buffer layers essentially have the following functions: (i) providing the proper nano-sized dimples on their surface to accommodate the nanoparticles from agglomeration between neighbor nanoparticles, (ii) affecting interactions between catalyst and buffer materials, this mechanism can support the fact that small-sized particles can be formed on Si wafer with AlN buffer layer, which demonstrates very small roughness. Furthermore, Al-based buffers can act as the carbon diffusion inhibitor to reduce the possible diffusion path of carbon through Si wafer and to accelerate other carbon diffusion paths during CNTs growth, which may reduce the deposition temperature (~ 600 °C) of SWNTs by combining with

smaller particle sizes.

Furthermore, we propose that each tube is grown from individual catalyst particle whose size determines the tube diameter and may follows yarmulke model because HRTEM micrograph (Fig. 4-30) displayed that catalyst trapped at the tip or bottom of CNTs has a similar diameter as tube. To clarify whether this model follow tip or base growth mechanism, EDX analytical results are performed and displayed in Fig. 4-46. There are not peaks of Fe signal can be detectable at the top of CNT film, indicating that Fe catalyst particles after CNTs growth still remained onto the substrate. This results support that spaghetti-like Fe-assisted CNTs follow base-growth model.

We present a sketch of the proposed scenario in Fig. 4-47. The first step is that small sized catalyst particles are formed after pretreatment under appropriate buffer layer materials. Second step is the dissolution of carbon and precipitation of supersaturating carbon from the catalyst particles (Fig 4-47c). Then spaghetti-like base-growth Fe-assisted SWNTs are grown from individual catalyst particles.

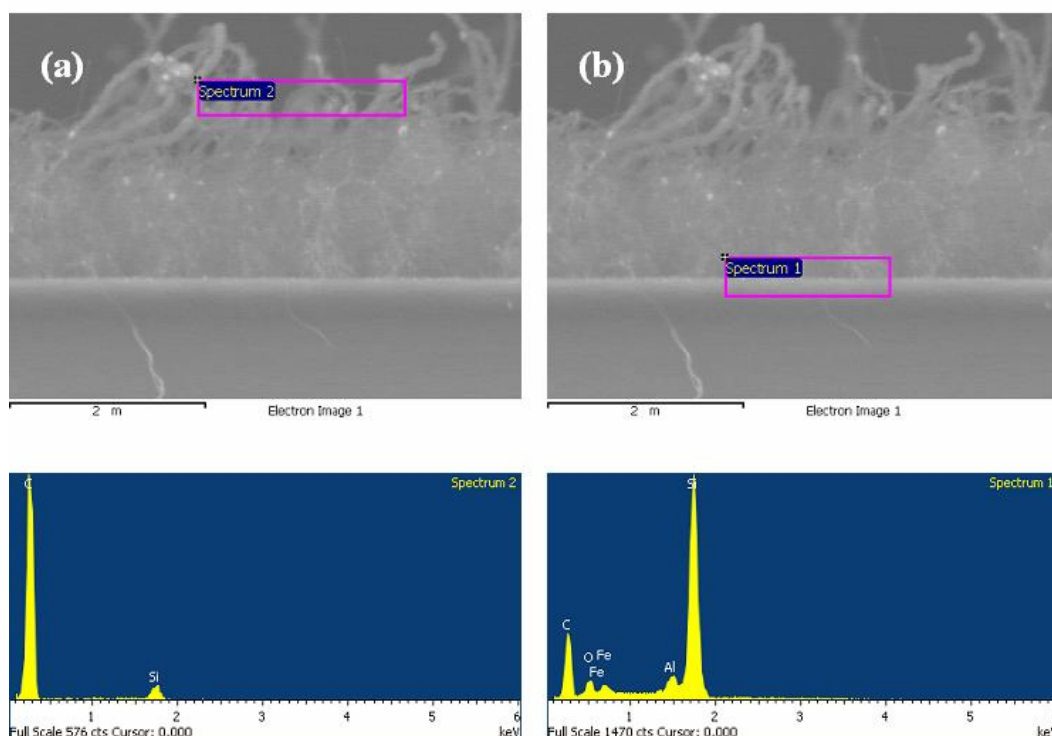


Fig. 4-46 EDX analysis of the Fe-assisted CNTs film on Si wafer : (a) top of CNTs film, no Fe signal is detected, and (b) bottom of CNTs film, Fe signals are detected indicating Fe catalyst particles remained on Si wafer after CNTs growth.

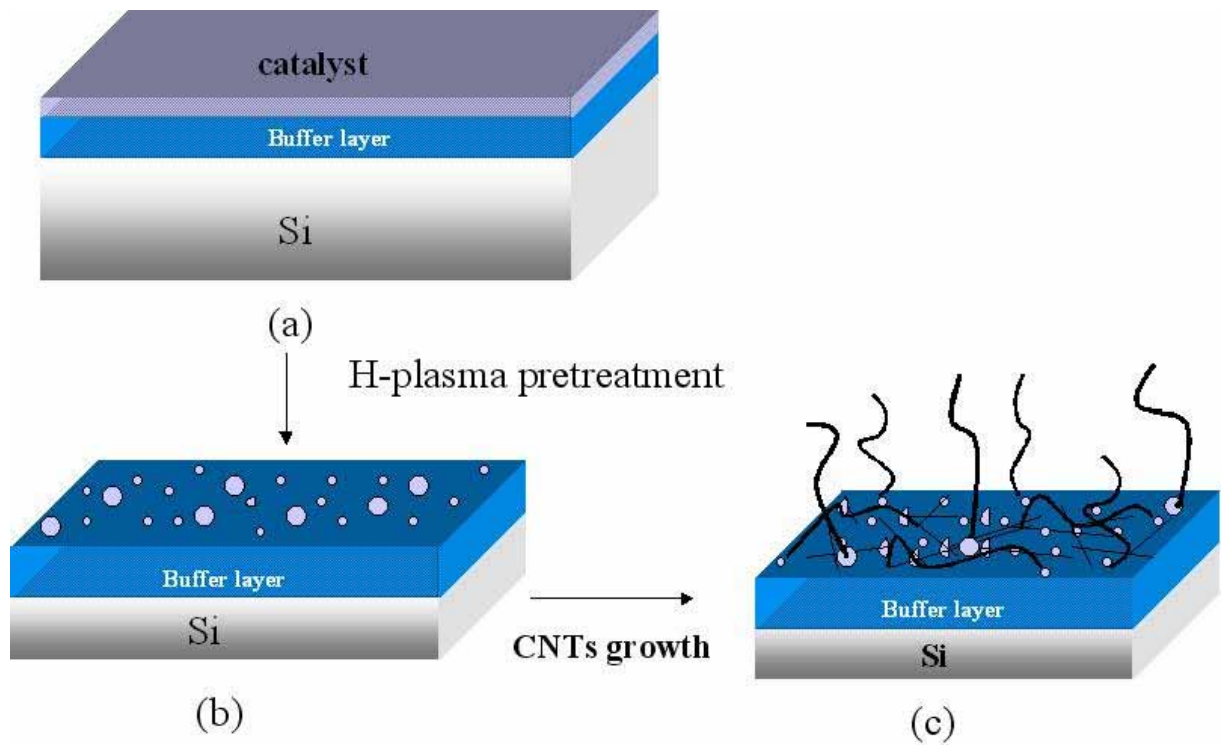


Fig. 4-47 Hypothetical growth process of spaghetti-like Fe- and buffer-assisted SWNTs by MPCVD.

4.7.3 Growth mechanism of the CoCrPtO_x-assisted SWNTs

a. Decomposition mechanism of CoCrPtO_x catalyst precursor

Figures 4-48(a) to (c) present the results of the XPS of an as-deposited CoCrPtO_x film formed by PVD and after H-plasma pre-treatment (MPCVD), respectively, to study how an oxidized CoCrPt film can form small nano-particles and prevent the agglomeration of catalyst as the buffer layer did in an earlier work^{[de los Arcos-2004-187] [Delzeit-2001-368] [Zhong-2005-1558]}. The spectra indicate that PtO_x, CrO_x, and CoO^[Wagner-1993-76] phases are formed simultaneously in the as-deposited film during reactive sputtering deposition by PVD. Furthermore, the PtO_x associated with a peak at 74.05 eV (4f_{7/2}) comprises PtO (73.8 eV) and PtO₂ (74.6 eV), while CrO_x (577.4 eV) consists of CrO₂ (576.3 eV) and CrO₃ (578.3 eV), respectively^[Wagner-1993-76]. The spectrum presented in Fig. 4-48(a) shows that the Pt peak is shifted by 1 eV after pre-treatment, indicating that most PtO_x atoms are reduced to Pt atoms in the H₂ atmosphere, but a small quantity of PtO_x remains. This is caused by surface oxidation of exposing samples to the air before loading them in XPS chamber. Most interestingly, the Cr phase in Cr₂O₃

remains^[Wagner-1993-76], suggesting that the effects of formation of nano-particles from CoCrPtO_x catalyst precursor film are mostly from the reduction of PtO_x or CoO. However, this effect is driven mainly by PtO_x and will be discussed in the following paragraph.

Recently, PtO_x has been demonstrated to be an active layer for use in the next generation of optical storage media applications^{[Kikukawa-2002-4697] [Kim-2003-1701]}, from which, oxygen is released after prolonged laser heating to compress the adjacent layers to form pits as recording marks, which consist of oxygen bubble gas and fine Pt nanoparticles. Therefore, the explosion-like phenomenon associated with the reduction of PtO_x (PtO/PtO₂) may cause the formation of very fine particles and such behavior may depend on the process temperature. In this experiment, a too low pre-treatment temperature (below 500 °C) results in an incomplete reduction of a CoCrPtO_x catalyst precursor film and non-uniform larger catalytic particles are formed, then, only MWNT can be synthesized. This difference is due to the fact that CoCrPtO_x catalyst precursor film has a higher critical decomposition temperature than PtO_x (~500 °C)^[Kolobov-2005-121909]. Compositions of CoCrPt target, as-deposited CoCrPtO_x film and pretreated CoCrPtO_x film on Si wafer by XPS depth analysis are listed in Table 4-8. These results are taken after ion gun etching with depth of 2 nm to avoid the effect of surface oxidation. Oxygen can be found in the pretreated CoCrPtO_x film. This result is in agreement with XPS spectra that Cr₂O₃ remains in pretreated film.

Table 4-8 Compositions of CoCrPt target, as-deposited CoCrPtO_x film and pretreated CoCrPtO_x film on Si wafer by XPS depth analysis.

Element	C	N	O	Si	Cr	Co	Pt
Target (at %)	-	-	-	-	10.97	57.08	31.95
As-deposited (at %)	1.18	0	50.08	0	5.41	37.66	5.66
Pretreated (at %)	6.10	0	14.94	0	6.97	62.16	9.83

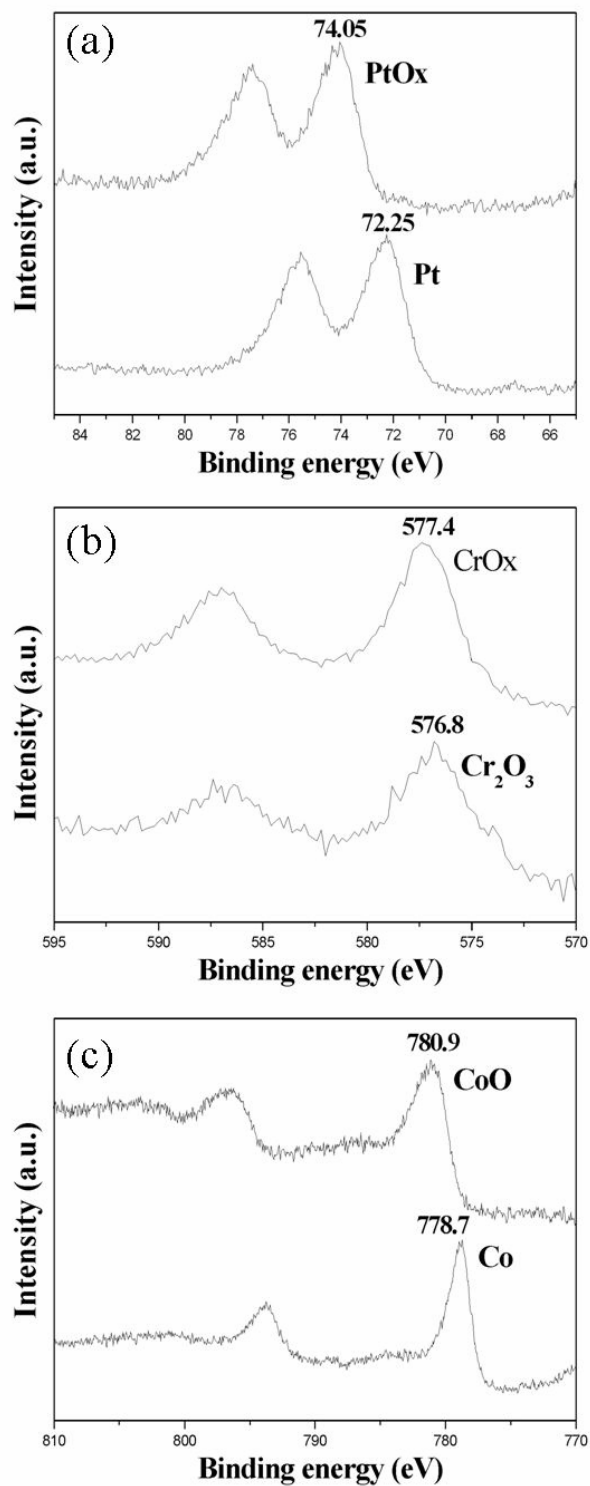


Fig. 4-48 XPS spectra of the CoCrPtO_x-coated substrates before and after H-plasma pretreatment for various element or compound in the films : (a) Pt, PtO_x (b) Cr₂O₃, CrO_x and (c) Co, CoO. Upper curves refer to as-deposited films and lower curves represent the pre-treated films.

With respect to the role of Cr, Cr_2O_3 can inhibit the agglomeration of particles. Hence, it is believed to play a role in suppressing the agglomeration of catalytic particles in the H-plasma pretreatment and CNTs growth processes. The Co element has an essential role in the dissolution and precipitation of carbon species in the SWNT films growth because the dissolution of carbon in Cr_2O_3 and Pt is rather small. The earlier work demonstrates that the pure Co catalytic nano-particles can also be formed by the reduction of CoO that is prepared as a chemical complex solution^[Kong-1998-567]. However, the nanoparticles with large size distribution and low density will not support SWNTs growth. Therefore, it is concluded that nano-particles from the decomposition of CoCrPtO_x film mainly comes from PtO_x but not CoO. The decomposition mechanism that involves the exploding effect associated with the reduction of CoCrPtO_x film enables the size and distribution of the catalysts particles to be manipulated to fabricate SWNTs with the desired morphology by controlling the composition, thickness and H-plasma pre-treatment temperature of CoCrPtO_x film.

Pure Co catalyst film, and the as-deposited CoCrO_x and CoCrPtO_x films, were prepared for experimental comparison under the same process conditions, to confirm more accurately the indispensability of Cr and Pt to this effect. Figures 4-49(a) to (c) presents the FESEM morphologies of the various catalysts following H-plasma pretreatment. The FESEM result reveals that small Co catalyst particles cannot be formed after H-plasma pretreatment. Smaller particles are formed in a pretreated CoCrO_x film, in which Cr_2O_3 is involved in inhibiting the agglomeration of particles, as stated above. However, the particles sizes are not sufficiently small for SWNTs growth. By contrast, Fig. 4-49 (c) reveals that small particles can be formed in a CoCrO_x film. Therefore, the coexistence of oxide of Cr and Pt in the CoCrO_x catalyst film favors the formation of small catalyst particles for growing SWNTs. The effect of the composition of CoCrPt on the formation of nano-particles must be discussed in the future.

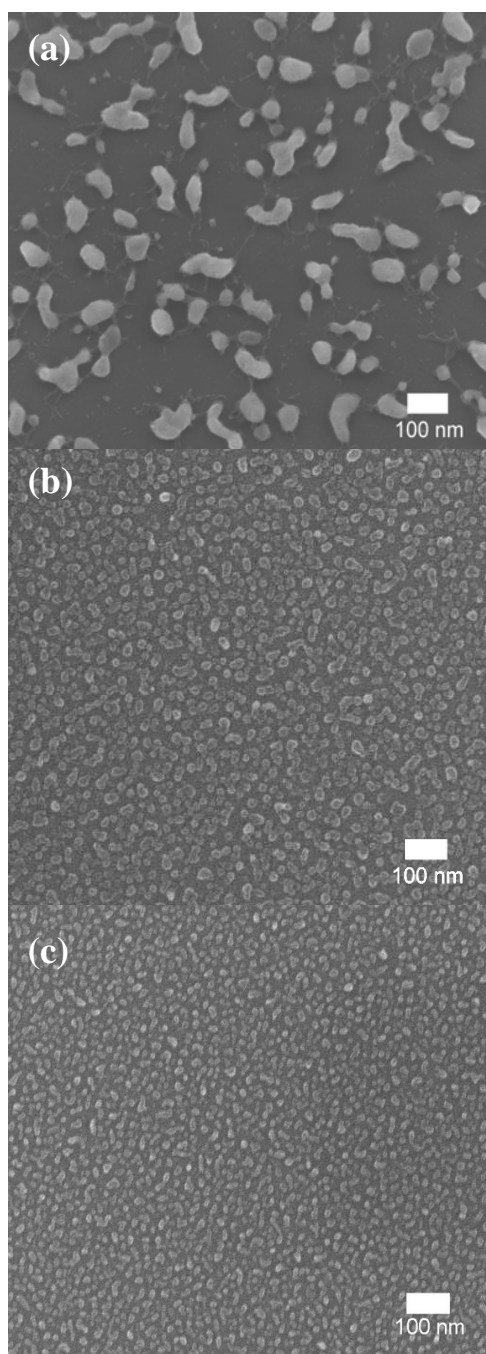


Fig. 4-49 Typical FE-SEM micrographs of various H-plasma pretreated catalysts: (a) pure Co, (b) CoCrO_x and (c) CoCrPtO_x thin film.

b. Growth mechanism of vertically aligned SWNTs films by MPCVD

To verify the growth mechanism of as-grown SWNTs films, the EDX analysis is used to study substrate whose as-grown SWNTs films are removed, and the result (Fig. 4-50) shows the catalysts existed on the Si substrate, suggesting the growth mechanism of as-grown SWNTs may follow a base-growth model. Interestingly, Si substrate whose as-grown SWNTs films are removed can be used to grow carbon nanostructures and the fabrication of dense SWNTs films with similar quality found to be repeatable (Fig 4-51). These results confirm that the CoCrPtO_x -assisted SWNTs films follow base-growth model. With respect to the fabrication of the extremely dense SWNTs films, highly dense and very fine catalytic particles are uniformly formed after H-plasma pre-treatment (Figures 4-10 and 4-11) and aligned tubes are then grown vertically, constrained among the tubes. By contrast, if the distribution densities of fine catalytic particles are low, entangled SWNTs are formed. Since tube shows similar diameter with pretreated particle size from HRTEM micrographs, it is concluded that each SWNT may grown from individual catalytic nanoparticles. Regarding the effect of Al-based buffer layers, it is considered that the proper mesoporous pore sizes on their surface to further prevent the nanoparticles from agglomeration. This assumption is in agreement with previous results that AlON buffer layer can increase the tube density.

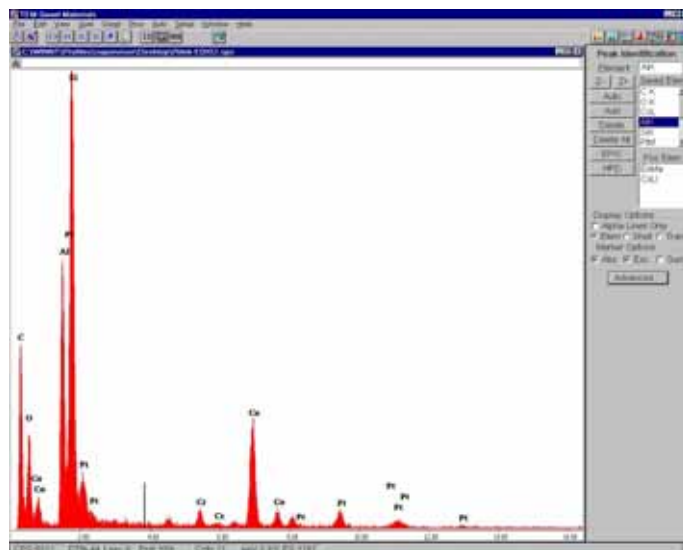


Fig. 4-50 EDX analysis of the substrate-side of the CoCrPtO_x -assisted SWNTs film on Si wafer.

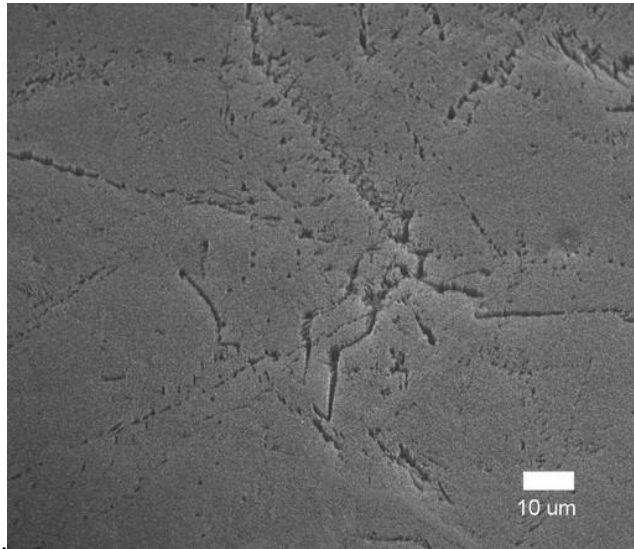


Fig. 4-51 Top-view FE-SEM micrograph of the CoCrPtO_x-assisted SWNTs films on the used substrate by wiping out the previously deposited CNTs films..

c. Growth mechanism of the small sized CoCrPtO_x-assisted CNTs by ECRCVD

We performed a same experiment as that of MPCVD in last paragraph. The as-grown small sized CNT films on the Si wafer whose is removed to grow carbon nanostructures under the same process conditions and the as-grown CNTs films with similar morphology found to be repeatable. This result suggests that the CoCrPtO_x-assisted CNTs by ECRCVD also follow the base-growth model. Moreover, HRTEM micrographs of pretreated particles (Figs 4-13, 4-14) demonstrate that their density is not high enough; supporting that only entangled CNTs can be synthesized from SEM observation. The HRTEM results (Figs 4-41 a to c) display that tube diameter is similar with pretreated catalyst size and each tube (SWNT, DWNT and MWNT) may grow from individual catalytic nanoparticles.

4.7.4 Effect of specimens stacking sequences

The catalyst-coated side of substrate is placed downward on the top of a Si wafer during CNTs growth, to eliminate difficulty of formation of carbon nanostructures (Fig 4-52 a). Figure 4-52 (b) demonstrates a typical image of a specimen after CNTs growth (G5). Notably, dense SWNTs films are formed in the inner area but hardly any CNTs re presented outside

this area, perhaps because the diffusion path of carbon species varies with the stacking sequence of the specimens. Carbon species are proposed herein to diffuse mainly into catalyst particles along the surface of the substrate because the catalyst-coated side of the specimen is placed downward and the catalyst particles outside the area are rapidly poisoned by contact with excess carbon species. As the carbon species diffuse along surface into the inner area, the carbon concentration can be controlled and then SWNTs grown. Since the carbon diffusion path is along the substrate surface, the buffer layer on the Si wafer may affect the diffusion of carbon species. Furthermore, a Al-based buffer layer with a rough surface may vary the diffusion speed or path, potentially inhibiting the excess carbon atom and rapidly poisoning the catalyst particle. This fact is one cause of the improvement of the density and length of the tubes by the application of AlON buffer layer herein.

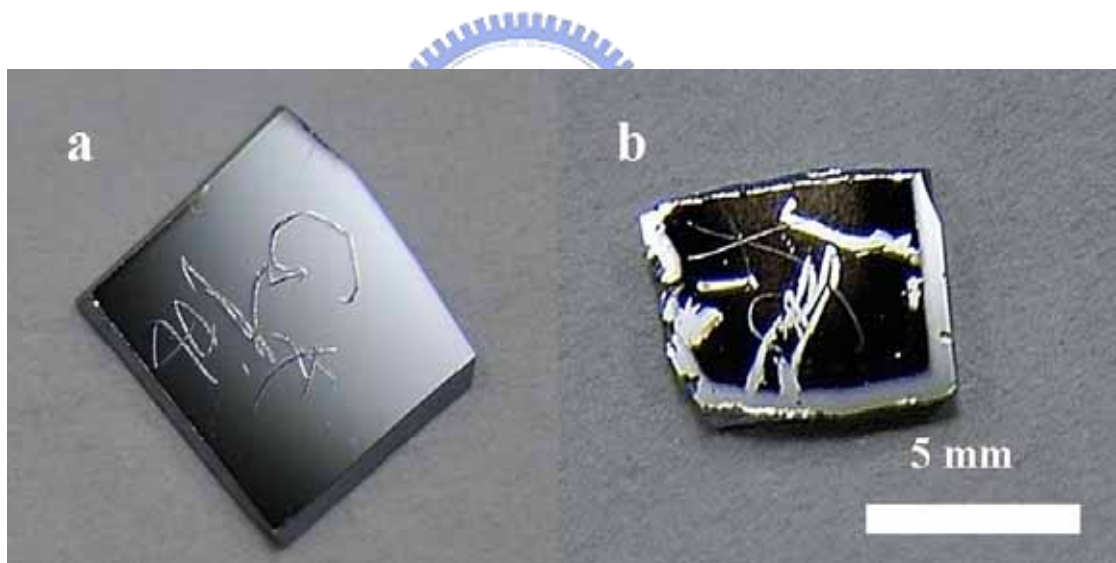


Fig. 4-52 Top-view OM images of effects of specimens stackings: (a) catalyst-coated side of substrate facing plasma, and (b) catalyst-coated side of substrate facing specimen holder.

4.8 Comparison of various catalyst-assisted carbon nanostructures

This section compares the effects of buffer layer, process conditions and synthetic method (MPCVD/ECRCVD) on the characteristics and growth mechanisms of buffer-layer-assisted SWNTs using various catalyst materials. Table 4-9 presents typical experimental results.

4.8.1 Role of buffer layer

In this work, Al-based buffer layer materials demonstrate remarkable effects to enhance SWNTs growth when Co and Fe act catalyst materials. Buffer-layer-assisted CNTs consist of MWNTs and SWNTs demonstrate networks and spaghetti-like morphologies with Co catalyst and Fe as catalyst materials, respectively. Moreover, no CNTs or only MWNTs can be fabricated without Al-based buffer layer application, demonstrating that application of Al-based buffer layer is a favorable condition for SWNTs growth. By contrast, vertical aligned SWNTs films can be fabricated using CoCrPtO_x catalyst precursor film on Si wafer (native SiO_2) without Al-based buffer layer application. However, the application of AlON buffer can further increase the tube number densities and their lengths ($\sim 60 \mu\text{m}$). These results suggest that Al-based buffer layer can encourage the formation of SWNTs with various catalyst materials in this work.

Here we propose that the Al-based buffer layers essentially have the following functions: (1) providing the proper nano-sized dimples on their surface to accommodate the nanoparticles from agglomeration between neighbor nanoparticles, (2) acting as template for the thicker catalyst film to promote formation of nano-sized extrusions for the root growth SWNTs, (3) affecting interactions between catalyst and buffer materials, including chemical bonding formation, wettability and surface tension of catalyst with buffer material, and (4) varying the diffusion path of carbon during CNTs growth. For accommodating effects, the

Al-based buffers can promote the smaller-sized base-growth Fe-assisted and CoCrPtO_x-assisted SWNTs. For effects of acting as template and giving a higher surface tension of Co/buffer interface, the Al-based buffers can enhance the root-growth Co-assisted SWNTs, instead of base-growth Fe-assisted SWNTs. For effect of changing diffusion path, the Al-based buffers can act as the carbon diffusion inhibitor to reduce the possible diffusion path of carbon through Si wafer and to accelerate other carbon diffusion paths during CNTs growth, which may reduce the deposition temperature (~600 °C) of SWNTs by combining with smaller particle sizes.

4.8.2 Raman spectra and field emission properties

With respect to the structures and properties of the as-grown buffer-layer-assisted SWNTs, the Co-assisted SWNTs networks with AlON as the buffer, the spaghetti-like Fe-assisted SWNTs with Al₂O₃ and AlN as buffers yield I_G/I_D ratios of ~15.7, ~10.8 and ~31.5, respectively. The results are in agreement with the reported results in the literature, which indicate that a higher N concentration in the buffer or catalyst may give rise to a higher I_G/I_D ratio by prolonging the activity of the catalyst. In contrast, for CoCrPtO_x-assisted SWNTs with AlON buffer, the I_G/I_D ratio can go up to ~ 43 and the RBM peaks are strong, indicating that the purity of SWNTs of as-produced CNTs is very high. These results agree with morphologies previously determined by FESEM and HRTEM, which demonstrated that MWNTs are easily observed when Co and Fe act as catalysts but hardly any MWNTs can be observed using CoCrPtO_x as a precursor catalyst film. The results also show that the I_G/I_D ratio of the CoCrPtO_x-assisted CNTs, obtained by ECRCVD, is ~ 0.58, which is much lower than the value, 43, obtained for CNTs by MPCVD.

With respect to field emission properties, the turn-on voltages and highest current densities are > 10, 3.4 ~ 3.6, ~4.6 and ~8.0 V/μm (for current density 0.01 mA/cm²), and < 0.01 (at 10 V/μm), ~34 (at 5.6 V/μm), ~33 (at 6.7 V/μm) and ~16 mA/cm² (at 10 V/μm) for root-growth Co-assisted CNTs, base-growth Fe-assisted CNTs, CoCrPtO_x and

MPCVD-assisted SWNTs and CoCrPtO_x and ECRCVD-assisted CNTs, respectively, as summarized in Fig. 4-53. Sparse CoCrPtO_x assisted-CNTs that were fabricated by ECRCVD demonstrate a high turn-on voltage because of their low tube density and many disorders or defects. The turn-on voltage for the denser CoCrPtO_x -assisted SWNTs is higher than that for the well-aligned Fe-assisted CNTs, because of the screening effect. No turn-on voltage can be measured for the root-growth Co-assisted CNTs because most tubes grow horizontally.

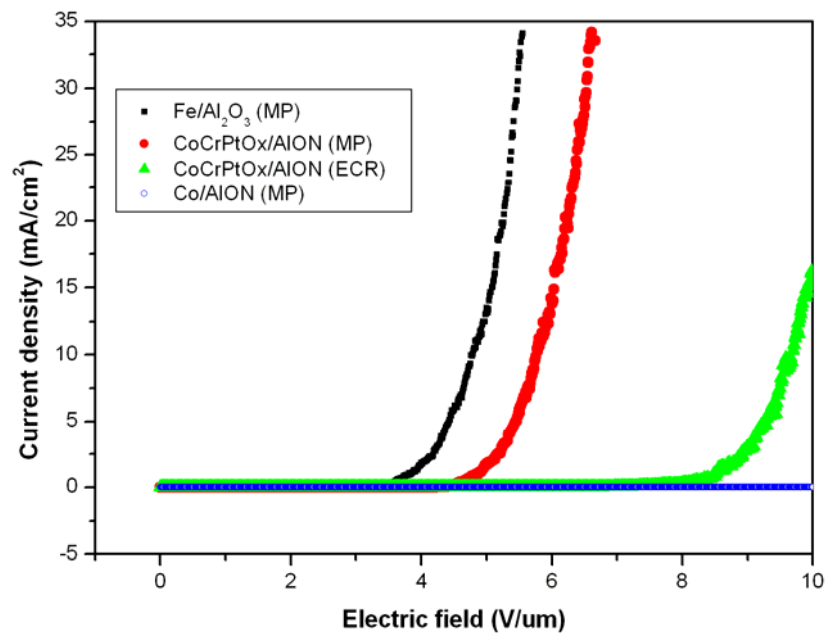


Fig. 4-53 Field emission I-V curves for the Fe-assisted CNTs, the CoCrPtO_x and AION-assisted SWNTs films, the CoCrPtO_x -assisted CNTs (ECRCVD) and the root-growth Co-assisted CNTs.

4.8.3 Process conditions and synthetic methods

Regarding effects of thickness of buffer and catalyst layers, the results indicate that buffer layer thickness (5 ~ 15 nm) has no significant effects on the deposited nanostructures. In contrast to buffer thickness, it shows that smaller catalyst thickness gives rise to smaller tube diameter of the nanostructures.

Regarding effects of temperature and CH_4/H_2 ratio conditions, the results demonstrates that the lowest temperatures to obtain the SWNTs are about the same (Co, ~620 °C; Fe, ~610 °C; CoCrPtO_x ~600 °C), indicating no significant differences among different catalyst

materials. The results appeal that the favorable CH_4/H_2 ratios to grow the smaller sized CNTs or SWNTs for Co, Fe and CoCrPtO_x film are around 5/50, 1.5/200 and 4/50 (sccm/sccm), respectively. In other words, by comparing with the base-growth CNTs, the Co-assisted root-growth SWNTs requires the greatest carbon source concentration.

On CNTs deposition methods, ultra dense well-aligned SWNT films are successfully fabricated with CoCrPtO_x precursor by MPCVD but only entangled small-sized CNTs, which consist of MWNTs, DWNTs and SWNTs, are synthesized by ECRCVD. The morphologies of catalyst particles pretreated by ECRCVD show that small-sized particles are successfully formed; therefore, it is believed that fine pre-treated particles may agglomerate and become large-sized particles during growth process due to directly substrate heating, which is not performed in MPCVD system. On growth mechanism of CoCrPtO_x -assisted CNTs, it is not different to synthesize by ECRCVD and MPCVD.



Table 4-9 Summaries of as-deposited carbon nanostructures on Si wafer with various catalyst and buffer layer materials.

Catalysts	Al-base buffer layer	Co ¹	Fe ²	CoCrPtO _x ³	CoCrPtO _x ^{4,5}
Pretreated particle size (nm)	Without	60	30	2.5~3.5	2~6
	With	35	2~8	1~3.5	2~4
Synthetic method		MPCVD	MPCVD	MPCVD	ECRCVD
As-grown CNT type	Without	None	MWNT	SWNT	SWNT+DWNT +MWNT
	With	SWNT+MWNT	SWNT+MWNT	SWNT	SWNT+DWNT +MWNT ⁶
Morphology	Without	Particle-like	Film	Well-aligned film	Spaghetti-like
	With	Network-like	Spaghetti-like	Extremely dense well-aligned film	Spaghetti-like
Tube size of SWNT (nm)	Without	None	None	~3	2~3
	With	0.8~1.3	0.8~2.1	1.5~2.5	No data
Optimum CH₄/H₂ (sccm/sccm)		5/50	1.5/200	4/50	4/50
Lowest temperature (°C)		620	610	600	658
Best I_G/I_D ratio		Fair (~15.7)	Good(~31.5)	Good (~43)	Poor (~0.58)
Turn-on voltage (V/μm)		> 10	3.4~3.6	~4.6	~8.0
Current density (mA/cm²)		< 0.01	~34	~33	~16
Growth model		Root	Base	Base	Base

Note :

1. Co thickness, 5 nm; AlON buffer layer, 10 nm. 2. Fe thickness, 5 nm; AlN buffer layer, 10 nm. 3. CoCrPtO_x thickness, 1 nm; AlON buffer layer, 10 nm.
4. CoCrPtO_x thickness, 2 nm without buffer layer. 5. CoCrPtO_x thickness, 1 nm with AlON buffer layer. 6. Predicted.

Chapter 5

Conclusions

In this work, the structures, properties and possible growth mechanisms of catalyst and buffer-layer-assisted SWNTs using Co, Fe and CoCrPtO_x films by MPCVD/ECRCVD are presented, and to give the guidelines of selecting the buffer layer materials and manipulating their process conditions. Experimental results are concluded as below:

1. For Co and Fe act as catalysts, the root-growth Co-assisted SWNTs networks and the base-growth spaghetti-like Fe-assisted SWNTs can be synthesized on Si wafers with Al-based materials as buffer layer by MPCVD. By contrast, multi-walled carbon nanotubes (MWNTs) or amorphous carbon films are merely formed with non-Al-based materials or the native SiO₂ as buffer material.
2. For CoCrPtO_x as catalyst precursor, the extremely dense vertically aligned base-growth CoCrPtO_x-assisted SWNTs films can be successfully fabricated on silicon wafer with native SiO₂ buffer layer by MPCVD at low temperatures down to ~ 600 °C. Moreover, the application of AlON buffer layer can further increase the tube length to ~60 μm. Besides, the CoCrPtO_x and AlON buffer layer-assisted SWNTs demonstrates a very high I_G/I_D of up to ~ 43 and its TGA result shows a purity of over 99 %.
3. In contrast to MCVD, the deposited CoCrPtO_x-assisted CNTs by ECR-CVD are the mixing types of base-growth CNTs consisting of SWNTs, double-walled and four-walled-CNTs (~ 2.0, 3.6 and 7.9 nm in diameter, respectively), which are the smallest reported sizes of CNTs in the literature by ECRCVD.
4. The function of the CoCrPtO_x catalyst precursor is essentially to promote miniaturization of the sizes of the pretreated nanoparticles down to less than ~3.0

nm in diameter. This mechanism is based on the explosion associated with the reduction of PtO_x in the CoCrPtO_x film, and Cr_2O_3 is employed to inhibit the agglomeration of nanoparticles during pretreatment and the initial stage of nanostructure deposition.

5. Al-based materials are the most effective buffer layers to enhance SWNTs growth and essentially have the following functions: (1) the proper nano-sized dimples (R_{max} : 1~2 nm) on their surface to accommodate the nanoparticles from agglomeration between neighbor nanoparticles, (2) acting as template for the thicker catalyst film to promote formation of nano-sized extrusions for the root growth SWNTs, (3) affecting interactions between catalyst and buffer materials, including chemical bonding formation, wettability and surface tension of catalyst with buffer material, and (4) varying the diffusion path of carbon during CNTs growth.
6. Regarding effects of process conditions, the results demonstrate that the lowest temperatures to obtain the SWNTs are about the same (around $600^\circ\text{C} \sim 620^\circ\text{C}$) and the favorable CH_4/H_2 ratios to grow the smaller sized CNTs or SWNTs for Co, Fe and CoCrPtO_x film are around 5/50, 1.5/200 and 4/50 (sccm/sccm), respectively. Furthermore, the results indicate that smaller catalyst thickness is favorable to synthesize more amount of SWNTs and buffer layer thickness (5 ~ 15 nm) has no significant effects on deposited nanostructures.
7. On field emission properties, the turn-on voltages are > 10, 4.6 and 3.4 ~ 3.6 V/ μm (for current density $0.01 \text{ mA}/\text{cm}^2$) and the highest current densities are < 0.01 (at 10 V/ μm), ~33 (at 6.7 V/ μm) and ~34 mA/cm^2 (at 5.6 V/ μm) for the root-growth Co-assisted CNTs, the CoCrPtO_x -assisted SWNTs and the base-growth Fe-assisted CNTs, respectively. The turn-on voltage for the CoCrPtO_x -assisted SWNTs is higher than that for the well-aligned Fe-assisted

CNTs is believed to be due to screening effect.

8. In summary, some percentages of the Co and Fe-assisted SWNTs can be synthesized with the application of Al-based buffer layers. However, application of the CoCrPtO_x precursor with AlON buffer layer can assist $> 99\%$ formation of SWNTs. On the other hand, the CoCrPtO_x precursor is the more effective agent to produce and control the structures, purity of the SWNTs on Si wafers than Fe or Co catalysts. The results have improved our thinking to design the desired process to obtain the required nanostructures.



Chapter 6 Future prospects

In this research, Fe, Co and CoCrPtO_x materials were used to act as catalysts or precursor to develop the processes of catalyst and buffer-layer-assisted SWNTs by MPCVD or ECRCVD. The results indicate that Al-based materials are the most effective buffer layers to enhance SWNTs growth and root-growth Co-assisted SWNT networks, base-growth spaghetti-like Fe-assisted SWNTs and extremely dense vertically aligned CoCrPtO_x-assisted SWNT films can be successfully fabricated with at a temperature range of 600~ 640°C by MPCVD/ECRCVD. These results provide the methods to fabricate SWNTs on Si wafer at relatively low temperature and manipulate their structures. However, some subjects should be further studied:

- (a) The composition of as-deposited CoCrPtO_x film in this work is fixed. It is believed that the compositions of CoCrPtO_x can be adjusted to increase the tube length and to manipulate the structures of SWNTs more precisely.
- (b) Catalyst-coated side of substrate is placed downward during CNTs deposition in this study and thus the applications and productivity are limited. The process of catalyst-coated side toward plasma to grow SWNTs must be developed.
- (c) It is possible to synthesize larger area of SWNTs films by modifying the heating system of ECRDVD system to avoid particles agglomeration during growth stage.
- (d) The deposition temperature of ~600 °C is still marginal for Si-based technology. It must be further lowered to 400~500 °C ^[Duesberg-2004-354] to expand the feasibility of applications of SWNTs integrated with Si substrates.
- (e) The mechanism of nitrogen to prolong the activity and lifetime of catalyst should be further studied.

References

A

1. Ando, Y., X. Zhao, K. Hirahara, K. Suenaga, S. Bandow and S. Iijima, *Diamond Relat Mater.* 10 (2001) 1185, “Arc plasma jet method producing single-wall carbon nanotubes”.

B

2. Baumer, M. and H.-J. Freund, *Prog. Surf. Sci.* 61 (1999) 127, “Metal deposits on well-ordered oxide films”.
3. Berber, Savas, Young-Kyun Kwon, and David Tománek, *PHYSICAL REVIEW LETTERS* 84 (2000) 4613, “Unusually High Thermal Conductivity of Carbon Nanotubes”.
4. Bethune, D. S., Kiang C. H., Vries M. S. de, Gorman G., R. Savoy, J. Vazquez, and R. Beyes, *Nature* 363 (1993) 605, “Cobalt- Catalysed growth of carbon nanotubes with single-atomic-layer wall”.
5. Benjamin, M.C., C. Wang, R.F. Davis, and R.J. Nemanich, *Appl. Phys. Lett.* 64 (1994) 3288, “Observation of a negative electron affinity for heteroepitaxial AlN on α (6H)-SiC(OOO1)”.
6. Birkett, P.R., A. J. Cheetham, B. R. Eggen, J. P. Hare, H. W. Kroto, *Chem. Phys. Lett.* 281 (1997) 111, “Transition metal surface decorated fullerenes as possible catalytic agents for the creation of single walled nanotubes of uniform diameter”.
7. Bronikowski, Michael J., Peter A. Willis, Daniel T. Colbert, K. A. Smith, and Richard E. Smalley, *J. Vac. Sci. Technol. A* 19 (2001) 1800, “Gas-phase production of carbon single-walled nanotubes from carbon monoxide via the HiPco process: A parametric study”.

C

8. Cassell, Alan M., Geoff C. McCool, Hou Tee Ng, Jessica E. Koehne, Bin Chen,

Jun Li, Jie Han and M. Meyyappan, 82 (2003) 817, “Carbon nanotube networks by chemical vapor deposition”.

9. Che, J., T. Cagin, and William, Nanotechnology 11 (2000) 65, “A Goddard III Thermal conductivity of carbon nanotubes”.
10. Cheng, H.M., F. Li, G. Su, H. Y. Pan, L. L. He, X. Sun, and M. S. Dresselhaus, Appl. Phys. Lett. 72 (1998) 3282, “Large-scale and low-cost synthesis of single-walled carbon nanotubes by the catalytic pyrolysis of hydrocarbons”.
11. Choi, W. B., Chung D. S., Kang J. H., Kim H. Y., Jin Y. W., Ha I. T., Y. H. Lee, Jung J. E., Lee N. S., Park G. S., and Kim J. M., Appl. Phys. Lett. 75 (1999) 3129, “Fully sealed, high-brightness carbon-nanotube field-emission display”.
12. Chiang, W. I., B. E. Brinson, A. Y. Huang, P. A. Willis, M. J. Bronikowski, J. L. Margrave, R. E. Smalley, and R. H. Hauge, J. Phys. Chem. B 105 (2001) 8297, “Purification and Characterization of Single-Wall Carbon Nanotubes (SWNTs) Obtained from the Gas-Phase Decomposition of CO (HiPco Process)”.
13. Cinke, M., J. Li, B. Chen, A. Cassell, L. Delzeit, J. Han, and M. Meyyappan, Chem. Phys. Lett. 365 (2002) 69, “Pore structure of raw and purified HiPco single-walled carbon nanotubes”.
14. Collins, P. G., M. S. Arnold, and P. Avouris, Science 292 (2001) 706, “Engineering Carbon Nanotubes and Nanotube Circuits Using Electrical Breakdown”.
15. Colomer, J. F., L. Henrard, G. van Tendeloo, A. Lucas, and P. Lambin, Chem. Commun. 14 (1999) 1343, “Synthesis of single-wall carbon nanotubes by catalytic decomposition of hydrocarbons”.
16. Costa, Pedro M.F.J., Steffi Friedrichs, Jeremy Sloan, Malcolm L.H. Green, Carbon 42 (2004) 2527, “Structural studies of purified double walled carbon nanotubes (DWNTs) using phase restored high-resolution imaging”.

D

17. Dai, H., A. G. Rinzler, P. Nikolaev, A. Thess, D. T. Colber, and R. E. Smalley, Chem. Phys. Lett. 260 (1996) 471, “Single-walled nanotubes produced by metal

catalyzed disproportionation of carbon monoxide”.

18. Dai, H., Hafner J. H., Rinzler A. G., Colber D. T., and Smalley R. E., Nature 384 (1996) 147, ”Nanotubes as nanoprobe in scanning probe microscopy”.
19. Delzeit, L., B. Chen, A. Cassell, R. Stevens, C. Nguyen, and M. Meyyappan, Chem. Phys. Lett. 348 (2001) 368, “Multilayered metal catalysts for controlling the density of single-walled carbon nanotube growth”.
20. Delzeit, Lance, Ian McAninch, Brett A. Cruden, David Hash, Bin Chen, Jie Han, and M. Meyyappan, J. Appl. Phys. 91 (2002) 6027, “Growth of multiwall carbon nanotubes in an inductively coupled plasma reactor”.
21. de los Arcos, T., M. Gunnar Garnier, P. Oelhafen, D. Mathys, J. W. Seo, Concepci on Domingo, Jose Vicente Garc Ramos and S. Sanchez-Cortes, Carbon 42 (2004) 187, “Strong influence of buffer layer type on carbon nanotube characteristics”.
22. de los Arcos, Z.M. Wu and P. Oelhafen, Chem. Phys. Lett. 380 (2003) 419, “Is aluminum a suitable buffer layer for carbon nanotube growth?”.
23. Derycke, V., Martel R., Appenzeller J., and Ph. Avouris, Nano Letter 1 (2001) 453, “Carbon Nanotube Inter- and Intramolecular Logic Gates”.
24. Dresselhaus, M. S., G. Dresselhaus, P. C. Eklund, “Science of Fullerenes and Carbon Nanotubes” (Academic Press, New York, 1996), P756.
25. Dresselhaus, M. S., G. Dresselhaus, A. Jorio, A.G. Souza Filho, R. Saito, R. Saito, carbon 35 (2002) 2043, “Raman spectroscopy on isolated single wall carbon nanotubes”.
26. Duesberg, G. S., A. P. Graham, F. Kreupl, M. Liebau, R. Seidel, E. Unger, and W. Hoenlein, Diamond Relat. Mater. 13 (2004) 354, “Ways towards the scaleable integration of carbon nanotubes into silicon based technology”.

E

F

27. Fan, S., Michael G. Chapline, Nathan R. Franklin, Thomas W. Tombler, Alan M. Cassell, Hongjie Dai and W. Hoenlein, *Science* 283 (2004) 512, "Self-Oriented Regular Arrays of Carbon Nanotubes and Their Field Emission Properties".
28. Fischer, J. E., W. Zhou, J. Vavro, M. C. Llaguno, C. Guthy, and R. Haggenueller, *J. Appl. Phys. Science* 93 (2003) 2157, "Magnetically aligned single wall carbon nanotube films: Preferred orientation and anisotropic transport properties".
29. Futaba, Don N., Kenji Hata, Takeo Yamada, Kohei Mizuno, Motoo Yumura, and Sumio Iijima, *Phys. Rev. Letts.* 95 (2005) 056104, "Kinetics of Water-Assisted Single-Walled Carbon Nanotube Synthesis Revealed by a Time-Evolution Analysis".
30. Gao, B., A. Kieinhammes, X. P. Tang, C. Bower, L. Fleming, Y. Wu and O. Zhou, *Chem. Phys. Lett.* 307 (1999) 153, "Electrochemical intercalation of single walled carbon nanotubes with lithium".
31. Gavillet, J., A. Loiseau, C. Journet, F. Willaime, F. Ducastelle, and J.-C. Charlier, *Physical Review Letters* 87 (2001) 275504-1 -275504-4, "Root-Growth Mechanism for Single-Wall Carbon Nanotubes".
32. Govindaraj, A. and C. N. R. Rao, *J. Mater. Res.* 14 (1999) 2567, "An investigation of carbon nanotubes obtained from the decomposition of methane over reduced $Mg_{1-x}M_xAl_2O_4$ spinel catalysts".
33. Gorbunov, A., O. Jost, W. Pompe, A. Graff, *Carbon* 40 (2002) 113, "Solid-liquid-solid growth mechanism of single-wall carbon Nanotubes".
34. Guo, T., P. Nikolaev, A. Thess, D. T. Colbert, and R. E. Smalley, *Chem. Phys. Lett.* 243 (1995) 49, "Catalytic Growth of Single-walled Nanotubes by Laser Vaporization".

H

35. Hamada, Noriaki, Shin-ichi Sawada, and Atsushi Oshiyama, *Phy. Rev. Letters* 68 (1992) 1579, “New One-dimensional Conductors: Graphitic Microtubules”.
36. Hata, K., Don N. Futaba, K. Mizuno, T. Namai, M. Yumura and S. Iijima, *Science* 306 (2004), 1362, “Water-assisted highly efficient synthesis of impurity-free single-walled carbon nanotubes”.
37. Helveg¹, Stig, Carlos Lo’pez-Cartes¹, Jens Sehested¹, Poul L. Hansen¹, Bjerne S. Clausen¹, Jens R. Rostrup-Nielsen, Frank Abild-Pedersen and Jens K. Nørskov, *Nature* 427 (2004) 426, “Atomic-scale imaging of carbon nanofibre growth”.
38. Hofmann, S., B. Kleinsorge, C. Ducati, A. C. Ferrari, and J. Robertson, *Diamond Relat. Mater.* 13 (2004) 1171, “Low-temperature plasma enhanced chemical vapor deposition of carbon nanotubes”.

39. <http://www.helixmaterial.com/product.html>

40. <http://www.cnanotech.com/>



41. Iijima, S., *Nature* 354 (1991) 56, ”Helical microtubules of graphitic carbon”.

J

42. Journet, C., W. K. Maser, P. Bernier, A. Loiseau, M. Lamy, de la Chapelle, S.Lefrant, P. Deniard, R. Lee and J. E. Fischer, *Nature* 388 (1997) 756, “Large-scale production of single-walled carbon nanotubes by the electric-arc technique”.
43. Joselevich, Ernesto and Charles M. Lieber, *Nano lett.* 2 (2002) 1137, “Vectorial Growth of Metallic and Semiconducting Single-Wall Carbon Nanotubes”.
44. Jungwirthova, I., I. Stara, and V. Matolin, *Surf.* 377-379 (1997) 644, “Study of CO interaction with alumina-supported Pd particles”.

K

45. Kato, T., G.-H. Jeong, T. Hirata, and R. Hatakeyama, *Thin Solid Films* 457 (2004) 2, “Structure control of carbon nanotubes using radio-frequency plasma enhanced chemical vapor deposition”.
46. Kim, J., I. Hwang, D. Yoon, I. Park, D. Shin, T. Kikukawa, T. Shima, and J. Tominaga, *Appl. Phys. Lett.* 83 (2003) 1701, “Super-resolution by elliptical bubble formation with PtOx and AgInSbTe layers”.
47. Kim, T. W., M. W. Song, H. L. Koh, and K. L. Kim, *Appl. Catal.* 210 (2001) 35, “Surface properties and reactivity of Cu/g-Al₂O₃ catalysts for NO reduction by C₃H₆ Influences of calcination temperatures and additives”.
48. Kikukawa, T. Nakano, T. Shima, and J. Tominaga, *Appl. Phys. Lett.* 81 (2002) 4697, “Rigid bubble pit formation and huge signal enhancement in super-resolution near-field structure disk with platinum-oxide layer”.
49. Kikkawaa, S., S. Enomotob, K. Hitotab and O. Yamaguchib, *Solid State Ionics* 172 (2004) 239, “Large magnetization of iron nitride at the interface of multilayered iron metal/aluminum nitride thin film deposited by rf sputtering”.
50. Kong, J., A. M. Cassell, and H. Dai, *Chem. Phys. Lett.* 292 (1998) 567, “Chemical vapor deposition of methane for single-walled carbon nanotubes”.
51. Kolobov, A. V., F. Wilhelm, A. Rogalev, T. Shima and J. Tominaga, *Appl. Phys. Lett.* 86 (2002) 121909, “Thermal decomposition of sputtered thin PtO x layers used in super-resolution optical disks”.
52. Kymakis, E., and G. A. J. Amaratunga, *Appl. Phys. Lett.* 80 (2002) 112, “Single-wall carbon nanotube/conjugated polymer photovoltaic devices”.

L

53. Lacerda, R. G., K. B. K. Teo, A. S. Teh, M. H. Yang, S. H. Dalal, D. A. Jefferson, J. H. Durrell, N. L. Rupasinghe, D. Roy, G. A. J. Amaratunga, and W. I. Milne, *Journal of Applied Physics* 96 (2004) 4456, “Thin-film metal catalyst for the production of multi-wall and single-wall carbon nanotubes”.

54. Landi, B. J., R. P. Raffaele, S. L. Castro and S. G. Bailey, *Prog. Photovolt: Res. Appl.* 13 (2005) 165, "Single-wall carbon nanotube-polymer solar cells".
55. Lee, C. J., S. C. Lyu, Y. R. Cho, J. H. Lee, and K. I. Cho, *Chem. Phys. Lett.* 341 (2001) 245, "Diameter-controlled growth of carbon nanotubes using thermal chemical vapor deposition".
56. Lee, Cheol Jin and Jeunghee Park, *Appl. Phys. Lett.* 77 (2000) 3397, "Growth model of bamboo-shaped carbon nanotubes by thermal chemical vapor deposition".
57. Li, Lixiang, Feng Li, Chang Liu, Hui-Ming, *Carbon* 43 (2005) 623, "Cheng Synthesis and characterization of double-walled carbon nanotubes from multi-walled carbon nanotubes by hydrogen-arc discharge".
58. Lin, C. H., H. L. Chang and C. T. Kuo, *Dia. Rel. Mater.* 11 (2002) 922, "Growth mechanism and properties of the large area well-aligned carbon nanostructures deposited by microwave plasma ECRCVD".
59. Lin, C. H., H. L. Chang, C. M. Hsu, A. Y. Lo and C. T. Kuo, *Dia. Rel. Mater.* 12 (2003) 1851, "The role of nitrogen in carbon nanotube formation".
60. Liu, C., Y. Y. Fan, M. Lu, H. T. Cong, H. M. Cheng, M. S. Dresselhaus, *Science* 286 (1999) 1127, "Hydrogen Storage in Single-Walled Carbon Nanotubes at Room Temperature".

M

61. Maruyama, S., Erik Einarsson, Yoichi Murakami and Tadao Edamura, *Chem. Phys. Lett.* 403 (2005) 320, "Growth process of vertically aligned single-walled carbon nanotubes".
62. Minea, T.M., T. S. Point, A. Gohier, A. Granier, C. Godon, and F. Alvarez, *Surface & Coatings Technology* 200 (2005) 1101, "Single chamber PVD/PECVD process for in situ control of the catalyst activity on carbon nanotubes growth".
63. Modi, A., N. Koratkar, E. Lass, B. Wei, and Pulickel M. Ajayan, *Nature* 424

(2003) 171, “Miniaturized gas ionization sensors using carbon nanotubes”.

64. Murakami, Y., S. Chiashi, Y. Miyauchi, M. Hu, M. Ogura, T. Okubo and S. Maruyama, Chem. Phys. Lett. 385 (2004) 298, “Growth of vertically aligned single-walled carbon nanotube films on quartz substrates and their optical anisotropy”.

N

65. Nehasil, V., I. Stara, and V. Matolin, Surf. Sci. 377-379 (1997) 813, “molecular beam study of CO and O₂ sticking coefficients on Rh model catalysts”.
66. Nefedov, V. I., J. Electron Spectrosc. Relat. Phenom. 25 (1982) 29.

67. Nikolaev, Pavel, Michael J. Bronikowski, R. Kelley Bradley, Frank Rohmund, Daniel T. Colbert, K.A. Smith and Richard E. Smalley, Chem. Phys. Lett. 313 (1999) 91, “Gas-phase catalytic growth of single-walled carbon nanotubes from carbon monoxide”.

68. Noda, S, Y. Tsuji, Y. Murakami and S. Maruyama, Appl Phys Lett 86 (2005) 173106, “Combinatorial method to prepare metal nanoparticles that catalyze the growth of single-walled carbon nanotubes”.

O

69. Odom, Teri Wang, Jin-Lin Huang, Philip Kim and Charles M. Lieber, Nature 391 (1998) 62, “Atomic structure and electronic properties of single-walled carbon nanotubes”.

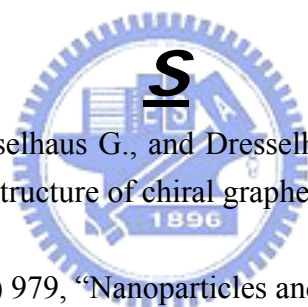
P

70. Patterson, T. A., J. C. Carver, D. E. Leyden, and D. M. Hercules, J. Phys. Chem. 80 (1976) 1702, “A surface study of Cobalt-Molybdena catalyst using X-ray Photoelectron Spectroscopy”.

Q

R

71. Rao, A. M., E. Richter, Shunji Bandow, Bruce Chase, P. C. Eklund, K. A. Williams, S. Fang, K. R. Subbaswamy, M. Menon, A. Thess, R. E. Smalley, G. Dresselhaus, and M. S. Dresselhaus, *Science* 275 (1997) 187, "Diameter-Selective Raman Scattering from Vibrational Modes in Carbon Nanotubes".
72. Raravikar, Nachiket R., Pawel Keblinski, Apparao M. Rao, Mildred S. Dresselhaus, Linda S. Schadler and Pulickel M. Ajayan, *PHYSICAL REVIEW B* 66 (2002) 235424-1, "Temperature dependence of radial breathing mode Raman frequency of single-walled carbon nanotubes".
73. Ram, S., D. Ghosh, and S. K. Roy, *J. Mat. Sci.* 36 (2001) 3745, "Microstructure and topological analysis of Co:Al₂O₃ nanocermet in new FCC and BCC metastable Co-structures".



74. Saito, R., Fujita M., Dresselhaus G., and Dresselhaus M. S, *Appl. Phys. Lett.* 60 (1992) 2204, "Electronic structure of chiral graphene tubules".
75. Satio, Y, *Carbon* 33 (1995) 979, "Nanoparticles and filled nanocapsules".
76. Saito, Yahachi, Mitsumasa Okuda, Naoya Fujimoto Tadanobu Yoshikawa, Masato Tomita, and Takavoshi Hayashi, *Jpn. J. Appl. Phys.* 33 (1994) L526, "Single-wall carbon nanotubes growing radially from Ni fine particles formed by arc evaporation".
77. Saito, Y., S. Uemura, and K. Hamaguchi, *Jpn. J. Appl. Phys.* 37 (1998) L346, "Cathode Ray Tube Lighting Elements with Carbon Nanotube Field Emitters".
78. Sander, J. Tans, A. R. M. Verschueren, and C. Dekker, *Nature* 393 (1998) 49, "Room-temperature transistor based on a single carbon nanotube".
79. Seidel, R., Georg S. Duesberg, Eugen Unger, Andrew P. Graham, M. Liebau, and F. Kreupl, *J. Phys. Chem. B* 108 (2004) 1888, "Chemical Vapor Deposition Growth of Single-Walled Carbon Nanotubes at 600 °C and a Simple Growth Model".

80. Shaijumon, M. M., N. Bejoy, and S. Ramaprabhu, *Appl. Sur. Sci.* 242 (2002) 192, “Temperature dependence of radial breathing mode Raman frequency of single-walled carbon nanotubes”.
81. Soto, G., W. de la Cruz and M.H. Far’ias, *Journal of Electron Spectroscopy and Related Phenomena* 135 (2004) 27, “XPS, AES, and EELS characterization of nitrogen-containing thin films”.
82. Stara, I., V. Nehasil, and V. Matolin, *Surf. Sci.* 365 (1996) 69, “Influence of substrate structure on activity of Alumina supported Pd particles: CO absorption and oxidation”.
83. Suzuki, T., Kenji Suhama, Xinluo Zhao, Sakae Inoue, Noriyoshi Nishikawa and Yoshinori Ando, *Diamond Relat. Mater.* 16 (2007) 1116, “Purification of single-wall carbon nanotubes produced by arc plasma jet method”.
84. Thess, Andreas, Lee, Roland, Nikolaev, Pavel, Dai, Hongjie, *Science* 273 (1996) 483, “Crystalline ropes of metallic carbon nanotubes”.
85. Treacy, M.M., Ebbesen, T.W., Gibson, J.M., *Nature* 38 (1996) 678.” Exceptionally high Young’s modulus observed for individual carbon nanotubes”.
86. Tsai, M. H., M.S. Thesis (2001) Mat. Res. Lab., MSE, NCTU, “Deposition mechanisms and properties of large area well-aligned carbon nanotubes by catalyst-assisted ECR-CVD method”.
87. Tsai, S. H., C. W. Chao, C. L. Lee, and H. C. Shih, *Appl. Phys. Lett.* 74 (1999) 3462, “Bias-enhanced nucleation and growth of the aligned carbon nanotubes with open ends under microwave plasma synthesis”.
88. Tseng, J. Y., C. W. Cheng, S. Y. Wang, and T. B. Wu, *Appl. Phys. Lett.* 85 (2004) 2595, “Memory characteristics of Pt nanocrystals self-assembled from reduction of an embedded PtOx ultrathin film in metal-oxide-semiconductor structures”.
89. Tuinstra, F., and J. L. Koenig, *The journal of chemical* 53 (1970) 1126, “Raman

Spectrum of Graphite”.

V

90. Valentini, L., Tsai, S. H., C. W. Chao, C. L. Lee, and H. C. Shih, *Appl. Phys. Lett.* 74 (1999) 3462, “Bias-enhanced nucleation and growth of the aligned carbon nanotubes with open ends under microwave plasma synthesis”.

W

91. Wang, N., Z. K. Tang, G. D. Li, J. S. Chen, *Nature* 408 (2000) 51.
92. Wagner, C. D., and J. A. Taylor, *J. Electron Spectrosc. Relat. Phenom.* 20 (1980) 83.
93. Wei, B. Q., R. Vajtai, Y. Jung, J. Ward, R. Zhang, G. Ramanath, P. M. Ajayan, *Nature* 406 (2002) 495, “Organized assembly of carbon nanotubes”.
94. Wildoer, Jeroen W. G., Liesbeth C. Venema, Andrew G. Rinzler, Richard E. Smalley and Cees Dekker, *Nature* 391 (1998) 59, “Electronic structure of atomically resolved carbon nanotubes”.
95. Wong, S. S., E. Joselevich, A. T. Woolley, C. L. Cheung, C. M. Lieber, *Nature* 394 (1998) 52, “Covalently functionalized nanotubes as nanometre-sized probes in chemistry and biology”

Y

96. Yang, Q., C. Xiao, W. Chen, and A. Hirose, *Diamond Relat. Mater.* 13 (2004) 433, “Selective growth of diamond and carbon nanostructures by hot filament chemical vapor deposition”.
97. Yoon, Young Joon, Jun Cheol Bae, Hong Koo Baik, Seong Jin Cho, Se-Jong Lee, Kie Moon Song, and No Seung Myung, *Physica B* 323 (2002) 318, “Nucleation and growth control of carbon nanotubes in CVD process”.
98. Yue, G. Z., Q. Qiu, Bo Gao Y. Cheng, J. Zhang, H. Shimoda, S. Chang, J. P. Lu

and O. Zhou, Appl. Phys. Lett. 81 (2002) 355, "Generation of continuous and pulsed diagnostic imaging x-ray radiation using a carbon-nanotube-based field-emission cathode".

Z

99. Zhang, G., D. Mann, L. Zhang, A. Javey, Y. Li, E. Yenilmez, Q. Wang, J. P. McVittie, Y. Nishi, J. Gibbons and H. Dai, PANS 102 (2005) 16141, "Ultra-high-yield growth of vertical single-walled carbon nanotubes: Hidden roles of hydrogen and oxygen".
100. Zhang, L., Y. Tan and Daniel E. Resasco, Chem. Phys. Lett. 422 (2006) 198, "Controlling the growth of vertically oriented single-walled carbon nanotubes by varying the density of Co-Mo catalyst particles".
101. Zhang, Y., Aileen Chang, Jien Cao, Qian Wang, Woong Kim, Yiming Li, Nathan Morris, Erhan Yenilmez, Jing Kong, and Hongjie Dai, Appl. Phys. Lett., 79 (2001) 3155, "Electric-field-directed growth of aligned single-walled carbon nanotubes".
102. Zhong, G., T. Iwasaki, K. Honda, Y. Furukawa, I. Ohdomari, and H. Kwarada, Jpn. J. Appl. Phys. 44 (2005) 1558, "Low Temperature Synthesis of Extremely Dense and Vertically Aligned Single-Walled Carbon Nanotubes".
103. Zhou, Dan, and Su Wang, Appl. Phys. Lett. 65 (1994) 1593, "Single-walled carbon nanotubes growing radially from YC_2 particles".
104. 成會明, "奈米碳管", 五南圖書出版公司(2004) 30.
105. 郭正次, 朝春光, "奈米結構材料科學" (2004) 8-18.

Vita

λ 基本資料

- λ 姓名：王威翔 (Wei-Hsiang Wang)
- λ 性別：男
- λ 出生年月日：民國 60 年 7 月 25 日
- λ 籍貫：台灣省台南市
- λ 通訊地址：新竹市信武陵路 38 號 9 樓之三
- λ 聯絡電話：(03)5425348
- λ 電子信箱：wayne_wang@ritek.com.tw

λ 學歷

- λ 國立交通大學 材料科學與工程所博士班
(民國 91 年 9 月 至 民國 96 年 7 月)
- λ 國立台灣大學 材料科學與工程所碩士班
(民國 83 年 9 月 至 民國 85 年 6 月)
- λ 大同工學院 材料工程系
(民國 79 年 9 月 至 民國 83 年 6 月)

λ 經歷

- λ 銖德科技股份有限公司 研發處 經理
(民國 94 年 7 月 至 民國 96 年 7 月)
- λ 銖德科技股份有限公司 研發處 副理
(民國 90 年 5 月 至 民國 94 年 6 月)
- λ 銖德科技股份有限公司 研發處 研究員
(民國 88 年 7 月 至 民國 90 年 4 月)
- λ 銖德科技股份有限公司 研發處 副研究員

(民國 87 年 6 月 至 民國 88 年 6 月)

λ 金門 284 師 砲兵少尉

(民國 85 年 7 月 至 民國 86 年 5 月)

λ 專長

λ 光學薄膜 PVD 沈積技術

λ 相變化材料技術

λ 可記錄型光碟片之原理與製作

λ 粉末冶金

λ 著作

λ 國際期刊論文

1. Wei-Hsiang Wang and K S Hwang, “The effect of Tungsten particle size on the processing and properties of infiltrated W-Cu compacts”, *Metallurgical and Materials Transactions A* 29A (1998) 1509.

2. Wei-Hsiang Wang, Ming-Huang Lin, Tung-Kuei Lu, Wei-His Chen, Min-Hui Huang, Hui-Fang Tsai, Jei-Ming Chuang and Shyh-yeu Wang, “Study of cyclability enhanced by nitrogen doping for digital versatile disk-random access memory medias”, *Japan Journal of Applied Physics* 41 (2002) 7377.

3. Wei-Hsiang Wang, Li-Chun Chung, and Cheng-Tzu Kuo, “Effects of the SbTe crystallization-induced layer on crystallization behaviors and properties of phase change optical disk”, *Surface and Coating Technology* 177-178 (2004) 795.

4. Wei-Hsiang Wang, Kuo-Min Chao, and Cheng-Tzu Kuo, “Process and characteristics of the large area well-aligned CNTs with open ends by electron cyclotron resonance chemical vapor deposition”, *Diamond and Related Materials* 14 (2005) 753.

5. Wei-Hsiang Wang, Yi-Tung Lin, and Cheng-Tzu Kuo, “Nanofabrication and properties of the highly oriented carbon nanocones”, *Diamond and Related Materials* 14 (2005) 907.
6. Wei-Hsiang Wang, Kuo-Min Chao, I-Ju Teng, and Cheng-Tzu Kuo, “Nanofabrication and the structure-property analyses of phase-change alloy-ended CNTs”, *Surface and Coating Technology* 200 (2006) 3206.
7. Wei-Hsiang Wang, Yu-Rong Peng, and Cheng-Tzu Kuo, “Effects of buffer layer materials and process conditions on growth mechanisms of forming networks of SWNTs by microwave plasma chemical vapor deposition ”, *Diamond and Related Materials* 14 (2005) 1906.
8. Wei-Hsiang Wang, Yu-Rong Peng, Pi-Kai Chuang, and Cheng-Tzu Kuo, “Low-temperature growth mechanism of SWNTs networks by buffer layer-assisted MPCVD”, *Diamond and Related Materials* 15 (2006) 1047.
9. Wei-Hsiang Wang, Tasi-Hau Hang, and Cheng-Tzu Kuo, “Super growth of vertically aligned SWCNTs using self-assembled nanoparticles from CoCrPtOx ultrathin film”, *Carbon* 45 (2007) 97.

λ 國際研討會論文

1. Wei-Hsiang Wang, Tsai-Hau, Hong and Cheng-Tzu Kuo, “Growth of vertically aligned CNTs on the plastic substrate by DVD laser pick-up head system ”, *The 17th European Conference on Diamond, Diamond-like Materials, Carbon Nanotubes, and Nitrides*, (Diamond 2006), Estoril, Portugal (2006).
2. Wei-Hsiang Wang, Yu-Rong Peng, and Cheng-Tzu Kuo, “Synthesis of highly graphitized SWNTs by Al-based buffer layer assisted Fe-catalyst MPECVD”, *International Conference on Superhard Coating*, Kibbutz Fin-Gedi, Israel (2006).

λ 學位論文

博士論文：Processes, characteristics and growth mechanisms of buffer layer-assisted SWNTs using Fe, Co and CoCrPtOx thin films as catalyst materials

碩士論文：鎢銅複合材料的粉末冶金製程

λ 專利

1. 王威翔、郭正次、洪蔡豪，“催化碳管生成反應之觸媒”，中華民國發明專利，申請案號：95119468。
2. 王威翔、郭正次、洪蔡豪，“用來催化碳管生成反應之觸媒的製造方法”，中華民國發明專利，申請案號：95119470。
3. 王威翔、郭正次、洪蔡豪，“單壁碳管的製造方法”，中華民國發明專利，申請案號：95119472。

